

ACID MONOLAYER FUNCTIONALIZED IRON OXIDE NANOPARTICLE CATALYSTS

by

MYLES IKENBERRY

B.S., University of Kansas, 2006

AN ABSTRACT OF A DISSERTATION

submitted in partial fulfillment of the requirements for the degree

DOCTOR OF PHILOSOPHY

Department of Chemical Engineering
College of Engineering

KANSAS STATE UNIVERSITY
Manhattan, Kansas

2014

Abstract

Superparamagnetic iron oxide nanoparticle functionalization is an area of intensely active research, with applications across disciplines such as biomedical science and heterogeneous catalysis. This work demonstrates the functionalization of iron oxide nanoparticles with a quasi-monolayer of 11-sulfoundecanoic acid, 10-phosphono-1-decanesulfonic acid, and 11-aminoundecanoic acid. The carboxylic and phosphonic moieties form bonds to the iron oxide particle core, while the sulfonic acid groups face outward where they are available for catalysis.

The particles were characterized by thermogravimetric analysis (TGA), transmission electron microscopy (TEM), potentiometric titration, diffuse reflectance infrared Fourier transform spectroscopy (DRIFTS), inductively coupled plasma optical emission spectrometry (ICP-OES), X-ray photoelectron spectrometry (XPS), and dynamic light scattering (DLS).

The sulfonic acid functionalized particles were used to catalyze the hydrolysis of sucrose at 80°C and starch at 130°C, showing a higher activity per acid site than the traditional solid acid catalyst Amberlyst-15, and comparing well against results reported in the literature for sulfonic acid functionalized mesoporous silicas. In sucrose catalysis reactions, the phosphonic-sulfonic nanoparticles (PSNPs) were seen to be incompletely recovered by an external magnetic field, while the carboxylic-sulfonic nanoparticles (CSNPs) showed a trend of increasing activity over the first four recycle runs. Between the two sulfonic ligands, the phosphonates produced a more tightly packed monolayer, which corresponded to a higher sulfonic acid loading, lower agglomeration, lower recoverability through application of an external magnetic field, and higher activity per acid site for the hydrolysis of starch.

Functionalizations with 11-aminoundecanoic acid resulted in some amine groups binding to the surfaces of iron oxide nanoparticles. This amine binding is commonly ignored in iron oxide nanoparticle syntheses and functionalizations for biomedical and catalytic applications, affecting understandings of surface charge and other material properties.

ACID MONOLAYER FUNCTIONALIZED IRON OXIDE NANOPARTICLE CATALYSTS

by

MYLES IKENBERRY

B.S., University of Kansas, 2006

A DISSERTATION

submitted in partial fulfillment of the requirements for the degree

DOCTOR OF PHILOSOPHY

Department of Chemical Engineering
College of Engineering

KANSAS STATE UNIVERSITY
Manhattan, Kansas

2014

Approved by:

Major Professor
Keith L. Hohn

Copyright

MYLES IKENBERRY

2014

Abstract

Superparamagnetic iron oxide nanoparticle functionalization is an area of intensely active research, with applications across disciplines such as biomedical science and heterogeneous catalysis. This work demonstrates the functionalization of iron oxide nanoparticles with a quasi-monolayer of 11-sulfoundecanoic acid, 10-phosphono-1-decanesulfonic acid, and 11-aminoundecanoic acid. The carboxylic and phosphonic moieties form bonds to the iron oxide particle core, while the sulfonic acid groups face outward where they are available for catalysis.

The particles were characterized by thermogravimetric analysis (TGA), transmission electron microscopy (TEM), potentiometric titration, diffuse reflectance infrared Fourier transform spectroscopy (DRIFTS), inductively coupled plasma optical emission spectrometry (ICP-OES), X-ray photoelectron spectrometry (XPS), and dynamic light scattering (DLS).

The sulfonic acid functionalized particles were used to catalyze the hydrolysis of sucrose at 80°C and starch at 130°C, showing a higher activity per acid site than the traditional solid acid catalyst Amberlyst-15, and comparing well against results reported in the literature for sulfonic acid functionalized mesoporous silicas. In sucrose catalysis reactions, the phosphonic-sulfonic nanoparticles (PSNPs) were seen to be incompletely recovered by an external magnetic field, while the carboxylic-sulfonic nanoparticles (CSNPs) showed a trend of increasing activity over the first four recycle runs. Between the two sulfonic ligands, the phosphonates produced a more tightly packed monolayer, which corresponded to a higher sulfonic acid loading, lower agglomeration, lower recoverability through application of an external magnetic field, and higher activity per acid site for the hydrolysis of starch.

Functionalizations with 11-aminoundecanoic acid resulted in some amine groups binding to the surfaces of iron oxide nanoparticles. This amine binding is commonly ignored in iron oxide nanoparticle syntheses and functionalizations for biomedical and catalytic applications, affecting understandings of surface charge and other material properties.

Table of Contents

| | |
|--|------|
| List of Figures | ix |
| List of Tables | xii |
| Acknowledgements..... | xiii |
| Chapter 1 - Introduction..... | 1 |
| 1.1 Green Chemistry, Sustainability, and Biofuel Catalysis..... | 1 |
| 1.2 Lignocellulosics for Ethanol and Fine Chemical Production | 1 |
| 1.3 Acid Catalyzed Cellulose Hydrolysis | 4 |
| 1.4 Solid Acid Catalysts..... | 7 |
| 1.5 Sulfonated Amorphous Carbon Catalysts..... | 8 |
| 1.6 Magnetite Nanoparticles | 10 |
| 1.7 Silica Coating of Magnetite Nanoparticles | 15 |
| 1.8 Functionalization strategies | 16 |
| Chapter 2 - Experimental Details..... | 18 |
| 2.1 Precipitation of Magnetite Nanoparticles | 18 |
| 2.2 Sonication | 19 |
| 2.3 Dialysis and Magnetic Washing | 20 |
| 2.4 Diffuse Reflectance Infrared Fourier Transform Spectroscopy (DRIFTS) | 20 |
| 2.5 X-Ray Photoelectron Spectrometry (XPS)..... | 21 |
| 2.6 X-Ray Diffraction (XRD)..... | 21 |
| 2.7 Transmission Electron Microscopy (TEM) | 21 |
| 2.8 Acid-Base Titration..... | 22 |
| 2.9 Dynamic Light Scattering (DLS)..... | 22 |
| 2.10 Zeta Potential Analysis | 22 |
| 2.11 Thermogravimetric Analysis (TGA) | 23 |
| 2.12 Weight Measurement of Wet Catalyst..... | 23 |
| 2.13 High Pressure Liquid Chromatography (HPLC) | 23 |
| 2.14 Inductively Coupled Plasma Atomic Emission Spectroscopy (ICP-OES)..... | 24 |
| Chapter 3 - Di-acid Monolayers on Polydisperse Iron Oxide Nanoparticles | 25 |

| | |
|---|----|
| 3.1 Monolayers of Small Acid Molecules | 25 |
| 3.2 Longer Chain Monolayers | 27 |
| 3.3 Synthesis of 11-Sulfoundecanoic Acid..... | 28 |
| 3.4 Purification of 11-Sulfoundecanoic acid | 30 |
| 3.5 Synthesis of 10-Phosphono-1-Decanesulfonic Acid | 31 |
| 3.5.1 Synthesis of 1,10-Dibromodecane (2) | 31 |
| 3.5.2 Synthesis of Diethyl (10-Bromodecyl) Phosphonate (3)..... | 32 |
| 3.5.3 Synthesis of Diethyl (Sulfonyldecyl) Phosphonate (4)..... | 32 |
| 3.6 Nanoparticle Synthesis and Functionalization..... | 33 |
| 3.7 Catalyst Characterization..... | 34 |
| 3.8 Sucrose and Starch Hydrolysis | 42 |
| 3.9 Conclusions..... | 55 |
| Chapter 4 - Amino Acids on Magnetite..... | 57 |
| 4.1 Amino Acid Ligands..... | 57 |
| 4.2 Literature Discussion of Amine Bonding | 58 |
| 4.3 Syntheses and Characterization | 63 |
| 4.3.1 Monolayer Chain Length Analysis | 63 |
| 4.3.2 Optimization of pH and Temperature | 65 |
| 4.3.3 Carboxylate/Amine-Magnetite Binding in the Presence of Ammonium Ions..... | 69 |
| 4.3.4 11-Aminoundecanoic Acid Functionalization Without HCl | 73 |
| 4.4 Conclusions..... | 77 |
| Chapter 5 - Toward Monodisperse Nanoparticles with Functional Monolayers..... | 78 |
| 5.1 The Importance of Monodispersity..... | 78 |
| 5.2 Toluene Mixed Solvents | 78 |
| 5.2.1 Toluene Mixed Solvents With 11-Bromoundecanoic Acid..... | 78 |
| 5.2.2 Toluene Mixed Solvents With 11-Bromoundecanoic Acid..... | 79 |
| 5.3 Aqueous Digestive Ripening | 80 |
| 5.4 High Temperature Decomposition..... | 81 |
| 5.4.1 High Temperature Decomposition With 11-Bromoundecanoic Acid | 81 |
| 5.4.2 High Temperature Decomposition With 11-Aminoundecanoic Acid | 83 |
| 5.5 Conclusions..... | 86 |

| | |
|--|----|
| Chapter 6 - Future Work | 88 |
| 6.1 Sulfonic Acid Monolayers on Iron Oxide Nanoparticles | 88 |
| 6.2 Amine-Magnetite Bonding | 90 |
| 6.3 Bi-Functional Catalysts..... | 91 |
| 6.4 Atom Transfer Radical Polymerization (ATRP) | 92 |
| References..... | 95 |

List of Figures

| | |
|---|----|
| Figure 1.1 Industrial intermediate chemicals produced from fermentation of glucose monomers (Modified from Corma et al. 2007)..... | 3 |
| Figure 1.2 Two mechanistic pathways for acid catalyzed hydrolysis of cellulose (modified from Rinaldi and Schüth 2009)..... | 5 |
| Figure 1.3 A kinetic model of dilute acid-catalyzed cellulose hydrolysis and degradation (modified from Xiang, Kim, Lee 2003)..... | 6 |
| Figure 1.4 Iron oxide surface charges, from low pH to high pH (modified from Cornell and Schwertmann 2003). | 11 |
| Figure 1.5 An example of bi-layer surfactant formation around a nanoparticle..... | 14 |
| Figure 1.6 Ligand functionalization before and after nanoparticle attachment (adapted from Neouze & Schubert 2008)..... | 14 |
| Figure 3.1 DRIFTS spectra of magnetite nanoparticles functionalized with a) pyromellitic acid, b) 4-sulfophthalic acid, and c) 1,3-propanedisulfonic acid..... | 26 |
| Figure 3.2 DRIFTS spectra for the synthesized, vacuum filtration-purified 11-sulfoundecanoic acid ligand. | 30 |
| Figure 3.3 Sequence of steps(De, Aswal, & Ramakrishnan, 2010; Taffa, Kathiresan, & Walder, 2009; X. Wang & Lieberman, 2003) used to prepare diethyl(sulfonyldecyl)phosphate (4). 31 | 31 |
| Figure 3.4 DRIFTS spectra of the a) CSNPs b) 11-sulfoundecanoic acid c) NaOH neutralized PSNPs d) 10-phosphono-1-decanesulfonic acid..... | 35 |
| Figure 3.5 XRD for a) PSNPs after 18 hours of starch hydrolysis at 130°C b) PSNPs as synthesized c) CSNPs after 18 hrs starch hydrolysis at 130°C d) CSNPs as synthesized e) bare particles. Lines denote goethite peaks..... | 36 |
| Figure 3.6 Histogram of particle sizes measured from TEM images of CSNPs, giving an average diameter of 13 nm. | 38 |
| Figure 3.7 PSNPs sonicated for one hour at neutral pH deposit on a TEM grid as both a) non- agglomerated particles with an average diameter of 5.2 nm and b) agglomerates with an average particle diameter of 12.9 nm..... | 39 |
| Figure 3.8 TGA graph of catalyst weight % vs. the temperature (°C). The total weight loss is a) 5.6% for the CSNPs and b) 18.7% for the PSNPs | 41 |

| | |
|--|----|
| Figure 3.9 Sucrose hydrolysis at 80°C using 0.05g catalyst, 0.1g sucrose, and 5g water. | 46 |
| Figure 3.10 TEM images from CSNPs deposited a) at room temperature in pure water b) from an aqueous 80°C sucrose solution after a 6 hour reaction. | 47 |
| Figure 3.11 Sucrose hydrolysis at 80°C using 0.05g catalyst, 0.1g sucrose, and 5g water. | 50 |
| Figure 3.12 6-hour sucrose reaction supernatants contain PSNPs which remained suspended in the presence of the external magnetic field. | 50 |
| Figure 3.13 XPS survey of a) PSNPs before reaction b) PSNPs after 17 sucrose reactions and washing to remove sugars | 53 |
| Figure 3.14 TOF [mol glucose (mol H ⁺) ⁻¹ hr ⁻¹] for three runs of 24 hour starch hydrolysis at 130°C | 54 |
| Figure 4.1 The amphoteric iron oxide nanoparticle surface has electrostatic attractions to oppositely charged moieties (Cornell and Schwertmann). | 58 |
| Figure 4.2 Ligand coordination modes on the surface of iron oxide and their carboxylate analogues (modified from Cornell and Schwertmann). | 61 |
| Figure 4.3 Commonly recognized potential binding structures for amino acids do not include the possibility of amine coordination to the particle surface. These possible binding structures come from a study on the surface charge of particles functionalized with the amino acids a) i-iv) Glucine, b) vi-vii) Lysine (adapted from J.Y. Park et al., 2009). | 63 |
| Figure 4.4 Synthesis with 3 washes to remove ammonium ions after particle precipitation, pH adjustment to 5 before and after ligand addition, and 3 hours of ligand functionalization at 80°C. | 64 |
| Figure 4.5 Synthesis with sonication prior to pH adjustment, with NH ₄ ⁺ ions present during ligand bonding, at varied temperatures and pH environments. | 65 |
| Figure 4.6 Thermogravimetric analysis of iron oxide particles functionalized with 11-aminoundecanoic acid at different temperatures and pH environments. | 66 |
| Figure 4.7 Magnetite's amphoteric variations in surface concentrations of FeOH ²⁺ , FeOH ⁰ , and FeO ⁻ at different pH chemical environments (modified from Cornell and Schwertmann 2006). | 67 |
| Figure 4.8 DRIFTS spectra of a) 11-aminoundecanoic acid, and particles whose functionalization occurred at b) 95°C, pH3 c) 75°C, pH 5, d) 75°C, pH 3 | 68 |

| | |
|--|----|
| Figure 4.9 Synthesis of amino-acid functionalized particles in the presence of excess ammonium ions, at pH 3, 5, 9, and 10.4. | 70 |
| Figure 4.10 XPS survey scans of 11-aminoundecanoic acid functionalized particles in the presence of ammonium ions in a solution at a) pH 10.8 b) pH 9 c) pH 5 d) pH 3 | 71 |
| Figure 4.11 DRIFTS spectra for particles functionalized with 11-aminoundecanoic acid at a) pH 3 b) pH 5 c) pH 9 d) pH 10.4 | 72 |
| Figure 4.12 Synthesis of two batches without HCl addition. One was washed as shown above. The other batch was functionalized the same way, except that it was not washed..... | 73 |
| Figure 4.13 Zeta potential measurements for the sample synthesized after removal of ammonium ions..... | 74 |
| Figure 4.14 Zeta Potential measurements for the sample synthesized without removal of ammonium ions..... | 75 |
| Figure 4.15 DRIFTS spectra for particles synthesized a) in the presence of ammonium left over from precipitation and b) after washing to remove ammonium ions..... | 76 |
| Figure 5.1 Magnetite nanoparticles after a) synthesis by co-precipitation, b) heating with 11-aminoundecanoic acid in pH 5 water at 95°C for 6 hours c) digestively ripened with boiling water reflux for 72 hours in pH 4 solution..... | 80 |
| Figure 5.2 Precursor composed of an Fe ³⁺ atom coordinated to the carboxylates of three molecules of 11-bromoundecanoate. | 82 |
| Figure 5.3 A bi-layer of 11-bromoundecanoic acid around a magnetite nanoparticle. | 83 |
| Figure 5.4 XPS surveys of the a) 11-aminoundecanoate Fe ³⁺ precursor and b) darker precursor material separated or chemically changed during three centrifugal washes. | 84 |
| Figure 6.1 11-aminoundecanoic acid can form an amide bond to 2-bromo-2-methylpropanoyl bromide | 94 |

List of Tables

| | |
|--|----|
| Table 1 Common iron oxide nanoparticle synthesis techniques (Modified from Lu, Salabas, Schüth 2007) | 10 |
| Table 2 Theoretical ligand loadings and elemental ratios calculated for particles of various diameters. | 40 |
| Table 3 Calculated properties for CSNPs, PSNPs, and bare particles, based on particle diameters from XRD data..... | 40 |
| Table 4 Hydrolysis reactions for 0.1g sucrose and 5g water at 80°C for 6 hours, averaged from two runs with no catalyst, 0.05g bare Fe ₃ O ₄ nanoparticles, 0.0025g 11-sulfoundecanoic acid, and 0.001g 10-phosphono-1-decanesulfonic acid. | 44 |
| Table 5 ICP measurements of iron and sulfur in the supernatants of the first four sucrose hydrolysis runs with CSNPs. | 48 |
| Table 6 ICP data for the inseparable catalyst remaining in solution after 6 hour sucrose runs.... | 51 |
| Table 7 Elemental compositions as estimated for the initial catalyst composition, and measured by ICP for sucrose hydrolysis losses and the final reaction solution..... | 52 |
| Table 8 XPS survey compositions for PSNPs before and after 17 sucrose reactions..... | 53 |
| Table 9 Acid loadings measured by titration for magnetite particles functionalized with 11-aminoundecanoic acid at varying temperatures and solution pH. | 67 |
| Table 10 Nitrogen atomic compositions from XPS surveys for ligands functionalized at pH 3, 5, 9, and 10.4, with 3-aminocaproic acid, 6-aminohexanoic acid, and 11-aminoundecanoic acid..... | 71 |

Acknowledgements

Many people at K-State have contributed to the development of the work presented in this thesis. First, Dr. Keith L. Hohn has provided me with excellent support and guidance during this PhD research, and I am very grateful for his mentoring and encouragement.

I also thank my committee members Dr. Donghai Wang, Dr. Kenneth Klabunde, Dr. Donghai Wang, and Dr. Peter Pfromm for their time and efforts that produced extremely valuable comments and influence over this work.

Many thanks also go to Dr. Dan Boyle for help during use of the TEM within Kansas State University's Biology Research Microscope and Image Processing Facility, to Dr. Hongwang Wang and Dr. Stefan Bossman for help during use of the centrifuge and DLS and for Zeta potential analysis within the Kansas State University Department of Chemistry, to Daming Wei for XRD analysis with the Kansas State University Department of Chemical Engineering, to Yonghui Li for help during use of the TGA within the Kansas State University Department of Biological and Agricultural Engineering, to Phillip Defoe for ICP analysis within the Kansas State University Department of Agronomy, and to the current and former Kansas State University Department of Chemical Engineering staff including David Threewit, Florence Sperman, Karene DeBardeleben, Pat Nelson, Cindy Barnhart, and Alison Hodges.

I also want to thank the past and current members of my research group and collaborators Chienchang Huang, Leidy Peña, Xianjiao Sun, and Jingyi Xie for many productive discussions and good times. And I want to thank Dr. L.T. Fan and Dr. Larry Erickson for their inspirational and educational contributions toward my passion for developing the sustainable technologies of the future.

Finally, I thank my parents Lane Ikenberry, Joleen Abell, Sandy Chism, and Randall Abell for their support and love throughout my life.

This work has been supported by, or in part by, the Kansas State University Center for Sustainable Energy, the National Science Foundation, and the Kansas National Science Foundation's Experimental Program to Stimulate Competitive Research (EPSCoR).

Chapter 1 - Introduction

1.1 Green Chemistry, Sustainability, and Biofuel Catalysis

Oil resources are non-renewable, and the expanding economies of the world will require renewable material sources and processing methods if economic development is to be sustainable. Fortunately, the world's annual production of biomass is greater than 170 billion metric tons, and three fourths of that material is carbohydrates, which are thought to be a potential feedstock for a sustainable world chemical industry in the future (Corma, Iborra, & Velty, 2007). One key to this sustainable chemical market is the development of manufacturing processes which are inexpensive and environmentally friendly. Current industrial processes, mainly involving petrochemicals, consume more than 15 million tons of sulfuric acid every year as a non-recyclable catalyst (Hara et al., 2004). Green chemistry seeks to introduce solid acid catalysts such as zeolites, heteropolyacids, and ion-exchange resins to replace sulfuric acid, hydrochloric acid, and aluminum trichloride, thus lowering the energy consumption and waste generation of such acid-catalyzed processes (Dhepe, Ohashi, Inagaki, Ichikawa, & Fukuoka, 2005; Hara et al., 2004). Biofuel production often requires the same homogenous acid and base catalysts that are used in other industrial processes, significantly increasing the production costs and environmental impacts of such commodities (Carvalho, Duarte, & Gírio, 2008).

1.2 Lignocellulosics for Ethanol and Fine Chemical Production

Industrial scale production of cellulosic ethanol has the potential to replace a share of the transportation fuels market which presently is derived from traditional petroleum sources (Carroll & Somerville, 2009; Rostrup-Nielsen, 2005). More than 36 billion gallons of cellulosic biofuels are expected to be produced every year by 2022, with biofuels generating more than 30% of U.S. transportation fuels (Perlack & Stokes, 2011). Cellulosic ethanol (as opposed to corn ethanol) is derived from renewable sources of low value biomass and does not contribute to increases in global food prices (Carroll & Somerville, 2009; Gallezot, 2008; Naik, Goud, Rout, & Dalai, 2010; Ye Sun & Cheng, 2002).

The first step in the conversion of lignocellulosic material to ethanol and fine chemicals is the disruption of the hemicellulose-lignin-cellulose bonds and interwoven structures. This can be accomplished by traditional acid, hydrothermal, wet oxidation, delignification, or alkaline pretreatments (Carvalho et al., 2008). Some recent research involves the use of ionic liquids and phosphoric acid/salts to accomplish the pretreatment (Charmot & Katz, 2010; Harris et al., 2009; Kilpeläinen et al., 2007; C. Li, Wang, & Zhao, 2008; Mahadeva & Kim, 2009; Rinaldi & Schüth, 2009; Z. Zhang & Zhao, 2009). Different pre-treatment methods accomplish different solubilizations, for example alkaline solutions dissolve more lignin while leaving mostly hemicellulose and cellulose in the solid phase, while acidic solutions dissolve mostly hemicellulose while leaving mostly lignin and cellulose in the solid phase (Carvalho et al., 2008). After pretreatment, the cellulose is exposed, and higher rates of hydrolysis can be accomplished through the enzymatic or acid catalyzed hydrolysis of the β -1,4 bonds. Glycosidic β -1,4 bonds are equatorial and correspond to straight, crystalline chains of glucose monomers with strong hydrogen bonding between polymeric chains. Strong acid solution accomplishes the disruption of lignocellulosic bonds and structure, exposure of cellulose, and hydrolysis of sugars simultaneously.

To maximize the economic productivity of a lignocellulosic processing plant, it is necessary to obtain the hydrolysis products of hemicellulose and cellulose along with purified lignin without producing large amounts of degradation products. There are substantial economic benefits from obtaining the full value of the co-products in addition to the main product glucose (Y.-H. P. Zhang et al., 2007). Such profits are possible only with catalytic processing procedures which give a high selectivity toward desirable molecules by avoiding the formation of waste by-products. Typically, homogeneous catalysis with strong acids such as sulfuric acid is associated with higher rates of by-product formation (Carvalho et al., 2008; Yong Sun, Zhuang, Lin, & Ouyang, 2009).

After separation of lignin and hemicellulose, the homopolymer cellulose can be hydrolyzed into its monomeric glucose molecules which can be further processed into valuable industrial chemicals and fuels (Rinaldi & Schüth, 2009). Some of the industrially significant molecules produced from glucose are shown in Figure 1.1 (Corma et al., 2007).

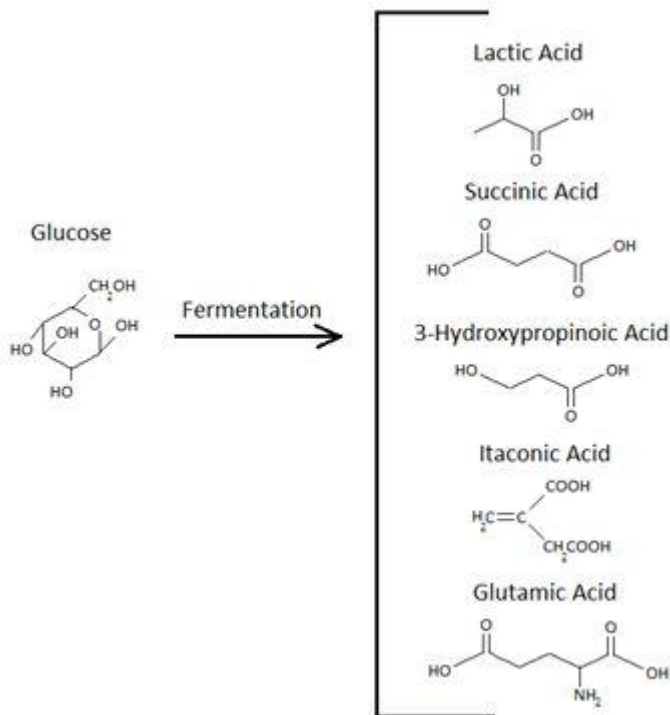


Figure 1.1 Industrial intermediate chemicals produced from fermentation of glucose monomers (Modified from Corma et al. 2007).

Hemicellulose bonds can be broken fairly easily and thus the main concern regarding of interaction between pretreatment acid catalysts and hemicellulose is the formation of degradation products. The hemicellulose degradation products such as phenolic compounds, weak acids, and furan derivatives are known to inhibit downstream fermentation processes and lower the overall process efficiency (Carvalho et al., 2008).

Breaking cellulose bonds is much more difficult than breaking the bonds of hemicellulose. Cellulose is insoluble in most solvents, and thus liquid and solid phase cellulose hydrolysis catalysts typically interact with cellulose through either a heterogeneous or solid-solid mechanism, respectively (Gan, Allen, & Taylor, 2003). Cellulose is composed of D-glucopyranose units connected by β -1,4 linkages, which make the homopolymer highly crystalline and stable, strongly resisting catalysis by both acids and enzymes (Rinaldi & Schüth, 2009; Ye Sun & Cheng, 2002). Catalytic activity has been seen to sharply increase for enzymatic molecules smaller than 3 nm (Fan, Gharpuray, & Lee, 1987). Acid-catalyzed breakage

of the β -1,4 glucose bonds requires either a strong concentration of acid or else a high reaction temperature (Carvalho et al., 2008; Ye Sun & Cheng, 2002).

Both enzymatic and acid catalyzed cellulose hydrolysis have significant disadvantages. Enzymes are somewhat expensive to produce, non-recyclable, and slow to react (Gan et al., 2003), while homogeneous mineral acid catalysts such as sulfuric acid produce degradation products and require expensive separation or neutralization after reaction completion (Carvalho et al., 2008; Yong Sun et al., 2009).

Currently, cellulosic ethanol is economically unable to compete with traditional petroleum fuel sources (Ye Sun & Cheng, 2002). To allow for cellulosic ethanol to compete in the open market without heavy subsidization, it is necessary to lower the production costs associated with chemical pre-treatment (Nagle, Ibsen, & Jennings, 1999; Stavrinides, Phipps, & Shamma, n.d.; Ye Sun & Cheng, 2002; Y.-H. P. Zhang et al., 2007) and hydrolysis (Nagle et al., 1999; Ye Sun & Cheng, 2002; Y.-H. P. Zhang et al., 2007). Pretreatment may account for as much as 25% of the total cost of cellulosic ethanol (Aden et al., 2002). An economically feasible catalyst for industrial cellulose hydrolysis would be easily separable and recyclable with a high activity for catalyzing cellulose hydrolysis and a high selectivity to glucose (Dhepe et al., 2005).

1.3 Acid Catalyzed Cellulose Hydrolysis

Acid catalysis of cellulose hydrolysis proceeds first with the breaking of hydrogen bonds and the separation of long chain oligomers from more crystalline bulk cellulose (Stephens, Whitmore, Morris, & Bier, 2008). As the cellulose becomes lower in molecular weight and less crystalline, it also becomes more accessible to enzymatic and acid hydrolysis (Gehlen, 2009).

A variety of acids can be used to catalyze cellulose hydrolysis, proceeding through the two mechanisms detailed in Figure 1.2. Weakly acidic carboxylic acids show a much lower activity than strongly acidic sulfonic acid groups, but carboxylic acids also produce much less degradation products and thus have been shown to have the potential for an overall higher selectivity towards the formation of glucose (Mosier, Ladisch, & Ladisch, 2002). Concentrated strong acid solutions can be used to disrupt the hydrogen bonds of the crystalline cellulose.

Subsequent addition of water to the concentrated acid solution, also at low temperatures, leads to the formation of glucose (Orozcoa, Ahmada, Rooneya, & Walker, 2007; Yamaguchi et al., 2009). Because of the low temperatures throughout the process, the formation of degradation products is avoided (Orozcoa et al., 2007; Yamaguchi et al., 2009). Concentrated acid saccharification can be successful only if the acid can be easily separated from the sugar, recovered, and reconcentrated (Y.-H. P. Zhang et al., 2007).

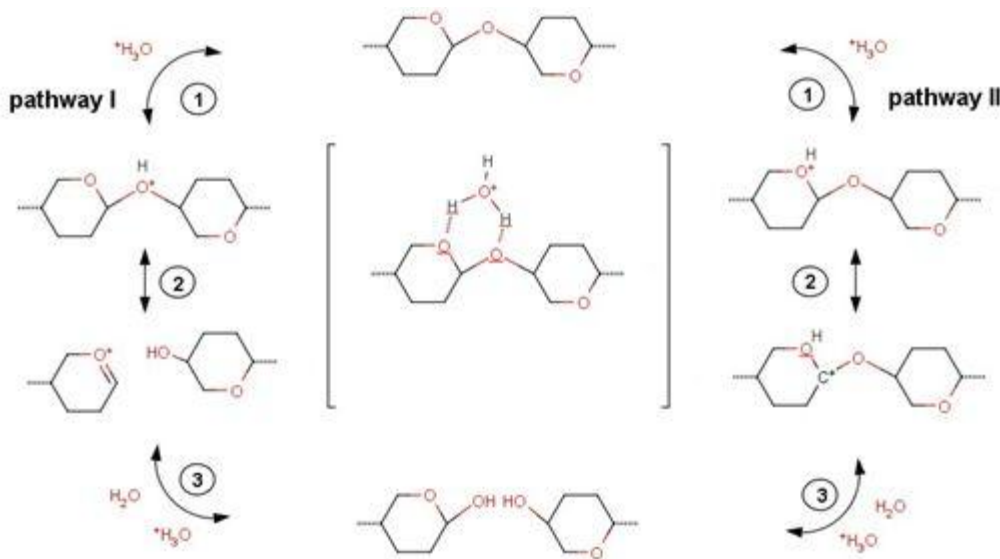


Figure 1.2 Two mechanistic pathways for acid catalyzed hydrolysis of cellulose (modified from Rinaldi and Schüth 2009)

The kinetics of the complex reactions taking place during acid catalyzed hydrolysis are known with much less certainty than the two mechanistic pathways of glucose formation. Multiple kinetic models for acid hydrolysis of cellulose have been reported in the literature (Gehlen, 2009), but recent publications are in agreement that the conventional two-step kinetic model (in which cellulose converts to glucose and glucose converts to degradation products) is inadequate (Gehlen, 2009; WPettersson et al., 2003; Xiang, Kim, & Lee, 2003). With concentrated acid catalysis, fast quenching is considered necessary to prevent degradation of glucose monomers because glucose degrades more rapidly than oligomers (Xiang et al., 2003). Another important consideration is the recondensation of glucose and lignin which can form a complex in solution and lower the process yield of glucose (Xiang et al., 2003). An example of a recently proposed overall reaction scheme is shown in Figure 1.3 (Xiang et al., 2003). It should be noted that this model does not take into consideration the ability of cellulose and oligomers to

directly form degradation products as suggested by other kinetic modelers (Bouchard & Overend, 1992).

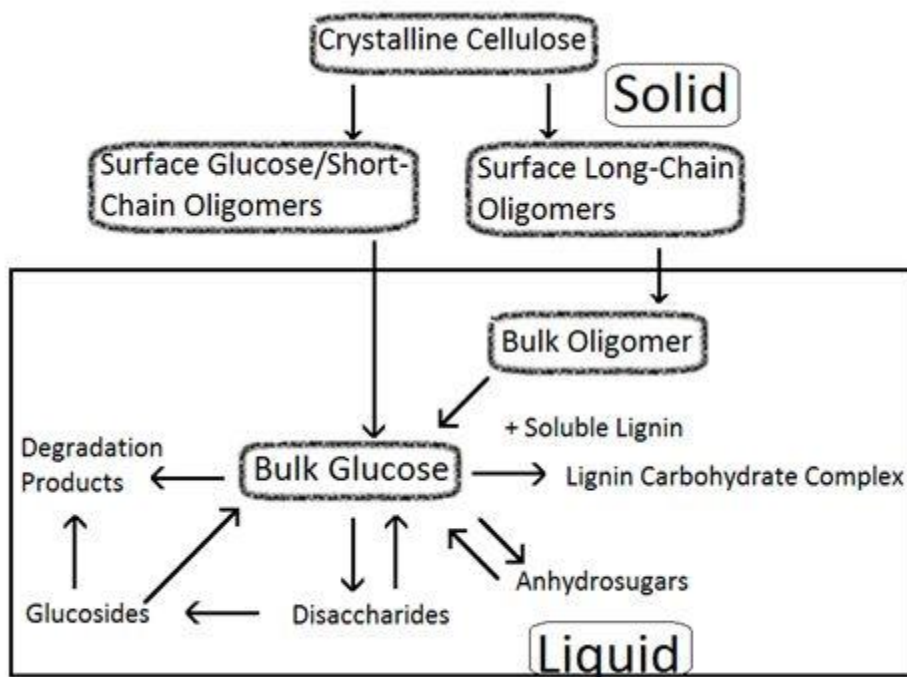


Figure 1.3 A kinetic model of dilute acid-catalyzed cellulose hydrolysis and degradation (modified from Xiang, Kim, Lee 2003).

For the production of cellulosic ethanol, the hydrolysis of cellulose into glucose is quickly and efficiently catalyzed by sulfuric acid, but the cost associated with waste separation and disposal has prevented an economically efficient large-scale saccharification of cellulosic materials (Van de Vyver et al., 2010). A heterogeneous catalyst capable of efficiently catalyzing cellulose hydrolysis at mild conditions could reduce the costs associated with waste disposal and enable large-scale utilization of cellulosic biofuels.

Because cellulose is insoluble in water, acid groups must be located on a solid catalyst's outer surface or in mesoporous channels open to oligomer fragment diffusion in order to hydrolyze the β -1,4 linkages of cellulose (Geboers et al., 2011; Van de Vyver, Geboers, Jacobs, & Sels, 2011). Some of the most successful cellulose hydrolysis catalysts are sulfonated amorphous carbons (Kitano et al., 2009; Onda, Ochi, & Yanagisawa, 2008), sulfonated mesoporous silicas (Lai, Deng, Guo, & Fu, 2011), sulfonated mesoporous carbons (Pang, Wang,

Zheng, & Zhang, 2010), and sulfonated carbon-silica composites (Van de Vyver et al., 2010). Of these solid acid catalysts, the highest cellulose conversion (94.4%) and glucose yield (74.5%) was achieved by the sulfonated mesoporous carbons. It is thought that cellulose conversion increases along with both the density of sulfonic acid groups and the surface area of the solid acid catalyst (Pang et al., 2010), although some investigators suggest that molecular structures such as hydroxyl groups, carboxylic acids, and graphitic moieties increase the solid acid's interaction with cellulose and thus increase the rate of hydrolysis (Kitano et al., 2009; Onda et al., 2008).

1.4 Solid Acid Catalysts

Green chemistry seeks to replace non-recyclable homogenous mineral acid catalysts with recyclable solid acid catalysts for the production of industrial chemicals (Okuhara, 2002). Many biofuels and industrial chemicals can be produced with a lower energy consumption and waste production if suitable solid acid catalysts can be developed with the appropriate activities and selectivities (Okuhara, 2002). Currently scientists must experimentally optimize solid acid catalysts for particular molecular transformations instead of basing optimizations around theoretical calculations (Gobin & Schüth, 2008; Jérôme, Pouilloux, & Barrault, 2008; Notestein & Katz, 2006; Thomas, 1997).

The behavior of hydronium and hydroxide ions in bulk water and at hydrophobic and hydrophilic surface interfaces has been the subject of extensive research in recent literature, and there is extensive debate regarding the correct interpretations of theoretical and experimental data (Ghosh et al., 2008; Kusaka, Wang, & Seinfeld, 1998; Mbaraka & Shanks, 2006; Mundy, Kuo, Tuckerman, Lee, & Tobias, 2009; X. Sun, Yoo, Xantheas, & Dang, 2009; Thøgersen, Jensen, Petersen, & Keiding, 2008; F. Wang, Izvekov, & Voth, 2008). Molecular simulations have indicated that hydrated hydronium cations may form unusual cation pairs, and that high concentrations of acid may lead to long-range ordering (F. Wang et al., 2008). Other simulations have suggested that hydrophobic forces acting out through transient hydrogen bonding in a bulk fluid can have long-range (75 Å) effects that extend beyond the solvation range of a surface, in agreement with experiments (Kanth, Vemparala, & Anishetty, 2010). For these reasons, the performance of solid acid catalysts might not be reducible to the strength and number of acid

sites. The distance between acid groups, as well as the presence of hydrogen bonding or non-polar moieties at the outer surface where the acid sites are located, may have a significant effect on the catalytic activity and selectivity for various reactions.

Although heterogeneous catalysts have already been proven very useful in replacing traditional homogeneous acid catalysts, improvements are still necessary in terms of stability, activity, and selectivity if heterogeneous acid catalysts are going to become thoroughly integrated into the industrial chemical production processes (Corma et al., 2007; Okuhara, 2002). Also, a mixture of solid acid and base catalysts may be employed simultaneously so as to achieve multiple reactions within a single step and thus eliminate costly separation and purification steps (Corma et al., 2007).

1.5 Sulfonated Amorphous Carbon Catalysts

Sulfonated carbon catalysts have received a large amount of attention recently and are thought to have the potential to replace sulfuric acid in many industrial applications including the production of biofuels such as biodiesel (Shu et al., 2010) and cellulosic ethanol (Suganuma et al., 2010; Yamaguchi et al., 2009). It is thought that the catalyst will be applicable to most industrial chemical syntheses which currently employ sulfuric acid. It has been demonstrated that for some reactions the carbon catalyst material has the ability to outperform homogeneous sulfuric acid even though it contains merely 5%-6% of the available hydronium ions (Nakajima, Hara, & Hayashi, 2007).

Amorphous carbon acid catalysts have been created by heating carbonaceous materials such as furfural, naphthalene, glucose, and cellulose to high temperatures in an inert atmosphere and subsequently sulfonating the materials so as to incorporate sulfonic acid groups into large aromatic sheets. These materials achieve high loadings of stabilized strong acid groups and have been used to efficiently and selectively catalyze reactions involving various sugars, industrial chemicals, and crystalline cellulose. Titration of amorphous carbon synthesized from a cellulose precursor indicated that one gram of the synthesized amorphous carbon catalyst contains 1.5 mmol of sulfonic acid groups, 0.4 mmol of carboxylic acid groups, and 5.6 mmol of almost neutral phenolic hydrogens (Suganuma et al., 2010).

It is believed that the amorphous carbon catalyst's extremely high activity for cellulose hydrolysis results from hydrogen bonding between the phenolic and carboxylic moieties and the cellulose oligomers, and for this reason some authors refer to the amorphous carbon catalysts as synthetic enzymes (Kitano et al., 2009; Sukanuma et al., 2010). Despite the successful qualitative characterizations of the various functional groups, and the numerous successful lab-scale applications of the sulfonated amorphous carbon catalysts, the molecular structures responsible for catalysis remain unproven due to difficulties in quantification (Nakajima et al., 2007).

In an attempt to prove the hypothesis regarding the amorphous carbon material's high activity for catalyzing cellulose hydrolysis, reactions were conducted on the hydrolysis of water-soluble β -1,4-glucan. A variety of strongly acidic solid Brønsted acids failed to catalyze the reactions, but the amorphous carbon was successful. The authors concluded that strong hydrogen bonding between the long chain glucans and the catalyst's graphene-based phenolic and carboxylic functional groups is responsible for increased interaction of the soluble glucans with the amorphous carbon surface, exposing the glucans to the strong sulfonic acid groups much more efficiently than the other solid acids (Kitano et al., 2009). The amorphous carbon catalyst was shown to have activity comparable to sulfuric acid (Onda et al., 2008), but with significantly lower production of degradation by-products 5-hydroxymethylfurfural or levulinic acid. Further, the carbon-based material was recyclable without decreased activities.

Recently the amorphous carbon catalyst has been coupled with silica, producing a material that has been shown to be catalytic for some reactions that could not be catalyzed by amorphous carbon alone (Nakajima et al., 2009). A sulfonated silica-carbon hybrid was also shown to catalyze cellulose hydrolysis better than any previous solid acid catalyst, which the authors attribute to increased surface area and the increased hydrophilicity resulting from the presence of the silica (Van de Vyver et al., 2010).

1.6 Magnetite Nanoparticles

Magnetite nanoparticles were first created from the co-precipitation of iron chloride salts with ammonium hydroxide in 1981 by Massart (Massart, 1981). Magnetite is composed of oxygen anions in a close-packed structure with iron cations at the interstices and magnetite's magnetic properties arise from a super-exchange mechanism (Harris et al., 2009). Superparamagnetic relaxation is unique to magnetic nanoparticles because of their single magnetic domains (Rondinone, Samia, & Zhang, 1999). The surface of iron oxide nanoparticles is considered to behave differently than the nanoparticle core material, due to the lack of full coordination for all atomic pairs (Khanh, Hoang, & Zung, 2008). Magnetite bulk magnetization saturation is about 90 emu/g while that of nanoparticles is typically 30-50 emu/g, with the lower magnetization thought to result from a magnetic dead layer on the particle surfaces (Lu, Salabas, & Schüth, 2007).

Iron oxide nanoparticles are currently under research for use in environmental (W. Zhang, 2003), medical (Binder & Weinstabl, 2007; S Mohapatra, Mallick, Maiti, Ghosh, & Pramanik, 2007; Sen, Magdassi, Nizri, & Bruce, 2006; Yoo et al., 2007), and electronic (Santoyo-Salazar, Castellanos-Roman, & Beatriz Gómez, 2007; Zheng, Gu, Xu, Fung, & Zhang, 2005) applications. In addition to co-precipitation, modern synthesis techniques include microemulsion, hydrothermal synthesis, and thermal decomposition, as seen in Table 1.

Table 1 Common iron oxide nanoparticle synthesis techniques (Modified from Lu, Salabas, Schüth 2007)

| Synthetic method | Synthesis | Temp. [C] | Time | Solvent | Ligand addition | Size distribution | Shape control | Yield |
|------------------|-------------------------|-----------|----------------|---------------|-----------------|-------------------|---------------|---------------|
| co-precipitation | very simple, ambient | 20-90 | minutes | water | during or after | relatively narrow | not good | high/scalable |
| thermal decomp. | complicated, inert atm. | 100-320 | hours-days | organic | during | very narrow | very good | high/scalable |
| microemulsion | complicated, ambient | 20-50 | hours-days | organic | during | relatively narrow | good | low |
| hydrothermal | simple, high pressure | 220 | hours ca. days | water-ethanol | during | very narrow | very good | medium |

Synthesis conditions directly control the size distribution of the nanoparticles (J. Liu et al., 2009; Vayssieres, 2005). Particle growth occurs in two phases; the nucleation phase must be shortened and separated from the growth phase in order to obtain monodisperse nanoparticles (Laurent et al., 2008; J. Park et al., 2005). There are many techniques that control the average

diameter of magnetite particles and lower their polydispersity (Kahani & Jafari, 2009; J. Park et al., 2004, 2005). Nanoparticles synthesized in organic solvents usually have higher crystallinity and better monodispersity than those synthesized in aqueous solution (Gubin & Kataeva, 2006). The nanoparticles created using the Massart co-precipitation method in the presence of an external magnetic field were found have the same size, shape, magnetic and chemical characteristics as those created in the absence of an external magnetic field (Vereda, Vicente, & Hidalgo-Alvarez, 2007).

Magnetite has a point of zero surface charge (pH_{pzc}) of about 6 or 6.5 at room temperature (Z. Sun, Su, Forsling, & Samskog, 1998; Vereda et al., 2007) and a pH_{pzc} of 5.4 at 90 °C (Cornell & Schwertmann, 2003). Magnetite's pH_{pzc} is highly sensitive to impurities such as chloride ions and carbon dioxide (Cornell & Schwertmann, 2003). A diagram of hydrogen and hydroxide uptake and release by iron oxide surfaces as a result of solution pH is given in Figure 1.4 (Cornell and Schwertmann 2003).

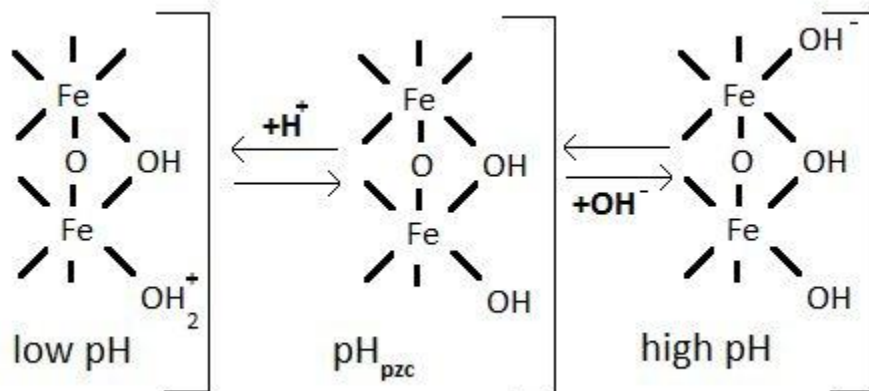


Figure 1.4 Iron oxide surface charges, from low pH to high pH (modified from Cornell and Schwertmann 2003).

Iron oxides have a positive surface charge in solutions with a pH lower than their pH_{pzc} , and can form chemical bonds with anions or anionic functional groups attached to ligands, with non-stoichiometric proton uptake (Cornell & Schwertmann, 2003). It is thought that the Langmuir adsorption curve of ligands onto iron oxides indicates a singly coordinated iron oxide surface hydroxyl group (Cornell & Schwertmann, 2003).

The pH corresponding to maximum adsorption results from the competing effects of increased surface FeOH^{2+} groups at low pH and increased anionic conjugate forms of the acid at higher pH (Cornell & Schwertmann, 2003). A kinetic study of goethites with varying crystallinities determined that adsorption of phosphate ligands proceeds by an initial fast stage and then a slow stage lasting hours to days, with the slow phase corresponding to ligand diffusion into pores, crevices, and aggregates of particles (Cornell & Schwertmann, 2003).

The bonding strength of iron oxide nanoparticles' bonds to common ligand head groups is in the order: phosphates > carboxylates > hydroxyls > sulfonates (Cornell & Schwertmann, 2003; Sahoo et al., 2001). Sulfonic acid bonds to iron oxide are significantly weaker than carboxylic and phosphonic bonds (Cornell & Schwertmann, 2003; Portet, Denizot, Rump, Lejeune, & Jallet, 2001; Vekasa, Bica, & Avdeev, 2007). The extra positive charge on phosphates results in the strongest ligand bonds to magnetite surfaces with the highest ligand packing densities (Duan et al., 2008). Some groups report that phosphate binding results in substantially decreased magnetic properties (Shafi, Ulman, Yan, Yang, & Estourne, 2001; Yee et al., 1999), although there is some disagreement (Daou et al., 2008). Proton relaxivity studies have indicated that carboxylic acid attachment to nanoparticle surfaces can improve magnetic properties (Guardia, Batlle-Brugal, & Roca, 2007) by increasing the coordination of surface iron oxide atoms (Duan et al., 2008), while other studies have indicated that the iron oxide surface loses magnetic strength from carboxylic ligand attachment (Ino, Nanodelcev, & Drmota, 2008). In-situ infrared spectroscopy has indicated that the carboxylate oxygens coordinate symmetrically to the nanoparticle surface (Ino et al., 2008). Carboxylic acids and other ligands are thought to rearrange the surfaces of metal oxide nanoparticles (Laurent et al., 2008; Rajh et al., 2002).

Typical nanoparticle ligands are straight chain alkanes attached to carboxylic and amine functional groups, soluble in many organic solvents but insoluble in water (Kalescky, Shinoda, Moore, & Nielsen, 2009; Neouze & Schubert, 2008; Theppaleak, Tumcharern, Wichai, & Rutnakornpituk, 2009). Longer alkyl chains were found to provide better stability, and this was attributed to increased van der Waals forces between the bigger ligands and a lower incidence of ligands collapsing back onto the nanoparticle surface (Avdeev et al., 2007).

Recently, molecular and polymeric ligands with multiple carboxylic acid functional groups such as citric acid have become commonly used in iron oxide production for biomedical applications (Adachi et al., 2009; Neouze & Schubert, 2008; Sahoo et al., 2001; Yu & Chow, 2004). A molecular dynamics study of such hydrophilic nanoparticles has shown that the curvature of the particle water interface leads to a negative free energy of hydration for very small diameters and increasingly negative with increasing particle size, thus controlling the shape and size of aggregates in solution (Chiu, Moore, Shinoda, & Nielsen, 2009).

Protecting against corrosion is an important challenge because magnetite nanoparticles can dissolve in acidic or alkaline media and also oxidize to maghemite (J. Park et al., 2005). The oxidation of Fe^{2+} decreases in the presence of inorganic ligands in the order perchlorate > fluoride > nitrate > chloride > carbonate > sulfate > silicate > phosphate (Huang & Wang, 1997). Achieving long-term stability requires ligands with functional groups that coordinate to nanoparticle surfaces along with long chain groups to prevent aggregation (Theppaleak et al., 2009). Stability is weaker with smaller ligands, while polymeric ligands are thought to be more stable (Kikura, Matsushita, Matsuzaki, Kobayashi, & Aritomi, 2004; Laurent et al., 2008; Neouze & Schubert, 2008).

Nanoparticle ligands can be functionalized prior to or after nanoparticle attachment, and can be partially or completely exchanged for other ligands (Binder & Weinstabl, 2007; Binder, Weinstabl, & Sachsenhofer, 2008; Lattuada & Hatton, 2007; Neouze & Schubert, 2008). Ligands chemisorbed to a nanoparticle surface can form a bi-layer with additional ligands that lack direct bonding to the nanoparticle surface, as shown in Figure 1.5 (Neouze & Schubert, 2008; L. Shen, Laibinis, & Hatton, 1999; Vekasa et al., 2007). A schematic of ligand modification before and after nanoparticle attachment is shown in Figure 1.6 (adapted from Neouze & Schubert, 2008).

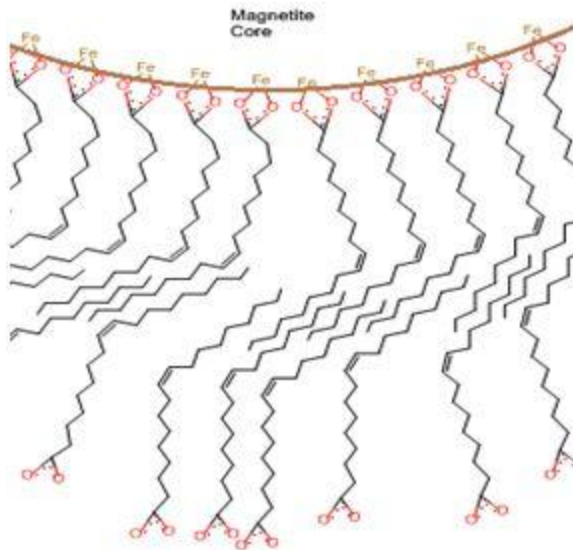


Figure 1.5 An example of bi-layer surfactant formation around a nanoparticle

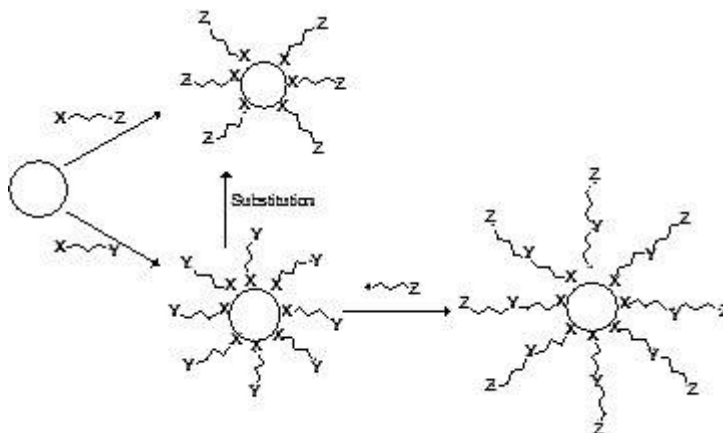


Figure 1.6 Ligand functionalization before and after nanoparticle attachment (adapted from Neouze & Schubert 2008)

Recently, diacetylene ligands were photopolymerized after nanoparticle attachment so as to create a polymerized layer on magnetite nanoparticle surfaces that provides resistance to chemical and thermal degradation (Bartczak & Kanaras, 2010; Vinod, Chang, Kim, & Rhee, 2008). Other promising techniques of enhancing functionalized nanoparticle stability include the use of steric methyl groups and the polymerization of functionalized benzene groups (Herbert, Wang, Schomäcker, Schlögl, & Hess, 2009; Luo, Ma, Zhang, & Carr, 2008; Schuster, Kreuer,

Andersen, & Maier, 2007; Shi, Xue, Li, & Jin, 1994; Summers & Eastoe, 2003; Y. Wang, Teng, Wang, & Yang, 2003; Yoshioka, Nakahara, & Fukuda, 1985).

1.7 Silica Coating of Magnetite Nanoparticles

An alternative method of stabilizing and functionalizing magnetite nanoparticles involves coating the particles with an inorganic layer such as silica. The coating of magnetite with a silica layer improves chemical stability and prevents aggregation (Laurent et al., 2008). Magnetite nanoparticles coated in silica underwent surface oxidation to form gamma phase maghemite when calcined at 700 °C for six hours, but the magnetic properties were only slightly degraded (J.-N. Park, Zhang, Hu, & McFarland, 2010).

Trialkoxysilanes are commonly used for the attachment of ligands to nanoparticle surfaces and can be directly attached to magnetite surfaces or alternatively attached to a silica layer which covers the nanoparticle (Neouze & Schubert, 2008; X.-C. Shen, Fang, Zhou, & Liang, 2004; C. Zhang et al., 2007). Silica-coated magnetic nanoparticles have also been successfully functionalized with acid and base groups so as to yield superparamagnetic solid acid catalysts (Gill, Price, & Jones, 2007; Lee et al., 2008; Phan & Jones, 2006).

Coating the magnetite nanoparticles with citric acid or poly(ethylene glycol) has been shown to improve homogeneity of the silica layer and hinder the agglomeration of particles during silica deposition (Lin & Haynes, 2009; Yongkang Sun et al., 2005). Silica increases the loading density of trialkylsilane ligands on iron oxide nanoparticles, but reduces magnetic properties by adding diamagnetic weight (Kralj, Makovec, Čampelj, & Drogenik, 2010). The magnetization of the iron oxide nanoparticles is thought to be higher (per gram of iron oxide) with a silica coating than with carboxylate bonded ligands (Häfeli, Zborowski, Woo, Hong, & Ahn, 2005). Reaction conditions important to the formation of silica coatings on magnetite nanoparticles include the temperature, ratio of alcohol-to-water, type of alcohol, and the amounts of silicate and catalyst in solution (Deng, Wang, Hu, Yang, & Fu, 2005).

Sonochemical synthesis is the only technique that has been successful in creating silica-coated magnetite particles with almost exclusively single magnetic cores and additionally a

higher saturation magnetization than particles from silent synthesis conditions (Morel et al., 2008). The sonochemically synthesized particles were not checked for stability in acidic media (Morel et al., 2008). DFT calculations have shown that hydrolysis of linear molecular silica chains begins in the middle and then spreads to the ends, and that silica molecular rings are less stable than linear chains when in the presence of water (Wei, Zhang, & Liu, 2008).

Even under sonochemical synthesis conditions, there are limits to the concentrations of TEOS and magnetite beyond which multiple cores are contained in each silica shell (Kralj et al., 2010). Accordingly, there are many techniques and processing conditions which have been shown to produce uniform silica shells with cores composed of multiple iron oxide nanoparticles (Do Kim, Kim, Choa, & Kim, 2007; J. Park et al., 2005; Santra et al., 2001).

1.8 Functionalization strategies

Environmentally friendly, economically viable processing of biomass requires facile separation of the acid catalyst. The presence of insoluble lignins and recalcitrant cellulose in biomass presents a problem even for the most efficient solid acid catalysts, which must be separated by centrifugation or filtration (Lai, Deng, Guo, et al., 2011). A solution to this problem may be provided by superparamagnetic iron oxide nanoparticles (SPIONS), which can be separated from solution by an external magnetic field, then redistributed in solution after the external field is removed. SPIONS are a promising substrate for the attachment of acid groups, providing both high surface area and a facile method of separation. The elimination of centrifugation and filtration from the processing steps may reduce the costs associated with particle separation, particularly in the case of biomass. The guiding principles for our development of this acid catalyst technology are to attain 1) high activity and stability in aqueous solutions at temperatures of interest, 2) a synthetic flexibility enabling the attachment of various outward-facing catalytically active moieties, and 3) a synthetic framework compatible with inexpensive industrial-scale catalyst production.

Recently, a material composed of ordered mesoporous silica encasing SPIONS was synthesized and used to hydrolyze cellulose (Lai, Deng, Li, et al., 2011) and biomass (Lai, Deng, Guo, et al., 2011); however, the catalyst required regeneration with H₂SO₄ after each run. While

silica-functionalization has resulted in some success, silica functionalizations of iron oxide nanoparticles have so far failed to demonstrate the stability desired for biomass hydrolysis and other industrial applications (Bootsma, Entorf, Eder, & Shanks, 2008; Kralj et al., 2010; Peña et al., 2011). Silica functionalization technology is also employed for acid functionalization of SPIONS through polymerization methods. However, schemes which utilize an initial silica functionalization in order to attach a polymerization initiator molecule to the particle surface have been unable to overcome the problems of acid group detachment and degradation (Long & Jones, 2011), and attempts to avoid a silica layer by using direct attachment of an organic ligand have been shown to require substantial cross-linking in order to maintain the iron oxide's magnetic properties (Feyen, Weidenthaler, Schüth, & Lu, 2010). If such cross-linking decreases the contact between inner acid groups and insoluble reactants, it may restrict the applicability for cellulose hydrolysis.

Catalyst stability is a critical improvement required to enable the industrial application of acid functionalized SPIONS. As an alternative to silica functionalization, the magnetite's amphoteric surface can be functionalized directly, by forming bonds between the magnetite's surface hydroxyl groups and specifically coordinating moieties. A single ligand can contain a functional group for binding to the nanoparticle surface and an additional functional group facing outward into solution. For example, di-sulfonic acids can attach to magnetite so as to leave one sulfonic acid group exposed to solution (Portet et al., 2001). Such di-acid functionalization schemes are limited by the sulfonic acid group's weaker binding affinity toward the magnetite surface and resulting lack of ligand-SPION bond stability (Cornell & Schwertmann, 2003; Portet et al., 2001; Vekasa et al., 2007). Many ligands bound directly to magnetite nanoparticles have high thermal stability in air, but tend to dissociate into solution in the absence of excess ligand (Sahoo et al., 2001). This thesis studies ligated SPIONS as acid catalysts for hydrolytic sugar production.

Chapter 2 - Experimental Details

2.1 Precipitation of Magnetite Nanoparticles

Iron oxide nanoparticle cores were synthesized using Massart's aqueous co-precipitation method (Massart, 1981; Sahoo et al., 2005). Iron (II) chloride and iron (III) chloride in a 1:2 molar ratio were precipitated with ammonium hydroxide at 80°C, heated for 30 minutes, and then sonicated for 10 minutes.

Particle precipitation was conducted in the absence of oxygen to control the oxidation of Fe^{2+} to Fe^{3+} . The iron chlorides could only be weighed out within the nitrogen environment of the glovebox where they were stored along with a tightly sealed bottle of de-oxygenated water. The de-oxygenated water was prepared by heating de-ionized water to boiling, then bubbling nitrogen through the water as it cooled to room temperature for a minimum of 30 minutes. That water was contained in a glass jar with a tight-sealing lid capable of maintaining a seal through the vacuum pressure of the transfer chamber while being added into the glovebox. The water level was close to the top of the glass jar during transfer to the glove box to minimize oxygen introduction.

Along with the de-oxygenated water, the following items were added through the transfer chamber: a 3-necked flat-bottom flask with 3 appropriately sized septa, a tightly sealed bottle of ammonium hydroxide, a stirbar, funnel, weighing trays, paper towels, a spatula, and a graduated cylinder to measure the water. The two side septa were closed prior to introducing the 3-necked flask, because the single middle neck was sufficient for adding the reagents.

After four vacuum/nitrogen-fill cycles of the transfer chamber and introduction of the reagents to the glovebox, the appropriate weights of iron chloride were weighed out and combined in the 3-necked flask. Next, the appropriate volume of water was added to the flask, along with the stir-bar, and the middle septum was sealed carefully to prevent oxygen contamination during the precipitation. Typically, 0.86g of iron (II) chloride tetrahydrate and 2.35g of iron (III) chloride hexahydrate were added to 40mL of water (with the subsequent addition of 5mL of ammonium hydroxide in the precipitation step as discussed below).

The sealed 3-necked flask was removed from the glovebox and placed in a hot oil bath which increased the flask temperature to 80°C over a period of approximately 20 minutes. The oil trap/tubing was vented with nitrogen gas, and the tubing needle was inserted through a side septum. A syringe was filled with ammonium hydroxide, with care taken to prevent the introduction of air into the needle. With the iron chlorides at 80°C, the ammonium hydroxide was added through the middle septum. Care was taken to ensure that the gas trap needle was open for quick release of excess gas, the flask was well-sealed, and the syringe was sealed and did not contain air or other contaminants. The ammonium was added rapidly to a solution being stirred at 500 rpm, and the flask was manually shaken after ammonium addition, to minimize the polydispersity of the precipitated particles. After 30 minutes of additional heating at 80°C, the particles were sonicated for 10 minutes.

Next, the pH was adjusted by adding HCl through one of the necks in the 3-necked flask. A metal tube inserted through a septum in the third neck was used to create positive nitrogen pressure inside the flask and a slight bubbling in the oil trap. The nitrogen flow during addition of ligands and hydrochloric acid was necessary to prevent contamination with air. The same septum holding the needle connecting the flask to the oil trap was used to hold the needle connecting the flask to a nitrogen gas cylinder. The acid was added by a sealed glass syringe into the septum of the sealed flask, with the pH meter probe inserted for measurement of the pH.

2.2 Sonication

A Sharpertek Model: SH80-2L sonicator with an ultrasonic frequency of 40 kHz and 380 W of power was used during ligand functionalization of the precipitated iron oxide particles. Such sonication can remove particles stuck to the surfaces of the synthesis vessel, help break apart agglomerates to some extent (Siddiqui et al. 2009), and thus possibly increase the particle surface area accessible to ligands in solution. The water in the sonicator was heated at 60°C in order to minimize cooling of the particle solutions during sonication. According to the manufacturer, heating the sonication bath water to higher temperatures is not recommended due to the formation of vapor bubbles which reduce the power of the ultrasonic vibrations.

2.3 Dialysis and Magnetic Washing

Dialysis tubing was used to remove excess ligands from some of our early batches of particles. A section of dialysis tubing (Thermo Scientific SnakeSkin 7K) was unrolled and crimped at the bottom end, soaked in DI water for 24 hours, then filled with the solution of particles to which ligands had been attached. The bulk DI water surrounding the tubing was measured for pH as an estimate of ligand diffusion. When the bulk water pH stabilized, the ligands were no longer diffusing from inside the dialysis tubing. Such stabilization took as long as two weeks for some of the early synthesis batches. During the functionalization of 11-sulfoundecanoic particles, we began to use the method of magnetic separation and washing.

Magnetic washing was conducted at least 10 times to remove excess ligand. The catalyst was stirred in de-ionized water and then exposed to a magnetic field which would remove the particles from solution while leaving the water-soluble excess ligands in the supernatant. The length of time for which the particle suspension was left in the 3661 Gauss magnetic field of the neodymium supermagnet was determined by the darkness of the supernatant, which was used as a quick source of information on how much catalyst would be lost if the supernatant was discarded at that time.

Some smaller particles were likely lost during the magnetic washing that would not be lost with dialysis. This may have resulted in a larger particle diameter measured by XRD calculations and TEM images. The supernatant above the magnet did not always clear completely during a reasonable washing step timeframe such as one hour, and some suspended particles were lost when the supernatants were discarded. However, if smaller particles were going to be lost, it may have been preferable to lose them before reaction, and to quantify the recyclability of only those particles which were more easily magnetically separated.

2.4 Diffuse Reflectance Infrared Fourier Transform Spectroscopy (DRIFTS)

DRIFTS was conducted on a Thermo Nicolet NEXUS 870 spectrometer with a ZnSe window, operated by the software program OMNIC. Samples were dried at 50°C for 48 hours. KBr was ground up by mortar and pestle, loaded in the sample chamber to flush with dry air for 15 minutes, and used for a background scan. Immediately after the background scan, the KBr

was added to approximately 0.01mg of dried sample, ground up by mortar and pestle, and returned to the cell for another 15 minutes of dry air flushing, followed by scanning the sample. 50 scans were taken with a resolution of 4 cm^{-1} over the range from $650\text{-}4000 \text{ cm}^{-1}$.

2.5 X-Ray Photoelectron Spectrometry (XPS)

X-ray photoelectron spectroscopy (XPS) data were obtained with a PerkinElmer PHI 5400 using achromatic AlK α radiation (1486.6 eV). Spectra were obtained under vacuum pressure of less than 8.0×10^{-8} Torr. XPS binding energies were measured with a resolution of 0.025-0.1 eV, and a precision of ± 0.1 eV. The analyzer pass energy was 17.9 eV, with a contact time of 50-100 milliseconds. XPS was used to measure the atomic surface concentrations of various samples for comparison, as well as to measure the binding energy in high resolution images of particular orbitals. Sample preparation for XPS analysis involved the grinding of the sample to a fine powder, and deposition of the fine powder on a conductive carbon tape support.

2.6 X-Ray Diffraction (XRD)

XRD analysis was conducted using a Rigaku MiniFlex II desktop x-ray diffractometer, using a fixed time scanning method with a 0.01° step size and 6 seconds counting time at each step. Crystallite sizes were calculated using the Scherrer formula:

$$\text{Equation 1 } d_{\text{domain}} = 0.9\lambda/\beta \cos \Theta$$

where d_{domain} is the crystallite diameter (nm), 0.9 is a dimensionless shape factor, λ is the x-ray wavelength (nm), β is the line broadening for the full width at half maximum (FWHM), and Θ is the Bragg angle. The crystallite size was used as an approximation of the magnetite particle size, as described by other investigators (Sahoo et al., 2005).

2.7 Transmission Electron Microscopy (TEM)

Transmission electron microscope (TEM) images were used to estimate the size distribution of the nanoparticles. A model CM100 TEM (FEI Company, Hillsboro, OR), equipped with an AMT digital image capturing system, was operated at 100 kV. The images were taken of dispersed particles deposited from aqueous solutions by contacting a drop of liquid with Formvar/carbon-coated, 200-mesh copper grids (Electron Microscopy Sciences, Fort

Washington, PA) for 30 seconds at room temperature. Nanoparticle mean diameters for TEM images were calculated by hand and using the software ImageJ, available from the National Institute of Health.

2.8 Acid-Base Titration

The measured acid loading was averaged from three titrations of 0.05 g catalyst with 0.01M NaOH, with variations of ± 0.02 mmol H⁺/g between measurements. Early in the project, titrations indicated that the dried particles gave significantly lower acid loadings than if they were kept in aqueous solution. A procedure was adopted in which the catalyst was never dried, and wet solutions of known catalyst concentration were used for all titrations and reactions. The likely reason that dried particles gave lower acid loadings than un-dried particles was the increased agglomeration seen in TEM images, and the reduction of acid sites accessible to ions in the solvent solution.

2.9 Dynamic Light Scattering (DLS)

Particle agglomerate measurements were taken on a ZetaPALS Zeta Potential Analyzer (Brookhaven Instruments Corporation) with hydrodynamic light scattering. Catalyst solutions were diluted by placing 1 drop of catalyst solution into 1.5-2mL of 2% sucrose solution.

2.10 Zeta Potential Analysis

The Zeta potential analysis was determined with a Zeta Potential analyzer from Brookhaven Instruments Corporation. Measurements were recorded at 28°C. Samples were suspended in double distilled water with 0.05-0.2 mg/mL concentrations (pH 6.8). Measurements were carried out with a Pd electrode using Phase Analysis Light Scattering mode. The Zeta potential was automatically calculated from electrophoretic mobility based on the Smoluchowski equation:

$$\text{Equation 2 } \xi = v / (\epsilon E / \eta)$$

where ξ is the Zeta potential, v is the measured electrophoretic velocity, η is the viscosity, ϵ is the electrical permittivity of the electrolytic solution and E is the electric field.

2.11 Thermogravimetric Analysis (TGA)

Samples were analyzed in a PerkinElmer Pyris1 TGA (Norwalk, CT), using 5-10 mg heated under a nitrogen atmosphere from 50°C to 600°C, typically at 10°C/min with a pause at 120°C to allow for a reduction of water content prior to reaching the temperature range associated with ligand desorption and decomposition. TGA weight loss is calculated as the change in weight between 120°C and 600°C.

2.12 Weight Measurement of Wet Catalyst

During the development of procedures in the beginning of the project, TEM images indicated severe agglomeration upon drying, and titration indicated severely hindered solvent access to acid sites. Even after letting the dried particles sit for 48 hours in 0.01M NaCl solution, the acid site measurement was about 10% of the loading measured for particles that were not dried. For these reasons, throughout the project, the particles were kept in aqueous solutions from synthesis through reaction cycles. After washing, the catalyst was kept in aqueous solution and stirred rapidly for 20 minutes at 300 rpm or higher during measurement of the catalyst dry weight per wet solution weight. Three vials of different proportions were weighed out, and their size/shape/weights were recorded. The dry vials were weighed, filled with 1-5 mL of catalyst solution, re-weighed to get the wet solution weight, and then dried in an oven at 80°C until the water was completely evaporated. The dried vials were weighed again, and the catalyst dry weight was then used to calculate the catalyst dry weight % of the aqueous solution. The dry weight % of the aqueous nanoparticle solution was then used to calculate the mass of solution needed for various catalytic reaction experiments or titrations. The appropriate weight of wet solution was extracted under 300 rpm or greater stirring speed, after vigorous stirring, in order to maintain a uniform distribution of particles throughout the solution.

2.13 High Pressure Liquid Chromatography (HPLC)

Sugar analysis was conducted using an HPLC RCM-Ca²⁺ monosaccharide column (300 × 7.8 mm; Phenomenex, Torrance, CA) with a refractive index detector. The HPLC was calibrated to external standards for sucrose, glucose, fructose, and maltose, using 80°C deionized water at a flow rate of 0.6 mL/minute. During HPLC analysis, samples were alternated with known standards to ensure accuracy of the measurements.

2.14 Inductively Coupled Plasma Atomic Emission Spectroscopy (ICP-OES)

ICP-OES was conducted with a Varian 720-ES ICP Optical Emission Spectrometer. Standards were prepared from stock solutions of Fe, S, and P, and used for calibration. The lines selected for each element were Fe 259.94 nm, P 178.29 nm, S 181.97 nm. Solutions of high catalyst concentration were diluted as necessary.

Chapter 3 - Di-acid Monolayers on Polydisperse Iron Oxide Nanoparticles

3.1 Monolayers of Small Acid Molecules

Initial investigations of ligand attachment to magnetite were based around the carboxylic acid functionalization used for citric acid (Sahoo et al., 2005). Iron (II) chloride and iron (III) chloride in a 1:2 molar ratio were precipitated with ammonium hydroxide at 80°C, heated for 30 minutes, and then sonicated for 10 minutes. The sonicated particles were then heated to 95°C, and 1g of the ligand was added to 1g of iron oxide nanoparticles, which were then heated at 95°C. Snakeskin 7 kDa dialysis tubing was used to remove excess ligands and ions from the solution of functionalized particles. Carboxylic acids, sulfonic acids, and benzene rings are indicated by some researchers as necessary for high cellulose hydrolysis activity (Kitano et al., 2009). Both sulfonic acids and carboxylic acids are discussed in the literature as moieties which bond to magnetite nanoparticle surfaces (Cornell & Schwertmann, 2003; Portet et al., 2001; Yee et al., 1999). Our first batches of catalyst involved smaller, commercially available molecules such as citric acid, pyromellitic acid, 4-sulfophthalic acid, and 1,3-disulfonic acid. FTIR for some of these functionalized particles are shown in Figure 3.1.

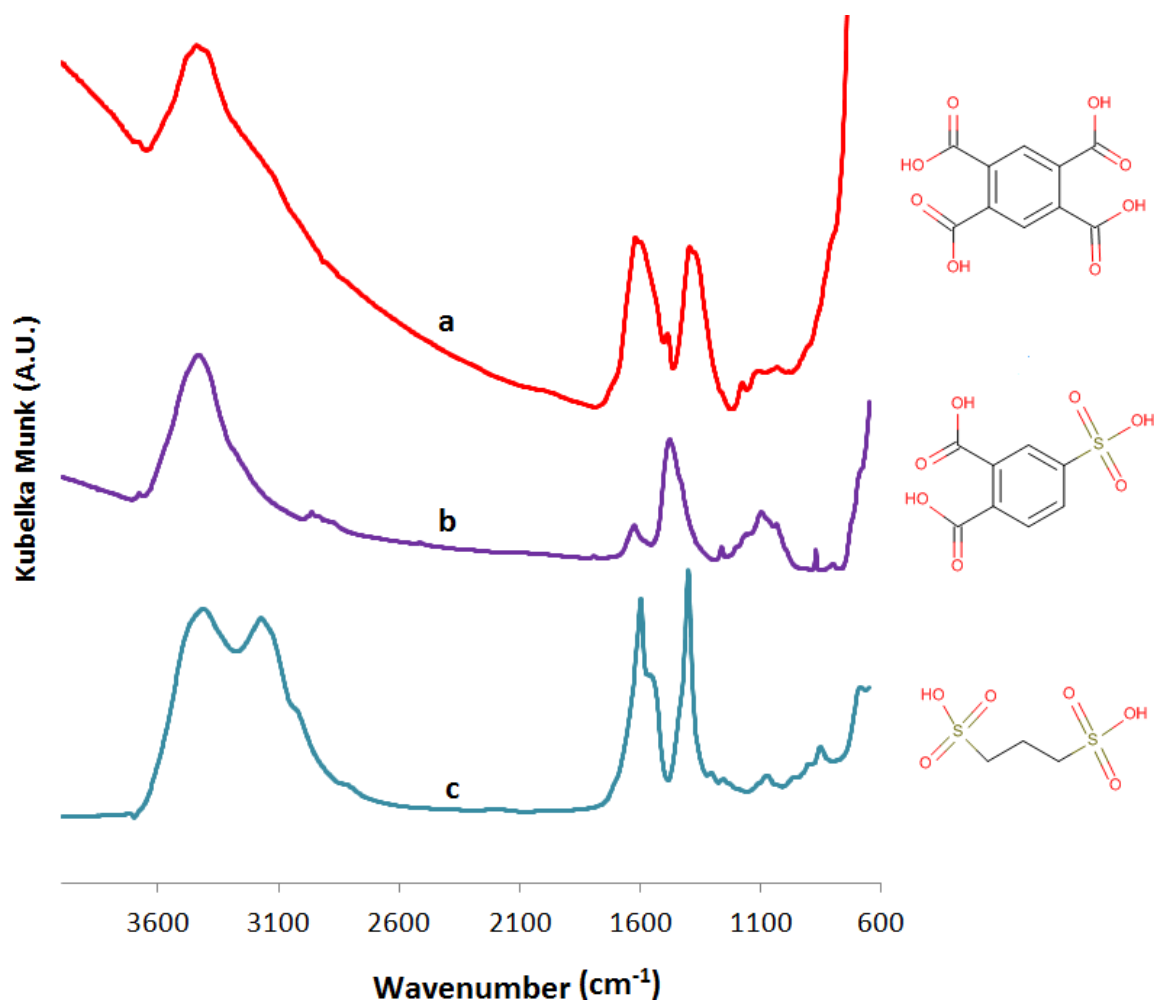


Figure 3.1 DRIFTS spectra of magnetite nanoparticles functionalized with a) pyromellitic acid, b) 4-sulfophthalic acid, and c) 1,3-propanedisulfonic acid

All three particles show the characteristic magnetite OH peak centered around 3400 cm^{-1} , and weak peaks in the range expected for hydrocarbons between $2800\text{--}3000\text{ cm}^{-1}$. The 4-sulfophthalic acid functionalized particles have peaks at 2925 and 2963 cm^{-1} which are expected for substituted benzenes. Both 4-sulfophthalic and pyromellitic nanoparticles may require careful deconvolution to discern between the vibrations of the benzene rings and those of the carboxylic acids. It appears that 4-sulfophthalic nanoparticles show peaks at 1620 cm^{-1} corresponding to COO^- symmetric stretching, and at 1480 cm^{-1} corresponding to asymmetric COO^- stretching, with the spacing of 140 cm^{-1} between the two indicating a bridging bidentate carboxylic acid binding structure (L. Zhang, He, & Gu, 2006). Peaks at 1034 and 1172 cm^{-1} correspond to RSO_3^- asymmetric and symmetric vibrations, respectively.

Pyromellitic acid nanoparticles show two or more carboxylic acid binding structures. The most prominent binding mode is monodentate with a spacing of 230 cm^{-1} between the symmetric COO stretch at 1626 cm^{-1} and the asymmetric stretch at 1396 cm^{-1} . A bridging bidentate carboxylic acid binding structure is inferred from peaks at 1626 cm^{-1} and 1487 cm^{-1} corresponding to symmetric and asymmetric COO- stretching, respectively. There also appears to be a slight shoulder around 1710 cm^{-1} , corresponding to the symmetric stretch of COOH.

The 1,3-propanedisulfonic acid nanoparticles were markedly different than the others in appearance and magnetic behavior. Instead of the characteristic black color attributable to magnetite cores, the disulfonic nanoparticles were orange and could not be extracted from solution by the magnetic field of our supermagnet. The peak near 700 cm^{-1} from Fe-O absorption is generally indicative of maghemite (Fe_2O_3), although the orange/red color is more typical of goethite (FeOOH). The additional peak around 3174 cm^{-1} in the 1,3-propanedisulfonic nanoparticle spectra may be further evidence of core oxidation.

The difficulties encountered in efforts to synthesize magnetite cores functionalized with di-sulfonic acids led us to return to the literature with the goal of determining how other groups had successfully used sulfonic acids to bind ligands to magnetite. Although some articles had been widely cited for utilizing sulfonate ligands in the capping of iron oxide nanoparticles, a careful reading of the articles suggests that sulfonates were both the weakest binding (Portet et al., 2001) and most disruptive to iron oxide magnetic properties (Yee et al., 1999). The relatively successful creation of 4-sulfophthalic nanoparticles, and the literature's indication that acid-magnetite binding strengths are in the order phosphonic > carboxyl > hydroxyl > sulfonic, pointed to the usefulness of combining stronger bonding, less catalytically active carboxyl groups with weaker binding, catalytically superior sulfonic acid groups on opposite ends of a single ligand.

3.2 Longer Chain Monolayers

We opted to synthesize a ligand with both sulfonic and carboxylic acid groups, in that sense similar to the 4-sulfophthalic acid, but with a longer alkane chain, with the goal of

increasing protection of the magnetite cores as well as shielding the magnetite-ligand bond from interactions with solvent and reagent molecules. Longer chain organic carboxylic acids have been shown to better stabilize larger diameter particles in organic solution (Avdeev et al., 2007), although this does not necessarily translate to an aqueous system with di-anionic surfactants. The first synthetic techniques we found were from the 1950's and 60's, involving higher temperatures and pressures but low yields. Our first attempts at synthesizing sulfonic-carboxylic ligands covered our Parr reactor's inside surfaces with a layer of black tarry gunk that was very difficult to clean.

3.3 Synthesis of 11-Sulfoundecanoic Acid

Fortunately, an easier, higher yield approach to synthesizing a carboxy-sulfonic ligand was found after an extensive literature search. A synthetic procedure (which is available in Chinese but not translated into English) from Cui et al. 2006 utilizes an aqueous synthesis at atmospheric pressure with relatively low temperatures and the relatively inexpensive reagents 11-bromoundecanoic acid and sodium sulfite (Cui, Cao, & Xu, 2006). This synthesis appeared useful not only for lab-scale applications, but also as a simple, scalable technique that could yield large quantities of the ligand for industrial scale catalyst production. 11-bromoundecanoic acid and sodium sulfite are available in large quantities at relatively low prices, produced from the bromination of ricolinic acid (Hofer, 2009) and the production of paper, respectively. Another pleasing aspect of the choice of 11-bromoundecanoic acid is the large number of organic chemistry reactions which are available to aid in the decoration of the outer ligand shell, by substituting nucleophiles for the bromine atom.

Following the previously established method, the 11-bromoundecanoic acid was combined with sodium sulfite in a 10:1 molar ratio and the reagents were heated at 50°C for 1 hour, 70°C for 2 hours, 80°C for 6 hours, then 90°C for 3 hours. Typically, 100g of 11-bromoundecanoic acid was combined with 475.3g of sodium sulfite in 1000 mL of water. Beyond what is described by Cui et al., there are some subtle, difficult aspects to the synthesis. The water should be heated to the initial reaction temperature of 50°C, before adding any reagents, in a round flask in an oil bath with the hotplate temperature probe monitoring the oil bath temperature. The magnetic stir bar selected should be capable of maintaining at least 1000

rpm for the hotplate. The non-water soluble 11-bromoundecanoic acid must be added slowly so as to allow it to distribute through the water without forming large clumps. Once the 11-bromoundecanoic acid is thoroughly distributed, the sodium sulfite can be added slowly and carefully.

If the sodium sulfite is added too quickly, or if stirring stops, it will form a dense, insoluble layer at the bottom of the synthesis vessel. Even when added slowly and carefully to a rapidly mixing solution, the sodium sulfite will tend to sit on the bottom of the flask, so a stirring bar should be of appropriate size and strength, so that at maximum stirring speed, it can distribute the sodium sulfite throughout the volume of solution. The reaction should be monitored periodically to make sure that the insoluble 11-bromoundecanoic acid has not formed chunks or a film on the water surface. If such chunks or film have formed, they should be broken up using a spatula, and allowed to redistribute through the aqueous solution. A Parr reactor could give better mixing, but being unable to see the reagents during reaction is a significant disadvantage because of the tendency for the sodium sulfite to clump at the bottom and for 11-bromoundecanoic to collect on the top of the solution.

The series of increasing reaction temperatures are used by Cui et al. to prevent the formation of by-products and increase the yield of the 11-sulfoundecanoic acid. At the optimized conditions and mol ratios, the process gives a yield of 97%, based on conversion of 11-bromoundecanoic acid (Cui et al., 2006). Unfortunately, separating the 11-sulfoundecanoic acid product from the excess sodium sulfite and sodium bromide salts is oversimplified in the original synthesis paper. Cui et al. simply describe a filtration separation of a heated ligand/salt mixture, and disregard the presence of salt impurities in the final ligand product.

In our lab, after the first ligand synthesis, the hot product solution was filtered through a vacuum filtration system and the resulting filter cakes were set aside. The lightest, fluffiest, whitest filter cake was selected for the particle functionalization. The filter cake's DRIFTS spectra matched the FTIR spectra reported by Cui et al. The DRIFTS spectra for that vacuum purified ligand filter cake shown in Figure 3.2 closely matches the FTIR spectra reported by Cui et al.

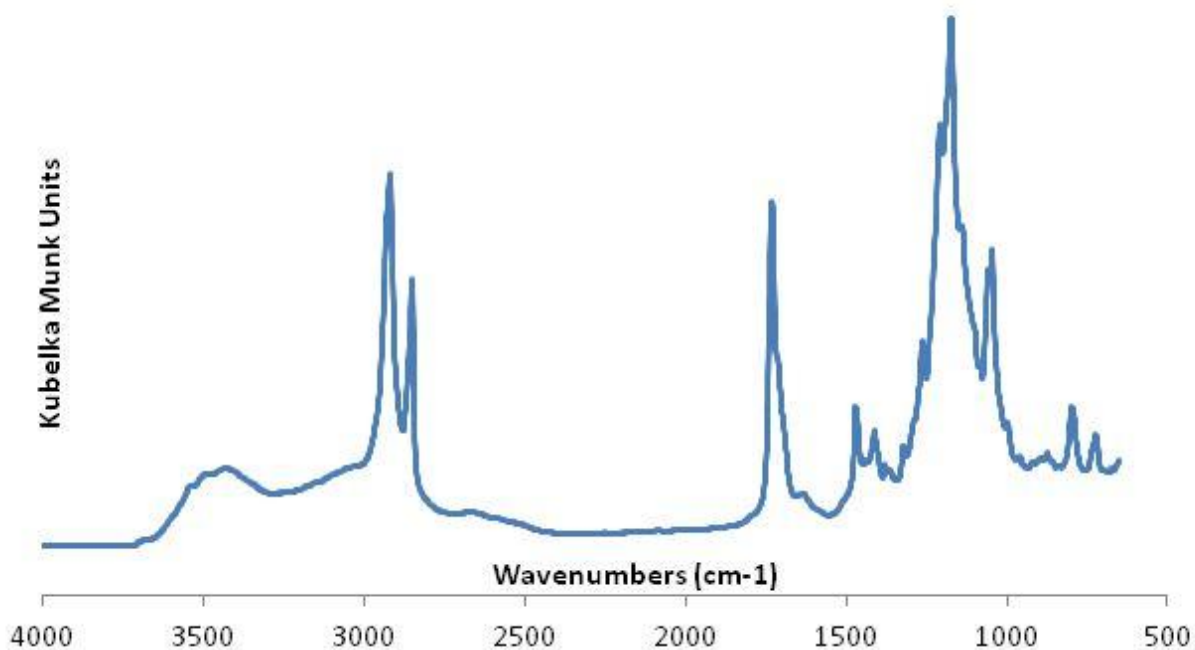


Figure 3.2 DRIFTS spectra for the synthesized, vacuum filtration-purified 11-sulfoundecanoic acid ligand.

The 11-sulfoundecanoic acid ligand peaks include a broad hydroxyl peak around 3400 cm^{-1} , alkane chain vibrations at 2850 cm^{-1} and 2918 cm^{-1} , a COOH symmetric stretch at 1730 cm^{-1} , a small peak for the COO^- symmetric stretch at 1614 cm^{-1} , CH_2 bending at 1470 cm^{-1} , symmetric RSO_3 stretching at 1174 cm^{-1} , and asymmetric RSO_3 stretching at 1045 cm^{-1} .

3.4 Purification of 11-Sulfoundecanoic acid

To increase the purity of the 11-sulfoundecanoic acid before ligation of the iron oxide nanoparticles, the product was separated from solution by first lowering the pH to 5 with HCl and filtering under vacuum at 50°C, then placing the filtrate in an oven and heating for one week at 80°C to fully oxidize the sodium sulfite impurity salt into sodium sulfate. The oxidized precipitate was then placed in concentrated hydrochloric acid solution and centrifuged to precipitate the purified ligand and leave the remaining sodium sulfate and sodium bromide in the concentrated acid solution. Full oxidation of the sodium sulfite is necessary to ensure that hydrochloric acid addition does not produce dangerous sulfur trioxide gas. The centrifugation was repeated three times. Then, the precipitated ligand was vacuum dried overnight at room

temperature to remove excess HCl. Surprisingly, XPS analysis indicated a sodium atomic concentration above 5%, indicating that the washing process did not achieve the desired level of ligand purification. Whether the sodium was present as sodium sulfate or a sulfonate/carboxylate sodium salt is unknown.

3.5 Synthesis of 10-Phosphono-1-Decanesulfonic Acid

10-phosphono-1-decanesulfonic acid was synthesized by Dr. Paul Rillema's group at Wichita State University. The procedure is illustrated in Figure 3.3.

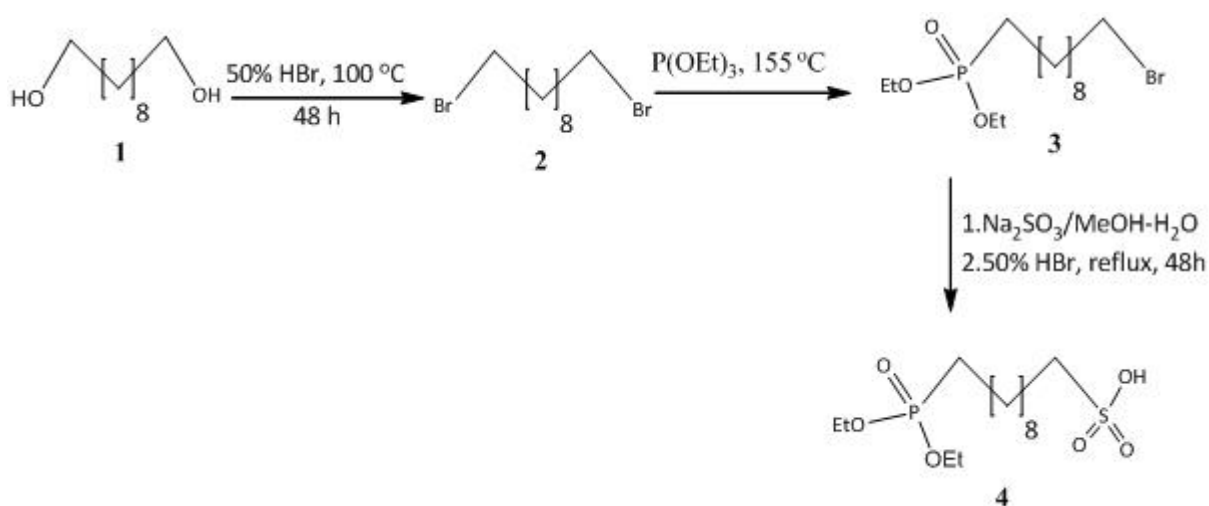


Figure 3.3 Sequence of steps(De, Aswal, & Ramakrishnan, 2010; Taffa, Kathiresan, & Walder, 2009; X. Wang & Lieberman, 2003) used to prepare diethyl(sulfonyldecyl)phosphate (4).

3.5.1 Synthesis of 1,10-Dibromodecane (2)

The intermediate compound, 1,10-dibromodecane, was synthesized by a modification of a previously published procedure (De et al., 2010). 1,10-butanediol (1) (16.0 g, 45.0 mmol), HBr (160 mL of 49 % HBr in H₂O) and water (80 mL) were added to a round-bottomed flask. The reaction mixture was stirred at 100 °C for 48 h. After the reaction was complete, it was extracted with chloroform and the chloroform layer was washed with brine, followed by stirring over sodium bicarbonate. Then it was filtered and passed through Na₂SO₄. The obtained compound was purified by column chromatography on silica gel eluting with 3:1

cyclohexane/ethylacetate mixture to give 23.72 g (86 %) of 1,10-dibromodecane as a white crystals.

$^1\text{H NMR}$ (δ , ppm, CDCl_3): 1.46 (m, 12H, CH_2) $_6(\text{CH}_2\text{CH}_2\text{Br})_2$, 1.85 (m, 4H, - $(\text{CH}_2\text{CH}_2\text{Br})_2$), 3.40 (t, 4H, $-\text{CH}_2\text{Br}$).

3.5.2 Synthesis of Diethyl (10-Bromodecyl) Phosphonate (3)

Diethyl (10-Bromodecyl) phosphonate was synthesized following the procedure described by Wang and Lieberman (X. Wang & Lieberman, 2003). A 100-mL three-necked round-bottomed flask was charged with 20 g (66 mmol) of 1,10-dibromodecane. A reflux condenser was attached, and the system was purged with argon. The flask was heated to 155 °C in an oil bath, and then 2.38 mL (14.33 mmol) of triethyl phosphite was added dropwise via a syringe over 8 h. The reaction was cooled to room temperature, and a white precipitate formed. The product was separated from the precipitate by filtration and purified by flash column chromatography with a gradient of neat hexane to 1:1 hexane/ethyl acetate yielding colorless oil 2.2 g, 44% yield. $^1\text{HNMR}$ (δ ppm, CDCl_3) 1.28-1.40 (unresolved coupling, eight CH_2 groups), 1.30 (t, J) 6.9 Hz, $-\text{OCH}_2\text{CH}_3$) combined integral 21.3H, 1.85 (m, 2H, PCH_2), 3.40(t, J) 6.9 Hz, 2H, BrCH_2 -), 4.10 (m, 4H, $-\text{OCH}_2\text{CH}_3$).

3.5.3 Synthesis of Diethyl (Sulfonyldecyl) Phosphonate (4)

The desired compound was synthesized following a report in the literature (Taffa et al., 2009). Diethyl(10-bromodecyl)phosphonate (2 g, 6.4 mmol) in 20 mL CH_3OH and a saturated solution of Na_2SO_3 (2.093 g, 16.4 mmol) in water were first refluxed for one hour and heated to 120 °C until the solvent solution was evaporated. The residue was then slurried with CH_3OH under reflux, and then the hot solution was filtered. The filtrate containing the sodium salt was then evaporated and the residue was acidified with 80 mL 50% HBr and was refluxed for 48 h. The acid was allowed to evaporate slowly under reduced pressure yielding a pale-black powder yielding 1.32 g (81%).

$^1\text{H NMR}$ (δ ppm, D_2O): 4.60 (q, $-\text{OCH}_2\text{CH}_3$ -, 4H), 2.79 (t, $-\text{CH}_2-\text{SO}_3$, 2H), 1.64 (t, $-\text{CH}_2\text{PO}$ -, 2H), 1.52 (t, $-\text{CH}_2\text{CH}_3$, 6H), 1.47 (p, $-\text{PCH}_2\text{CH}_2-(\text{CH}_2)_6-\text{CH}_2\text{CH}_2\text{S}$ -, 4H), 1.21 ($-(\text{CH}_2)_6$ -unresolved coupling, combined integral, 12H).

3.6 Nanoparticle Synthesis and Functionalization

Iron oxide nanoparticle cores were prepared using the co-precipitation method (Massart, 1981; Sahoo et al., 2005). Iron (II) chloride and iron (III) chloride in a 1:2 molar ratio were precipitated with ammonium hydroxide at 80°C, heated for 30 minutes, and then sonicated for 20 minutes.

To functionalize the iron oxide nanoparticles, 1g of the synthesized di-acid ligand was added to 1g of the sonicated particles. The mixture was sonicated for 10 minutes, and then heated to 95°C for 30 minutes. The 95°C particles were sonicated for an additional 10 minutes, then returned to the oil bath. After 24 hours of stirring at 95°C, the solution was allowed to return to room temperature under constant stirring for 12 hours, then reheated to 95°C and stirred for another 24 hours, and then again allowed to return to room temperature.

To remove unbound ligands, the nanoparticles were repeatedly washed with water and magnetically extracted from solution. The washwater was initially clear and then on subsequent washes became darker as the particles became increasingly difficult to separate from solution. As the concentration of unbound ligand in the supernatant decreased during the washing process, the supernatant did not become clear in the presence of the neodymium supermagnet (with a field strength of 3661 Gauss).

After 5 washes, the phosphonic-sulfonic nanoparticle (PSNP) supernatant, which was not clear, was measured by DLS as 50 nm agglomerates. The separable particles, when re-suspended, also measured as 50 nm agglomerates. Increasing the concentration of re-suspended particles did not increase the measured size of particle agglomerates, possibly indicating that individual particles were present in solution, instead of agglomerates. The combined supernatant/particle mixture was then subjected to centrifugation (10,000 rpm for 1 hour at 4°C). The supernatant was discarded, and the centrifuged solid was then re-suspended in DI water and vigorously agitated for 5 minutes. The centrifugation-washing was repeated twice more.

Washing the carboxylic-sulfonic nanoparticles (CSNPs) five times gave a suspension which was not fully separable by the supermagnet. After a few days of sitting at room

temperature, the particles had agglomerated to the stir bar magnet, leaving a clear supernatant. They were washed another 5 times by supermagnetic particle separation to further remove unbound ligand. The PSNPs and CSNPs were not dried after washing. Instead, a washed catalyst solution of known catalyst dry weight concentration was added to DI water to obtain reaction solutions.

3.7 Catalyst Characterization

DRIFTS spectra of the ligands, CSNPs, and NaOH neutralized PSNPs are shown in Figure 3.4. RSO_3^- and RPO_3^- groups appeared around 1050 and 1180 cm^{-1} due to asymmetric and symmetric vibrations, respectively (Yee et al., 1999). Both functionalized iron oxide nanoparticles have a peak at 1467 cm^{-1} corresponding to the CH_2 scissoring bend (Yee et al., 1999). For CSNPs, an overlapping peak at 1544 cm^{-1} is due to asymmetric COO^- stretching. The CSNP peak at 1626 cm^{-1} corresponds to COO^- symmetric stretch. The distance between the asymmetric and symmetric COO^- peaks being less than 110 cm^{-1} is an indication of chelating bidentate attachment (L. Zhang et al., 2006) or chelating mononuclear attachment (Roonasi & Holmgren, 2009). When carboxylic acid COOH groups are uncoordinated, a peak around 1710 cm^{-1} is present (Shafi et al., 2001; Yang, Peng, Wen, & Li, 2010). The peak for free carboxylic acid is observed in the 11-sulfoundecanoic acid. The lack of this peak in the spectrum of the CSNPs indicates a lack of free COOH . The alkane chain vibrations appear at 2852 and 2921 cm^{-1} for PSNPs, with CSNPs showing corresponding peaks at 2850 and 2918 cm^{-1} . The NP alkane vibrations are at lower wavenumbers than the corresponding free acids, indicating confinement and ordered packing on the particle surfaces (Nakamoto, 1997). The ligands and NPs all had a broad OH vibration band between 3200 and 3600 cm^{-1} (not shown).

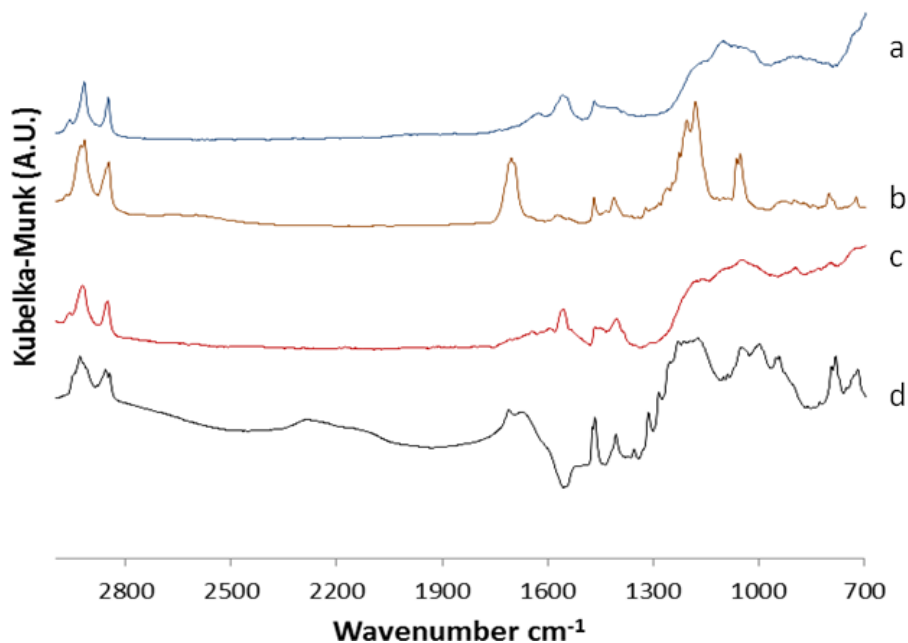


Figure 3.4 DRIFTS spectra of the a) CSNPs b) 11-sulfoundecanoic acid c) NaOH neutralized PSNPs d) 10-phosphono-1-decanesulfonic acid

Preventing magnetite degradation and the loss of acid groups is a primary concern in the design of acid functionalized iron oxide nanoparticles. X-ray diffraction results (Figure 3.5) indicate significant differences in the iron oxide phase compositions of CSNPs and PSNPs. Magnetite and maghemite are present in both CSNPs and PSNPs, with PSNPs showing substantially higher maghemite content. Additionally, the goethite phase of iron oxide is present in the PSNPs but not in the CSNPs or bare particles, as demonstrated by the XRD peaks at 21.18° , 33.20° , 39.93° , 41.16° , 50.65° , 53.16° , 58.98° , and 61.29° , which are marked on Figure 3.5. Carboxylic acids and other ligands are thought to rearrange the surfaces of metal oxide nanoparticles (Laurent et al., 2008; Rajh et al., 2002). This does not necessarily mean a degradation of magnetic properties (Daou et al., 2008; Duan et al., 2008).

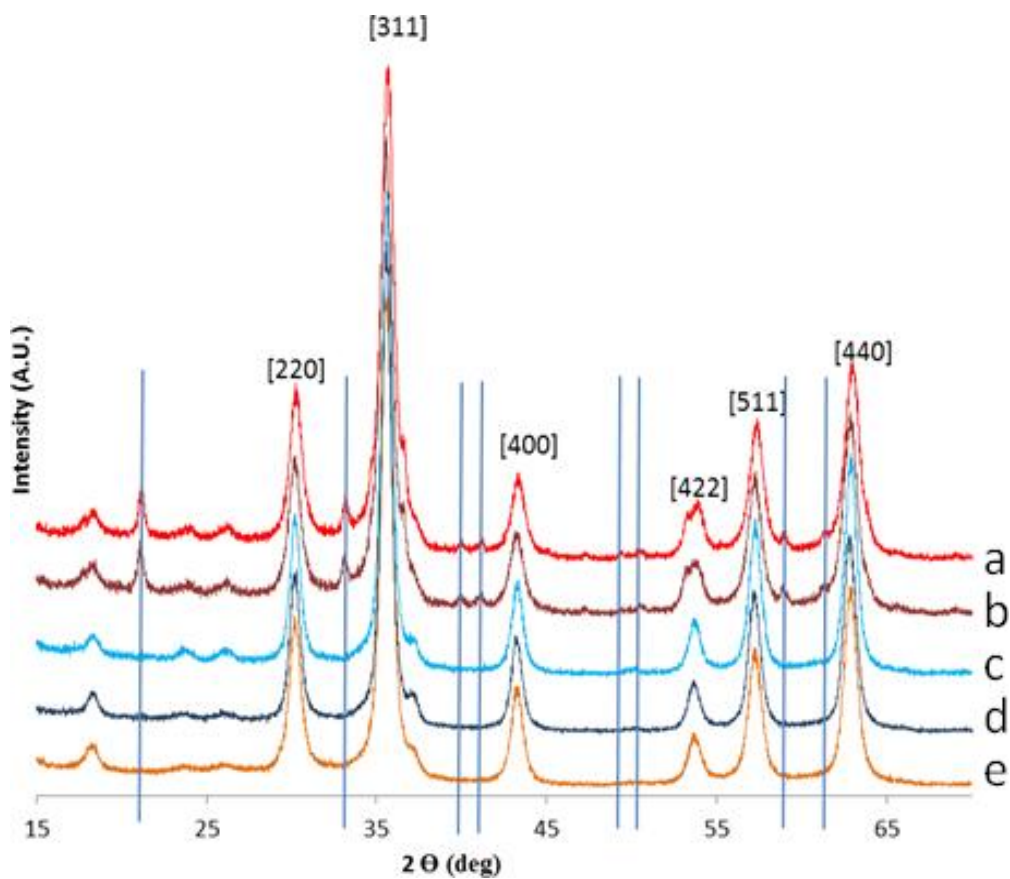


Figure 3.5 XRD for a) PSNPs after 18 hours of starch hydrolysis at 130°C b) PSNPs as synthesized c) CSNPs after 18 hrs starch hydrolysis at 130°C d) CSNPs as synthesized e) bare particles. Lines denote goethite peaks.

The packing density of the ligand layer on the particle surface is important for many reasons. A more tightly packed full monolayer will result in a higher acid site density on the outer surface and a higher ligand loading by weight. Additionally, a tightly packed ligand layer may be more likely to protect the iron oxide core from oxidation, prevent degradation of magnetic properties, and prevent ligand dissociation. We can estimate the packing density of ligands on the particle surfaces by measuring the surface area and ligand loading. The determination of specific surface area in solution is complicated by the decrease of particle surface area that occurs when a sample is dried in preparation for analysis with a Brunauer-Emmett-Teller (BET) device (Sahoo et al., 2005). For this reason, the X-ray diffraction line broadening was used to estimate particle size according to the Scherrer formula.

From X-ray diffraction data, the average diameter of bare magnetite particles is 10.6 nm, which corresponds to a specific surface of 109 m²/g (under the assumption of constant magnetite density). Functionalization with the ligands increased the average particle diameter, possibly due to the rearrangement of atoms on the iron oxide surface, or the preferential loss of smaller acid-functionalized particles during the washing steps. Because the particles are precipitated before ligand addition, size effects are minimized as compared to synthesis schemes in which the ligands are present during particle precipitation (Laurent et al., 2008). XRD gives diameters of 10.9 and 11.5 for the PSNPs and CSNPs, respectively, which correspond to specific surface areas of 107 and 100 m²/g.

Manual measurements of >300 particles from four TEM images of particles functionalized with 11-sulfoundecanoic acid indicate a distribution of diameters as seen in Figure 3.6. Based on this distribution, the specific surface area is 78 m²/g, and the average diameter is 13 nm. The difference between the average of the TEM images and the XRD value may be the result of smaller particles being more difficult to measure in the agglomerates observed by TEM. However, the Scherrer formula gives a minimum size for the particles, so the actual size could be closer to what is seen in the TEM images. Smaller acid-functionalized particles may be preferentially lost during the washing stage, whose bare particle counterparts would be retained in agglomerates during washing.

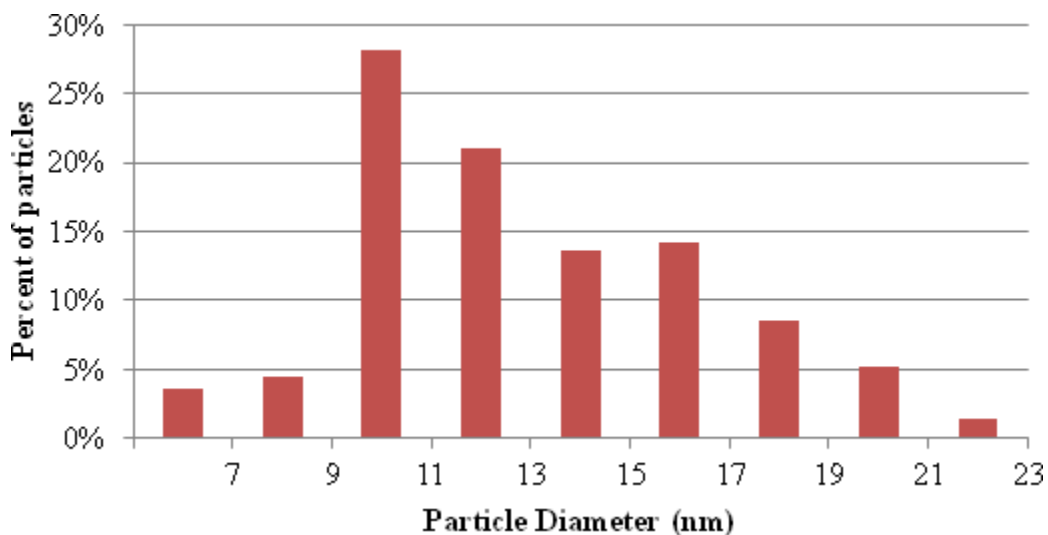


Figure 3.6 Histogram of particle sizes measured from TEM images of CSNPs, giving an average diameter of 13 nm.

Using TEM images to get the diameters of PSNPs is also complicated by agglomeration. As shown below in Figure 3.7, the particles titrated to neutral pH and sonicated for one hour display a sharp difference in agglomeration depending on particle size. Image J software was used to calculate the average diameters from three images of agglomerated particles and three images of individual particles, with particles in agglomerated areas having an average diameter of 12.9 nm and individual particle images showing an average diameter of 5.2 nm. When measured manually by digitally drawing lines within the ImageJ software across more than 300 randomly selected particles from three images, the average diameters were 7.9nm and 3.2nm. The software-calculated values are more consistent with the average diameter calculated from XRD data and the Scherrer formula, which gave the minimum for the average particle diameter as 10.9 nm.

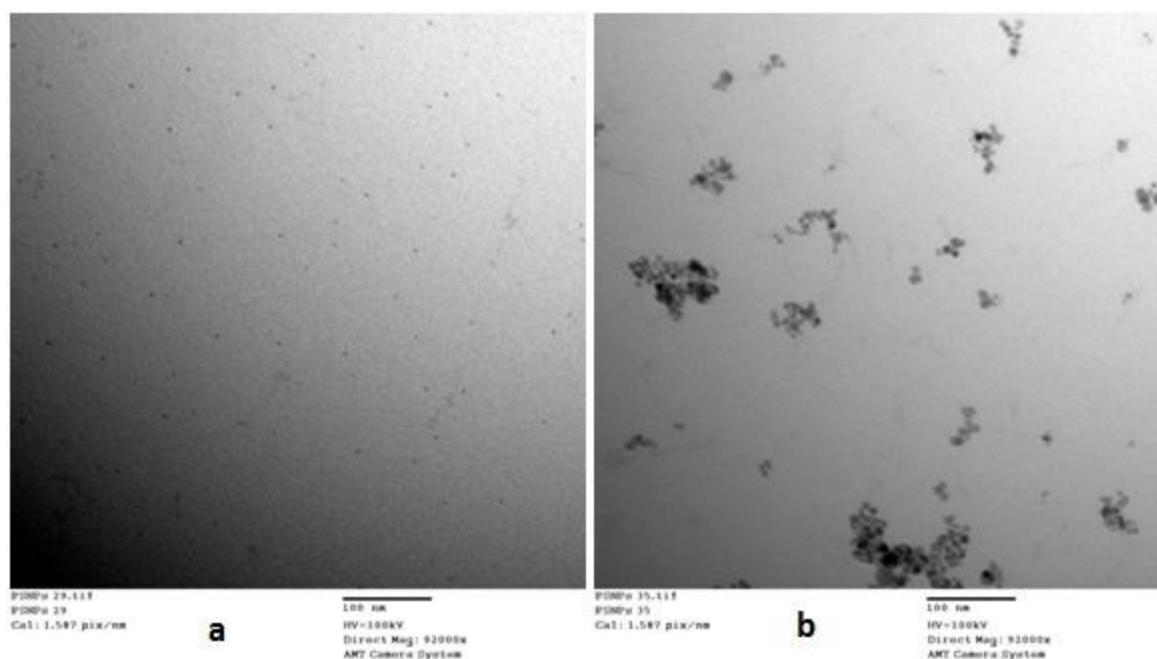


Figure 3.7 PSNPs sonicated for one hour at neutral pH deposit on a TEM grid as both a) non-agglomerated particles with an average diameter of 5.2 nm and b) agglomerates with an average particle diameter of 12.9 nm.

Measuring the sizes of diameters by hand using TEM images is difficult when the particles are agglomerated; it is difficult to tell where one particle ends and the next particle begins. Using software to measure the particles faces the same problem of agglomeration. A method for TEM imaging which would break apart the agglomerates and allow for precise individual measurement of particle diameters would be preferable, but has not been achieved in this work.

Regardless of the exact particle size distribution, the composition of the smallest and largest particles can give some useful information. Table 2 gives calculated, theoretical ligand loadings and ratios of iron to sulfur for nanoparticle diameters 4 to 22nm, with the assumptions of constant magnetite density at 5.18 g/cm^3 , footprint areas of 0.24 nm^2 per phosphonate (Sasmita Mohapatra & Pramanik, 2009) and 0.21 nm^2 per carboxylate (Sahoo et al., 2005), and ignoring ligand effects on particle diameters. At full monolayer coverage, a 4 nm particle has an iron to sulfur ratio around 10:1 for both ligands, while a 22 nm particle has a Fe:S ratio above 50:1 for CSNPs and above 60:1 for PSNPs. Thus, any Fe:S ratio lower than 10 in a supernatant implies

ligand loss, while any Fe:S ratio above 54 for CSNPs and above 62 for PSNPs implies an incomplete monolayer, regardless of the size distribution of particles in the sample.

Table 2 Theoretical ligand loadings and elemental ratios calculated for particles of various diameters.

| Diameter (nm) | Surface area (m ² /g) | g ligand/gcat | mmol ligand/gcat | PSNP Fe:P ratio | PSNP Fe:S ratio | g ligand/gcat | mmol ligand/gcat | CSNP Fe:S ratio |
|---------------|----------------------------------|---------------|------------------|-----------------|-----------------|---------------|------------------|-----------------|
| 4 | 290 | 0.38 | 1.25 | 12 | 11 | 0.38 | 1.42 | 10 |
| 6 | 193 | 0.29 | 0.95 | 17 | 17 | 0.29 | 1.09 | 15 |
| 8 | 145 | 0.23 | 0.77 | 23 | 23 | 0.23 | 0.88 | 20 |
| 10 | 116 | 0.20 | 0.65 | 29 | 28 | 0.20 | 0.74 | 25 |
| 12 | 97 | 0.17 | 0.56 | 35 | 34 | 0.17 | 0.63 | 30 |
| 14 | 83 | 0.15 | 0.49 | 41 | 39 | 0.15 | 0.56 | 34 |
| 16 | 72 | 0.13 | 0.44 | 47 | 45 | 0.13 | 0.50 | 39 |
| 18 | 64 | 0.12 | 0.39 | 52 | 51 | 0.12 | 0.45 | 44 |
| 20 | 58 | 0.11 | 0.36 | 58 | 56 | 0.11 | 0.41 | 49 |
| 22 | 53 | 0.10 | 0.33 | 64 | 62 | 0.10 | 0.37 | 54 |

The 11-sulfoundecanoic acid has a smaller footprint of 0.21 nm² instead of 0.24 nm², and a correspondingly higher mmol H⁺/g at monolayer coverage. These footprints assume close-packed monodentate (Sahoo et al., 2005) or chelating bidentate (Daou et al., 2008) binding for the carboxylate and bridging bidentate (Daou et al., 2008) or tridentate (Sasmita Mohapatra & Pramanik, 2009) binding for the phosphonate. The lower molecular weight offsets that difference and they have the same weight % loading for a given particle diameter. Table 3 gives the calculated properties for the synthesized particles based on the XRD measurements of particle diameters.

Table 3 Calculated properties for CSNPs, PSNPs, and bare particles, based on particle diameters from XRD data.

| Sample | Crystal Size | Surface area (m ² /g) | g ligand/gcat. | mmol ligand/g cat. | g ligand/g cat | mmol ligand/g cat | PSNP Fe:P ratio | PSNP Fe:S ratio | CSNP Fe:S ratio |
|----------------|--------------|----------------------------------|----------------|--------------------|----------------|-------------------|-----------------|-----------------|-----------------|
| bare particles | 10.6 | 109 | 0.19 | 0.62 | 0.19 | 0.70 | 31 | 30 | 26 |
| CSNP | 11.5 | 100 | NA | NA | 0.17 | 0.66 | NA | NA | 28 |
| PSNP | 10.9 | 107 | 0.18 | 0.60 | NA | NA | 32 | 31 | NA |

TGA results for both PSNPs and CSNPs are shown in Figure 3.8, for 10°C/min heating under nitrogen. By 200°C, the CSNPs had lost about 1% of its weight, and the PSNPs had lost about 2%. Some of the weight loss may be due to water. For CSNPs, the total weight loss was 5.6% by weight. If this entire weight loss is ascribed to ligand desorption and decomposition, it corresponds to a sulfur content of 0.69%, or 0.2 mmol/g sulfur in the CSNPs. That is higher than the acid loading of 0.08 mmol H⁺ per gram as determined by titration of the CSNPs. The discrepancy between titration and TGA may indicate that the measured acid loading is reduced by cationic impurities, or that agglomeration hinders solution access to some acid sites. For the PSNPs, the weight loss during TGA was 18.7%, and the titrated acid loading was 0.65 mmol H⁺ per gram. An acid loading of 0.65 mmol H⁺ per gram corresponds to a ligand and sulfur loading of 19.7% and 2.1% by weight, respectively, so the TGA measurement of 18.7% is roughly in agreement with the titration. Impurities and agglomeration might also affect the measurement of PSNP acid sites, but be counteracted to some extent by incomplete removal of the ligand layer. During TGA of functionalized iron oxide nanoparticles, it is thought that some carbon remains on the particle surface due to incomplete decomposition of the organic ligands, and the formation of graphitic species (Roonasi & Holmgren, 2009). Incomplete decomposition may be more significant for the higher ligand loading of the PSNPs.

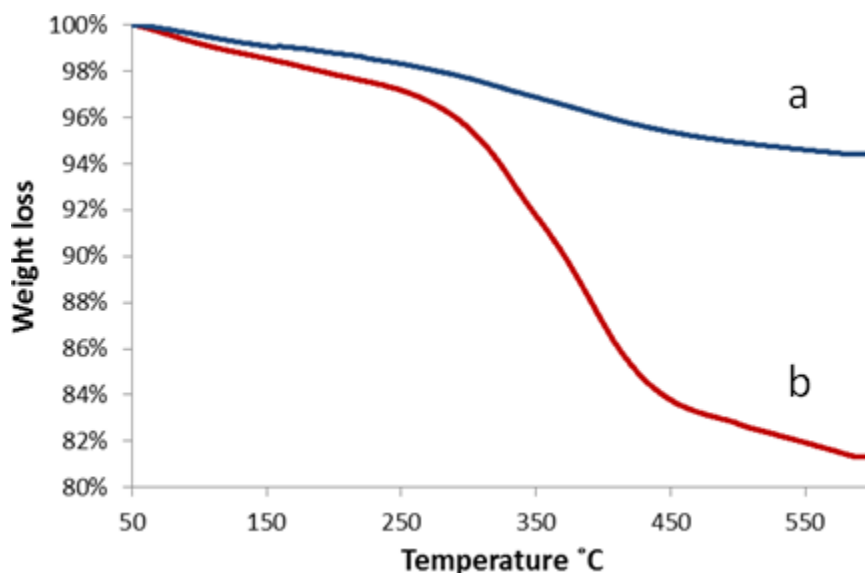


Figure 3.8 TGA graph of catalyst weight % vs. the temperature (°C). The total weight loss is a) 5.6% for the CSNPs and b) 18.7% for the PSNPs

The Scherrer equation calculates the PSNP diameter as 10.9 nm from the XRD data, which corresponds to a specific surface area of 107 m²/g for a constant magnetite density of 5.18g/cm³. For a ligand footprint of 0.24nm², there is an 18% weight loading of 10-phosphono-1-decanesulfonic acid, and 0.60 mmol H⁺/gram. The measured TGA ligand loading of 18.7% and titration loading of 0.65 mmol H⁺/ gram are close to what is expected, suggesting a complete monolayer with a ligand footprint of 0.24 nm².

For CSNPs, the XRD indicates an average particle size of 11.5 nm, which corresponds to a specific surface area of 100 m²/g. The slightly smaller carboxylate footprint of 0.21 nm² and molecular weight of 266.4 g/mol for 11-sulfoundecanoic acid correspond to a 17% ligand weight loading for monolayer coverage, with a sulfonic acid loading of 0.66 mmol H⁺/gram. TGA and titration indicate that the coverage is significantly less than monolayer for the CSNPs, with TGA putting the ligand loading at 5.6% and the titration indicating only 0.08 mmol H⁺/gram. If the lower than expected titration measurement is due to restriction of acid sites within agglomerates, then the TGA value may be a better indicator of the ligand packing density. According to this analysis, the CSNPs have approximately 1/3 of a monolayer. However, this packing density is likely an average over significantly different packing densities for different particle sizes, as indicated by other work with oleic acid and magnetite nanoparticles with monodisperse diameters (L. Zhang et al., 2006).

3.8 Sucrose and Starch Hydrolysis

Reaction conditions to catalyze the hydrolysis of sucrose at 80°C and starch at 130°C were adopted from the work of Dhepe et al. (2005) in order to enable direct comparison with solid acids which have been previously demonstrated. For sucrose hydrolysis, conversion was calculated according to equation 3, and turnover frequency was calculated with equation 4. For starch hydrolysis, conversion was calculated according to equation 5, and turnover frequency was calculated with equation 6.

Equation 3 Sucrose conversion = $([G]+[F])/([G]+[F]+1.05[S])$

where [G], [F], and [S] are the concentrations of glucose, fructose, and sucrose, respectively, in the supernatant after reaction. The factor of 1.05 accounts for the additional weight of the water molecule gained during the hydrolysis reaction.

$$\text{Equation 4 TOF} = [\text{mol glucose (mol H}^+\text{)}^{-1} \text{ hr}^{-1}]$$

which gives the moles of glucose formed per acid site of the catalyst per hour, averaged over the course of the 6-hour sucrose hydrolysis reaction cycle.

$$\text{Equation 5 Starch conversion} = [G]/1.05[H]$$

where [G] is the glucose concentration after reaction, [H] is the initial starch concentration, and the factor of 1.05 accounts for change in molecular weight during hydrolysis of the polymer into monomers

$$\text{Equation 6 TOF} = [\text{mol glucose (mol H}^+\text{)}^{-1} \text{ hr}^{-1}]$$

which gives the moles of glucose formed per acid site of the catalyst per hour, averaged over the course of the 6-hour sucrose hydrolysis reaction cycle.

Sucrose hydrolysis was conducted by 80 °C for 6 hours in a sealed vial with magnetic stirring, using 0.05g of catalyst and 0.1g of sucrose in 5g of water. Reaction temperature was controlled using an oil bath held at constant temperature, with reactor temperature periodically checked with a temperature probe. After the completion of each run, the catalyst was separated either by supermagnet or by centrifugation. Fresh sucrose and 5g of water were placed in the reaction vessel, which was returned to the oil bath for the next round of reaction. For estimation of the experimental variability, five runs with fresh Amberlyst-15 were conducted and found to give a standard deviation of 6% for sucrose conversion.

To test the reproducibility of the trend seen in CSNP activity, three runs were conducted on three different CSNP samples. Control runs with no catalyst present showed no conversion. Catalytic activity was measured in terms of sucrose conversion to the two hydrolysis products glucose and fructose. The mass balance indicated that fructose formed by-products which are less than 3% of the total mass.

For starch hydrolysis, 0.002g (dry wt.) of PSNPs, 0.017g (dry wt.) of CSNPs, or 0.0006g Amberlyst-15 were added with 0.09g starch and 5g of water so as to yield an acid site:starch:water mole ratio of 1:200: 100,000 for Amberlyst-15 and 1:400:200,000 for the CSNPs and PSNPs. In a sealed glass tube with magnetic stirring at 300 rpm, the mixtures were placed in an oil bath at 130°C for 24 hours. CSNPs and PSNPs were both separated by centrifugation at 10,000 rpm for 1 hour at 4°C. The centrifuged catalyst was combined with 5g of water and 0.09g of starch and returned to the reaction vessel for the next run. To estimate the variability of the experimental setup, 3 runs with fresh Amberlyst-15 were run, and a sucrose conversion standard deviation of 3.7% was found. Control runs with no catalyst present showed no conversion. Catalytic activity is measured in terms of glucose turnover frequency per acid site. Oligomers were not measured.

Control runs were conducted for sucrose hydrolysis in the absence of catalyst, in the presence of only the ligands, and in the presence of only the bare iron oxide nanoparticles. The averaged conversions from two trials are shown in Table 4. Ligand weights were selected to correspond with the loading on 0.05g of catalyst particles, using the ligand loadings from TGA analysis.

Table 4 Hydrolysis reactions for 0.1g sucrose and 5g water at 80°C for 6 hours, averaged from two runs with no catalyst, 0.05g bare Fe₃O₄ nanoparticles, 0.0025g 11-sulfoundecanoic acid, and 0.001g 10-phosphono-1-decanesulfonic acid.

| | |
|-------------------------------------|------|
| no catalyst | 0% |
| bare Fe ₃ O ₄ | 37% |
| 11-sulfoundecanoic acid | 24% |
| 10-phosphono-1-decanesulfonic acid | 100% |

The controls with no catalyst showed no conversion, as expected. 11-sulfoundecanoic acid conversion may have been lowered by impurities remaining after the purification process, while 10-phosphono-1-decanesulfonic acid's complete conversion was probably due to the combination of strongly acidic phosphonic and sulfonic acids. Surprisingly, two runs with bare particles showed an average 37% conversion. To our knowledge, iron oxide catalysis of carbohydrates has not been previously published in the literature. We are unsure as to whether

the iron oxide is truly catalyzing the reaction. Impurities left over from the synthesis process may be responsible for the catalytic activity. The activity of bare particles complicates the analysis of recycle data, and gives the possibility that turnover frequencies for acid groups are artificially inflated by catalytic activity from iron oxide catalytic sites.

The conversion of sucrose for three different CSNP samples over multiple consecutive runs is shown in Figure 3.9. The CSNP catalytic activity increases through the first 4 runs, using centrifugation for separation of particles between runs. After the 4th cycle, the catalyst was refrigerated and stored for one week before being used again in recycle reactions 5-9, with magnetic particle separation. Sucrose conversion for trials 6-9 is relatively constant at ~60%. As seen in Figure 3.9, the increasing activity over the first four recycles was noted for three different CSNP samples, providing strong evidence that this was a real trend.

The much higher acid loading of Amberlyst-15 results in a higher conversion for sucrose hydrolysis for equal catalyst weight. However, the CSNPs and PSNPs have a higher turnover frequency per acid site, possibly due to the location of acid groups on the outer surface of the material. The turnover frequency (TOF) for CSNPs (9th run), PSNPs (17th run) and Amberlyst-15 are 7.1, 0.64, and 0.20 mol sucrose converted/mol H⁺/hour, respectively, based on initial acid loadings. The TOF for CSNPS would be lower if the CSNP acid loading were calculated from the TGA data instead of the titration data. The higher TOF of acid sites is apparent in the starch hydrolysis, which compares equal numbers of acid sites instead of equal catalyst weights.

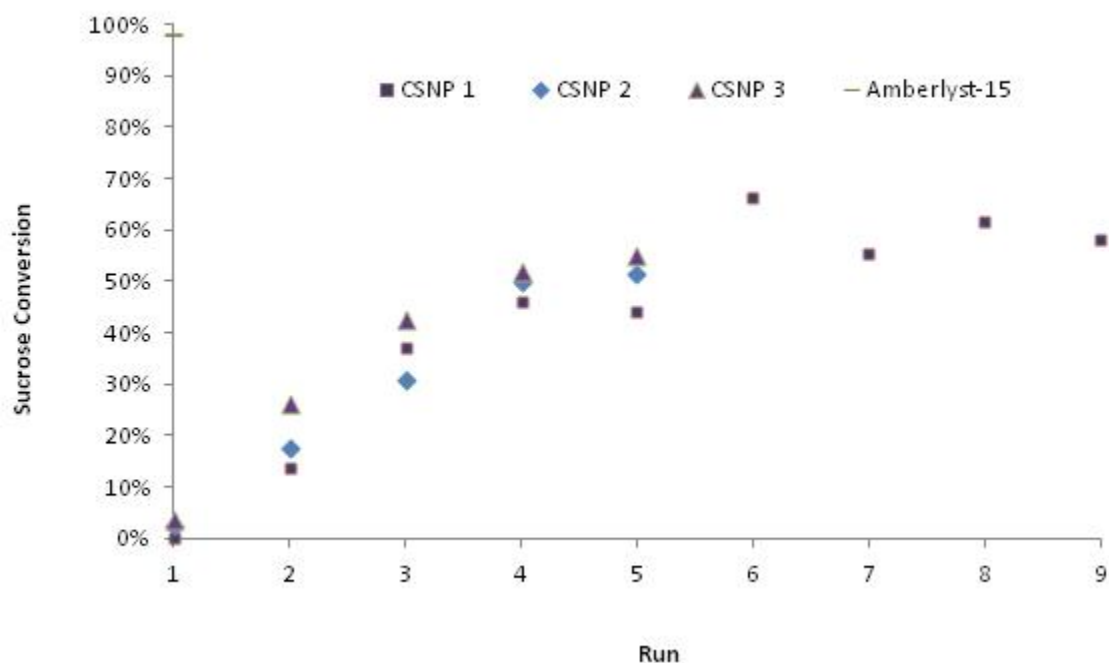


Figure 3.9 Sucrose hydrolysis at 80°C using 0.05g catalyst, 0.1g sucrose, and 5g water.

An increase in catalytic activity during recycle runs is unusual for solid acids, and may be related to a decreased agglomeration. In aqueous solutions of functionalized iron oxide nanoparticles, agglomeration often decreases at higher temperatures (Kikura et al., 2004). The de-agglomeration of CSNPs has been observed in TEM images, as shown in Figure 3.10. On the left, the agglomeration of primary particles leaves only a single non-agglomerated particle to be seen in the TEM image. In the image on the right, 6 hours of sucrose hydrolysis at 80°C has caused the agglomeration to decrease significantly.

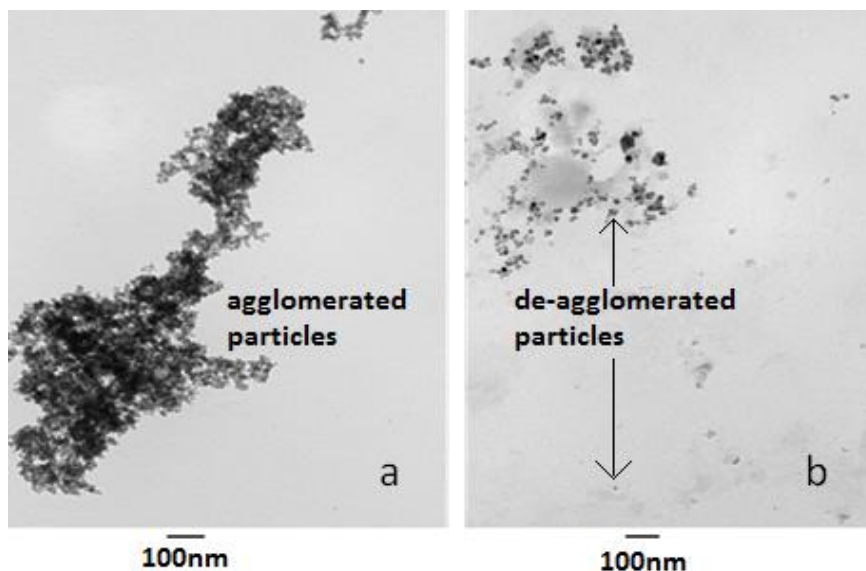


Figure 3.10 TEM images from CSNPs deposited a) at room temperature in pure water b) from an aqueous 80°C sucrose solution after a 6 hour reaction.

The CSNP de-agglomeration during sucrose reactions was also measured with DLS, by adding drops of hot reaction solution to a heated cell containing 70°C sucrose solution. These conditions were chosen to minimize agglomerate changes during the DLS measurement of the reaction mixture. Table 5 shows the DLS results. DLS measurements of the CSNPs taken at the beginning and end of a 6-hour sucrose reaction indicated that the initial effective agglomerate size of 3000-4000 nm was reduced to less than 1000 nm by the end of a reaction cycle. The necessary dilution for DLS measurement may have caused some de-agglomeration.

Another possible explanation for the increase in activity is an increased iron oxide surface exposure as ligands rearrange and/or dissociate from the iron oxide core. As indicated in Table 5, ligand loss into the supernatant is less than 1 ppm, with ICP giving sulfur measurements less than 1 ppm for the supernatants of the first four runs.

Table 5 ICP measurements of iron and sulfur in the supernatants of the first four sucrose hydrolysis runs with CSNPs.

| Supernatant sample | Run | Fe ppm | S ppm | Fe:S ratio |
|--------------------|-----|--------|-------|------------|
| CSNP1 | 1 | 6 | 0.6 | 9 |
| CSNP2 | 2 | 8 | 0.6 | 14 |
| CSNP3 | 3 | 21 | 0.9 | 24 |
| CSNP4 | 4 | 32 | 0.4 | 82 |

The sulfur losses seen in the first four runs are very low. The ICP-OES machine gives atomic concentrations of about 0.2 ppm for blank solutions. The iron to sulfur ratios for these runs are around what would be expected for the loss of small particles with monolayer coverage, and therefore do not necessarily imply ligand dissociation from the iron oxide cores of the CSNPs. Although it is not possible to distinguish between the catalytic effects of the particle surface and the acid ligands, the ~60% conversion seen for the last four runs compares well against the 90% conversion demonstrated for identical reaction conditions in previous work by Dhepe et al. for their acid-functionalized mesoporous silicas (Dhepe et al., 2005).

The differences between properties of different sized particles complicate the analysis of what is happening to the CSNPs during reaction. For example, are the functionalized nanoparticles truly the active catalysts or is the dissociated ligand and resulting bare particle surface playing an important role? The ICP data suggests that there is little ligand loss during reactions. The presence of iron in the supernatant could result from the presence of bare particles or iron atoms dissolved from the magnetite cores into the supernatant, or it could indicate the loss of entire functionalized nanoparticles. The increasing iron content of subsequent reaction cycles is consistent with an increasing loss of individual functionalized particles to the supernatant, which might be expected along with the decrease in agglomeration and increase in catalytic activity. The consistent black color of the CSNPs throughout the recycle runs is indicative of magnetite core stability and that observation is consistent with the XRD data which indicates stability of the magnetite crystal structure after 18 hours of starch reaction at 130°C.

The PSNP catalytic activity for sucrose hydrolysis is shown in Figure 3.11 for 17 consecutive 6-hour runs. Catalyst separation was achieved by using an external magnetic field in

runs 1-13 and by centrifugation in runs 14-17. As seen in Figure 3.11, conversion is between 40 and 50% for the first four runs, but then shows a decrease to less than 20% by the 13th run. This decrease is likely due to the loss of magnetic particles in the recycling process. PSNPs are quite stable in solution, so a certain amount is not able to be extracted even by the high powered magnet. Figure 3.12 is a photograph of the supernatants following reaction and removal of PSNPs with the magnet. The darker colors observed are an indication that some PSNPs remain in the supernatant.

To understand whether the loss in activity noted over 13 runs was entirely due to the loss of PSNP particles, the supernatants collected in the first 13 runs were centrifuged to recover more of the suspended catalyst for reuse. The centrifugally recovered catalyst was combined with the catalyst that had been magnetically recovered. The recombined catalyst was then used in further reactions. As seen in Figure 3.11, PSNP conversion returned to over 40% for runs 15-17, indicating that the catalyst had not been deactivated. As with the CSNPs, the activity of iron oxide for this reaction reduces the usefulness of conversion data to determine the activity of acid ligands the stability of their attachments to the iron oxide cores.

The trend for increased activity on subsequent runs seen in the CSNP reaction data may have been countered by the loss of PSNP particles due to incomplete recovery by magnetic separation. This might be an indication that the magnetic character of the magnetite core is damaged by the attachment of the phosphonate ligands. This is supported by the XRD data that shows peaks associated with the presence of the iron phase goethite (α -FeOOH) in addition to substantially increased maghemite (Fe_2O_3), after phosphonate ligand attachment. For runs 15-17, centrifugation was used to recycle the PSNPs. A conversion above 40% for these recycle runs indicates that centrifugation is superior to magnetic separation when recycling the PSNPs.

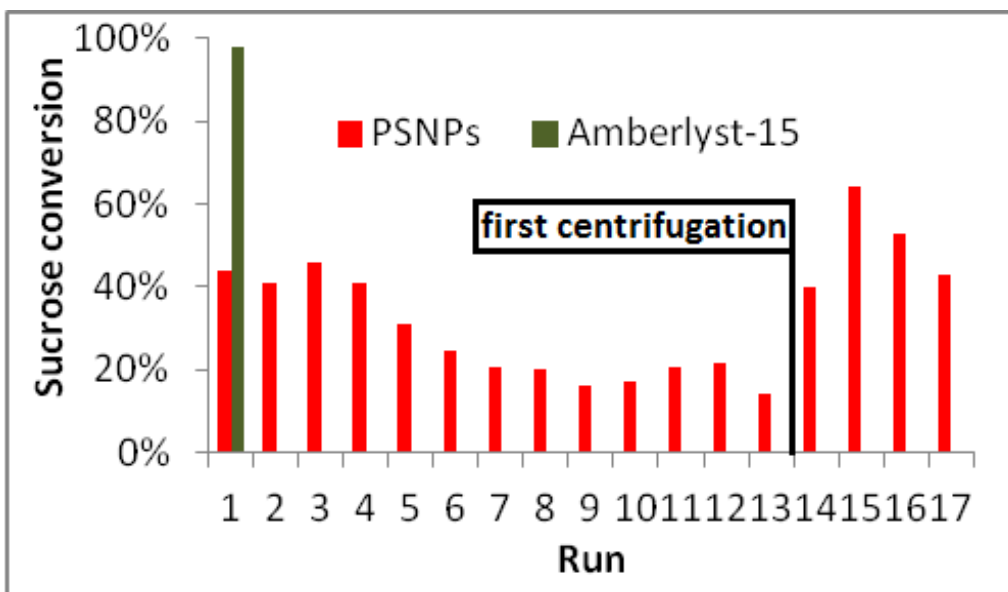


Figure 3.11 Sucrose hydrolysis at 80°C using 0.05g catalyst, 0.1g sucrose, and 5g water.



Figure 3.12 6-hour sucrose reaction supernatants contain PSNPs which remained suspended in the presence of the external magnetic field.

The PSNPs are not easily separated from solution. Centrifugation is more effective, but supernatant measurements by ICP indicate the presence of iron which may be from residual particles. The tendency of some particles to remain in solution may be due to a combination of factors such as increased hydrophilic character from the increased number of sulfonic acid groups, increased hydrophilic character due to the more highly packed and less exposed lipid layer, decreased agglomerate sizes resulting in smaller effective magnetic force per particle, and possibly decreased particle magnetic strength. These factors may also result in preferential loss of smaller nanoparticles.

ICP was used to gain some information about the atomic composition of the supernatants after catalyst removal. As seen in Table 6, these data indicate a ratio of iron to phosphorus that is around 2:1 for the combined supernatants of runs 1-13, and around 4:1 for the individual supernatants of runs 14-16. The final reaction solution, containing the recycled catalyst, required

dilution to 10% concentration before ICP analysis, and the 2 ppm difference between phosphorus and sulfur is magnified when the results are multiplied to get the undiluted solution concentration.

Table 6 ICP data for the inseparable catalyst remaining in solution after 6 hour sucrose runs.

| sample | Run | Fe (ppm) | P (ppm) | S (ppm) | Fe:S ratio |
|-----------------------|----------|----------|---------|---------|------------|
| P1-13 | 1 to 13 | 20 | 9 | 9 | 2 |
| P14 | 14 | 19 | 5 | 5 | 4 |
| P15 | 15 | 47 | 10 | 12 | 4 |
| P16 | 16 | 26 | 6 | 8 | 3 |
| P17 10% dilution | Catalyst | 355 | 8 | 6 | 59 |
| P17 recycled catalyst | Catalyst | 3550 | 80 | 60 | 59 |

The incomplete separation of particles from solution, combined with the correlation between ligand loading and particle size, complicates the interpretation of ICP data. The presence of iron and sulfur in the supernatants of the runs may indicate the loss of entire functionalized particles to the supernatant, with smaller diameter particles being lost more than larger particles. However, the ratios of iron to sulfur and phosphorus seen in Table 6 for reactions 1-13 and 14-16 are lower than the ratios for the monolayer of a 2nm particle, and therefore confirm some presence of free ligands in the centrifuged supernatant solutions. If the PSNPs had a monolayer initially, and then lost ligands over the course of the 16 sucrose hydrolysis reactions, the Fe:S and Fe:P ratios seen for the centrifugally recovered particles used in reaction 17 should be lower than what is expected for a monolayer. However, the preferential loss of small particles would also decrease the Fe:S ratio, so a decrease may be a combination of both phenomena.

The composition of the catalyst in the original sucrose reaction solution was not measured by ICP. However, by using the titrated acid loading of 0.65 mmol H⁺/g to estimate a ligand loading of 20% by weight, the initial catalyst loading shown can be estimated, as shown in Table 7. The ICP data in Table 6 can be used to calculate the amount of ligands lost during the 16 sucrose hydrolysis reactions. Comparing the sulfur and phosphorus lost in the reaction supernatants to the estimate of the initial catalyst composition in the reaction solution can give some understanding of the ligand-core stability for the PSNPs.

Table 7 Elemental compositions as estimated for the initial catalyst composition, and measured by ICP for sucrose hydrolysis losses and the final reaction solution.

| | Estimated Initial | ICP: losses in 16 runs | Expected remaining | ICP data: catalyst run 17 |
|----------------|-------------------|------------------------|--------------------|---------------------------|
| ppm phosphorus | 205 | 139 | 66 | 83 |
| ppm sulfur | 212 | 142 | 70 | 61 |
| ppm iron | 5789 | 353 | 5436 | 3553 |
| Fe:S ratio | 27 | 2.5 | 77 | 59 |
| Fe:P ratio | 28 | 2.5 | 83 | 43 |

The low Fe:S ratio of 2.5 seen in the centrifuged supernatants from the first 16 runs indicates that some sulfur is due the presence of ligands that have dissociated from the particle surfaces. This is supported by ICP measurements of the final reaction solution which indicate Fe:S and Fe:P ratios higher than what is estimated for the initial reaction solution. However, the uncertainty in the ICP measurements is significant, and the Fe:P ratio of 43 measured from the recycled catalyst is not far from the expected initial ratio of 32.

The final reaction solution was dried to increase agglomeration and reduce particle loss during the 10 repeat washings used to remove excess sugars. However, some smaller particles were likely lost during the 10 washings. The washed catalyst was then dried again, and analyzed by XPS and TGA analysis. XPS surveys of the PSNPs before reactions and after recycling are shown in Figure 3.13.

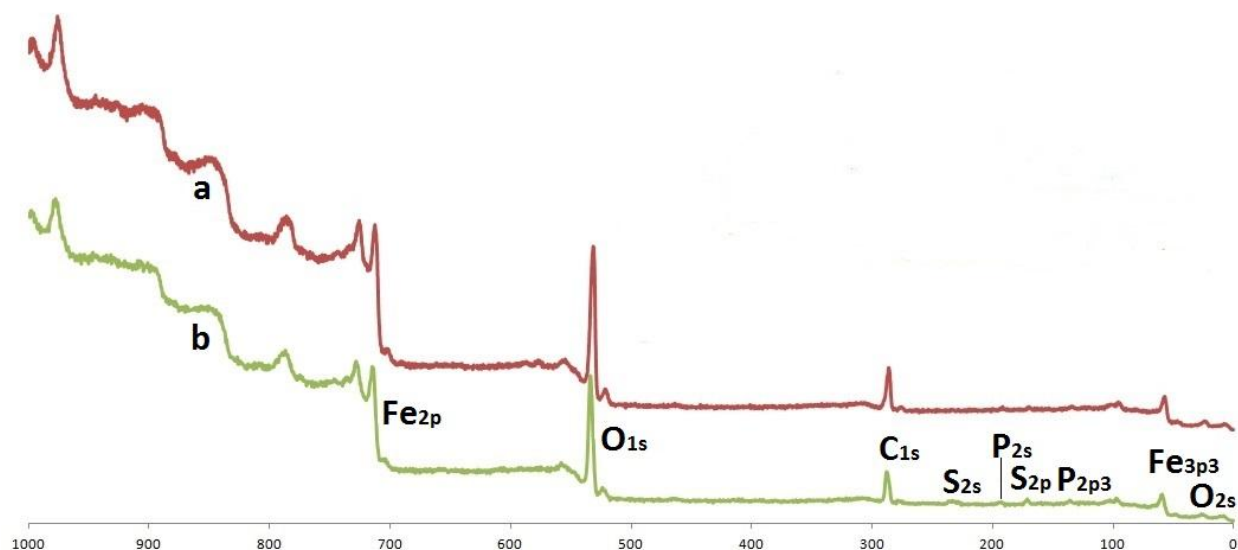


Figure 3.13 XPS survey of a) PSNPs before reaction b) PSNPs after 17 sucrose reactions and washing to remove sugars

Table 8 XPS survey compositions for PSNPs before and after 17 sucrose reactions.

| | Fe _{2p} | O _{1s} | C _{1s} | S _{2p} | P _{2p} |
|---|------------------|-----------------|-----------------|-----------------|-----------------|
| PSNPs | 9.9% | 50.8% | 32.5% | 4.0% | 2.8% |
| PSNPs after 17 sucrose reactions, extensive washing | 10.5% | 51.4% | 34.5% | 1.9% | 1.7% |

In Table 8, the sulfur and phosphorus atomic concentrations decrease significantly in the XPS survey of the PSNPs after 17 sucrose reactions, without a corresponding drop in iron content that might indicate the presence of sugars. The TGA weight loss from 120°C to 600°C is reduced from 18.7% before reaction to 8% after the reactions, further confirming the decrease in organic ligand content. The XPS and TGA measurements, like the ICP data, are unable to differentiate between the sulfur that is lost from 10-phosphono-1-decanesulfonic acid ligands dissociating into solution during the sucrose reaction cycles and the sulfur that is lost in the form of functionalized particles. Both sources of ligand loss would contribute to a lower ligand loading and sulfur elemental composition measured for the recycled catalyst.

For comparing the activity of PSNPs to CSNPs and Amberlyst-15, the starch hydrolysis data is more useful since centrifugation was used to maximize catalyst recovery after each

reaction. Acid site turnover frequency (moles of glucose formed per mole of acid per hour) for PSNPs, CSNPs, and Amberlyst-15 is shown in Figure 3.14. The PSNPs show the highest activity for starch hydrolysis, surpassing the CSNPs and Amberlyst-15. The CSNP activity is likely overestimated as a result of using the titration data, instead of the TGA data, to determine the amount of CSNP used in the reactions. The increased ligand loading achieved using the phosphonic acid attachment apparently also results in an outer surface whose acid sites are individually more active for starch hydrolysis. Unfortunately, there is a trade-off between the benefits and downsides of a more highly hydrophilic outer surface. Even with centrifugation, the PSNPs leave the supernatant visibly darkened with the presence of particles.

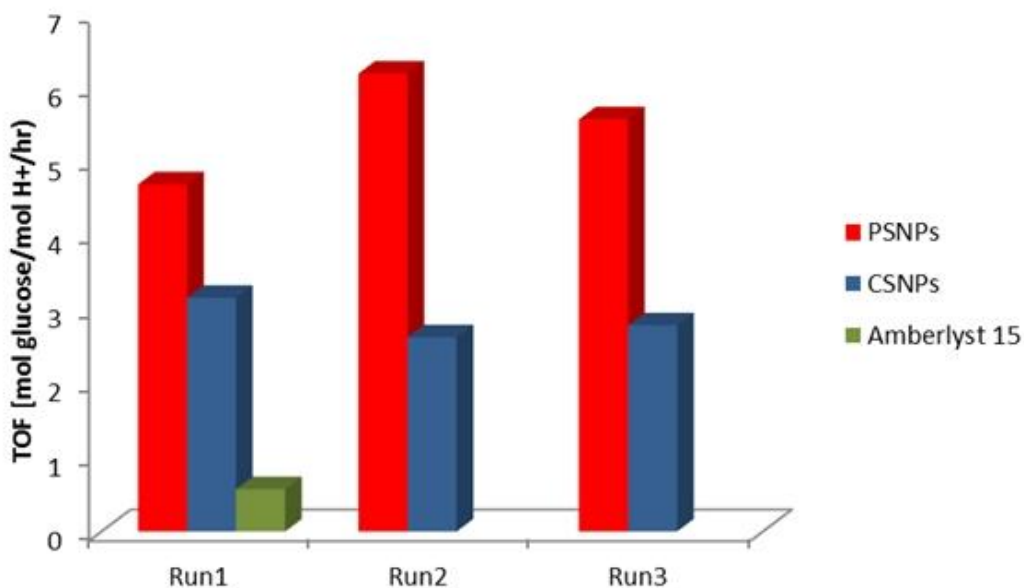


Figure 3.14 TOF [mol glucose (mol H⁺)⁻¹ hr⁻¹] for three runs of 24 hour starch hydrolysis at 130°C

Dhepe et al. demonstrated that sulfonic acid-functionalized mesoporous silicas gave a glucose yield of 68% for starch hydrolysis at 24 hours and 130°C with an acid site:starch:water ratio of 1:200:100,000 (Dhepe et al., 2005). Our reactions with nanoparticles used half of that concentration of acid sites, at an acid site:starch:water ratio of 1:400:100,000. With half the acid loading, PSNPs and CSNPs gave glucose yields averaging 32% and 18% over three runs,

respectively. The CSNP activity would likely be lower if the TGA data were used instead of the titration data to calculate the ligand loading.

For both the CSNPs and PSNPs, the activity seen is an average over particles of significantly different radii and surface curvature. Beyond the immediate geometrical trends, the smaller particles are likely to behave differently from larger ones. For example, smaller iron oxide nanoparticles have been seen to form more tightly packed monolayers than larger particles (L. Zhang et al., 2006). This may compound the effect of increased surface area and further increase the weight loading of ligand on smaller particles. However, since phosphonic acids bind more strongly than carboxylic acids to magnetite, the monolayer density as a function of particle size may be less pronounced in PSNPs than in CSNPs. Another interesting effect of the nanoparticle curvature is the tendency to push acid groups closer together at larger particle sizes (D. Wang et al., 2011). It is unclear whether this effect increases acid site activity (Mbaraka & Shanks, 2006) or decreases it (D. Wang et al., 2011).

3.9 Conclusions

11-sulfoundecanoic acid and 10-phosphono-1-decanesulfonic acid both create quasi-monolayers on the iron oxide particles with sulfonic acid groups available for catalysis. The binding of carboxylate groups to magnetite can be confirmed by the absence of the symmetric stretch of COOH in the DRIFTS spectra. The phosphonic ligand gave a packing density more than three times higher than the carboxylic ligand on the polydisperse iron oxide particles, possibly a full monolayer. The more tightly packed monolayer of the phosphonate ligand corresponded to a higher sulfonic acid loading by weight, reduced agglomeration of particles, and a greater tendency to remain suspended in solution in the presence of an external magnetic field.

Polydisperse iron oxide particles functionalized with 10-phosphono-1-decanesulfonic acid showed an increased ratio of iron to sulfur after 17 sucrose hydrolysis reactions, as measured by ICP analysis of the aqueous solution and XPS analysis of the washed and dried particles. TGA confirmed a final ligand loading around half of what was measured initially. These measurements cannot differentiate between the loss of sulfur as dissociated ligands and

the loss of sulfur in the form of smaller particles with ligand loadings higher than the average loading for the polydisperse sample. However, the ratio of iron to sulfur measured by ICP is lower than what is expected for small particles, and thus indicates the presence of some dissociated ligands in the supernatant solutions. Although the higher ligand loading on the PSNPs is attributable to the higher bonding strength between magnetite and phosphonates, incomplete washing cannot be ruled out. Unattached ligands remaining after washing may have contributed to the presence of free ligands in the supernatant as measured by ICP.

CSNPs and PSNPs both show significant catalysis of sucrose and starch hydrolysis. Dhepe et al. reported a 90% conversion over 6 hours of sucrose hydrolysis for sulfonic acid-functionalized mesoporous silicas, compared to our CSNPs averaging 60% conversion for the last four recycle runs of a 9 run reaction series. The PSNP activity for sucrose hydrolysis was less certain due to the incomplete catalyst recovery. CSNPs have been shown to possess an interesting trend of increasing catalytic activity through initial sucrose hydrolysis reactions, likely because of deagglomeration of particles at the elevated reaction temperatures. The same trend for increased activity over initial recycle runs might have been demonstrated in the PSNPs if not for the incomplete catalyst recovery by magnetic field in the initial runs. The presence of particles in the supernatant correlates with ICP data showing the presence of iron and sulfur in the post-centrifugation supernatants of both catalysts and indicates that smaller particles are lost at a greater rate than larger particles. The downside of decreased catalytic recovery is a significant one. If particles with larger diameters and/or less tightly packed monolayers are more easily recovered, a lower acid loading by weight may be a desirable trade-off.

Chapter 4 - Amino Acids on Magnetite

4.1 Amino Acid Ligands

After characterization of the 11-sulfoundecanoic acid functionalized nanoparticles and acid-catalyzed hydrolysis of starch and sucrose, we wanted to study the effect of chain length on attachment and stabilization of the sulfonic/carboxylic di-acid ligands on the nanoparticle surface. In the case of carboxylic acids, there has been success reported regarding the use of short chain molecules for the stabilization of some magnetic nanoparticles in organic solutions (Avdeev et al., 2007). The length of the hydrocarbon chain has many important possible effects for the behavior of the catalyst. A thicker hydrophobic layer may be a better buffer by which to keep outer molecules from contacting the particle surface and interfering with ligand-particle bonds. However, if the packing density of the longer chain ligands is lower, the hydrophobic region will not necessarily be thicker than the layer created by shorter ligands. Longer ligands may not necessarily protect the ligand-particle bonds better than shorter ligands. In addition to a potential reduction in ligand diffusion, the longer chains may create a more hydrophobic outer surface with a larger distance between hydrophilic tail group moieties, affecting the interactions between the solvent, reagents, and active acid sites.

A direct comparison would involve the use of carboxylic-sulfonic acids with shorter chain lengths than the 11-sulfoundecanoic acid. The literature did not provide a route for facile synthesis of 6-sulfohexanoic acid or 3-sulfopropionic acid. Cui et al's optimized synthesis of 11-sulfoundecanoic acid indicated that both the reagent ratio (of 11-bromoundecanoic acid ligand to sodium sulfite salt) and the heating procedure required optimization in order to achieve high product purity (Cui et al., 2006). For such optimization, synthesis of sulfonic-carboxylic acids would require time-consuming purification and characterization steps. Instead of synthesizing sulfonic-carboxylic acids of various chain lengths from their brominated analogues, a substitute ligand was desired which would provide similar molecular characteristics.

To study the effects of ligand chain length, without developing synthesis schemes to obtain sulfonic-carboxylic acids from the 6-bromohexanoic acid and 3-bromopropionic acid precursors, a similar ligand was sought which could be purchased at high purity from a chemical

distributor. The most important aspects of a potential ligand were considered to be a carboxylic acid head group and an ionic tail group which would not bind to the magnetite surface. 11-aminoundecanoic acid, 6-aminohexanoic acid, and 3-aminocaproic acid ligands were selected. It was anticipated that a significant benefit of this choice would be the creation of amine-decorated, base-functionalized iron oxide nanoparticles.

4.2 Literature Discussion of Amine Bonding

Because the amino acids are zwitterionic, they maintain a positive charge on the amine and negative charge on the carboxylate throughout a wide pH range. At a low pH, the amphoteric iron oxide surface's positive surface charge has an electrostatic repulsion to the positively charged amine ligand tail, as shown in Figure 4.1.

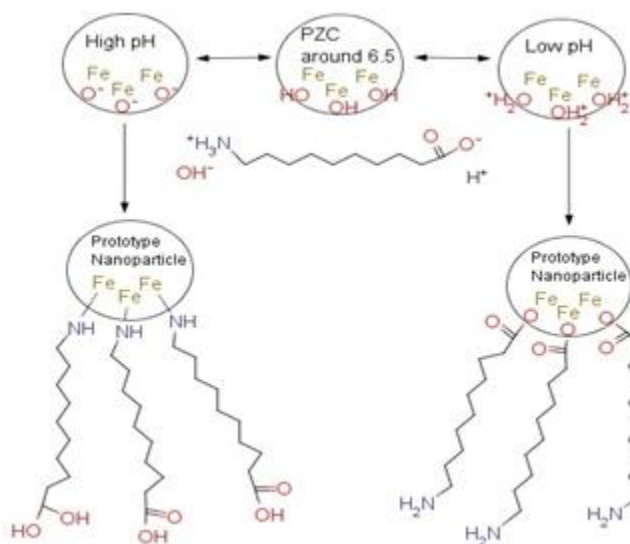


Figure 4.1 The amphoteric iron oxide nanoparticle surface has electrostatic attractions to oppositely charged moieties (Cornell and Schwertmann).

In addition to electrostatic consideration, it is widely stated in the literature that carboxylic acids are among the specific binding moieties, which form bonds to magnetite even in electrostatically unfavorable pH regions. Amines are non-specific binding moieties and should only form electrostatic or hydrogen bonds to the magnetite surface (Cornell & Schwertmann, 2003). According to most literature sources, the bonding between the ligand and magnetite surface is expected to be exclusively through carboxylic acid moieties, although some authors

report that positively charged amine groups adsorb onto iron oxide surfaces at high pH (Siddiqui, Unwin, Xu, & Kresta, 2009).

Cornell and Schwertmann's often cited "The Iron Oxides: Structure, Properties, Reactions, Occurrences, and Uses" covers magnetite chemistry extensively, including specific and non-specific binding ions (Cornell & Schwertmann, 2003). According to Cornell and Schwertmann, specific binding ions can form inner sphere complexes with magnetite at pH values unfavorable to electrostatic interaction. FeOH_2^+ , FeOH^0 , and FeO^- surface species exist in equilibrium at the point of zero surface charge (p_{pzc}) and when the overall surface charge is positive or negative. Because magnetite has a higher concentration of FeOH_2^+ on its surface at a lower pH, anions will have a stronger electrostatic attraction to the magnetite surface at those conditions. Specific ions will bind to the surface at unfavorable pH conditions, and specific binding acid groups will dissociate on the iron oxide surface at a higher rate than in the bulk solution for a given pH environment.

The specific binding of carboxylic acids are discussed in detail by Cornell and Schwertmann, while non-specific amines are almost entirely absent from bonding discussions (Cornell & Schwertmann, 2003). The only mention of amine binding to an iron oxide in "The Iron Oxides" is in the context of polymer hydrogen binding on page 275, in which polyacrylamide was found to have a high affinity for hematite at low concentrations in a pH range of 3.5 to 11.5 (Cornell & Schwertmann, 2003). Ammonium and amines are absent from the cation interactions listed in Table 11.3, and further absent from the competing adsorbates listed in Table 11.5 (Cornell & Schwertmann, 2003). The work of Cornell and Schwertmann may be leading researchers to believe that carboxylic acid binding to magnetite dominates amine binding so strongly that amine bonds can be ignored entirely (J. Y. Park, Choi, Baek, & Lee, 2009).

Current iron oxide nanoparticle research includes biological labeling, separations, and cancer treatments, and catalytic applications, which use ligands to create a catalytically active outer surface or serve as attachment sites for metal nanoparticles. Throughout these varied applications, carboxylic and amine functional groups are often simultaneously present during

functionalization of the particles' surfaces. Researchers frequently assume (without direct evidence) that the carboxylates will coordinate to the magnetite surface in aqueous solution while the amines do not (Durdureanu-Angheluta et al., 2012; J. Y. Park et al., 2009). For high temperature syntheses in organic solutions, it is commonplace to use a 1:1 molar ratio of oleic acid to oleylamine for magnetite functionalizations and label the resulting particles as oleic acid functionalized nanoparticles (S. Sun & Zeng, 2002).

The reasons for ignoring the possibility of amine bonding have been discussed by Klokenburg et al., whose research into the vibrational spectroscopy of magnetite/carboxylate/amine systems is worth quoting (Klokkenburg, Hilhorst, & Ern , 2007):

“On the one hand, the [FTIR] spectra do not give any clear indication of the presence of oleylamine molecules at the surface of magnetite. On the other hand, the same can be said of the spectra of the acid–base complex [known to form in a cyclohexane solution of oleylamine and oleic acid], where despite the lack of direct spectral evidence, no doubt exists about the presence of oleylamine.... A chemical argument against the presence of oleylamine molecules in the surface layer is that it is unclear how it could bind to magnetite. Moreover, an oleic acid molecule cannot at the same time form a carboxylate with oleylamine and with the magnetite surface.”

FTIR analyses of magnetite particles decorated with amines and carboxylates are complicated by the overlapping absorption peaks within the fingerprint region. COO- symmetric and asymmetric stretching changes according to the way it is bound to the magnetite surface (Zhang et al., 2006). Figure 4.2 demonstrates the three different binding modes for carboxylates on magnetite.

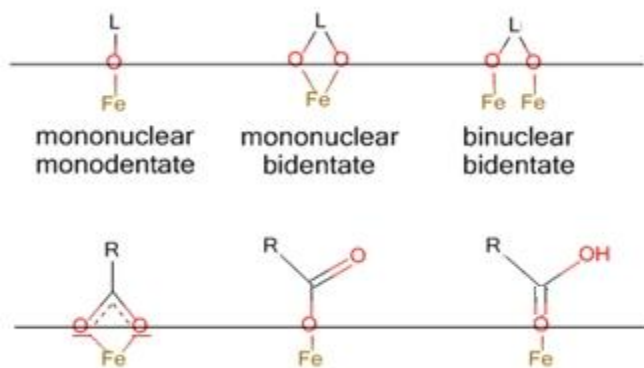


Figure 4.2 Ligand coordination modes on the surface of iron oxide and their carboxylate analogues (modified from Cornell and Schwertmann).

Monodentate bonds between magnetite and carboxylates result in a separation of 200-320 cm^{-1} between the absorption peaks of symmetric and asymmetric COO^- stretching. Bridging bidentate bonds correspond to a separation of 140-190 cm^{-1} , while chelating bidentate bonds show a separation of $<110 \text{ cm}^{-1}$ (L. Zhang et al., 2006). Another additional complication is the formation of an acid-base complex between an amine and carboxylate, whose peaks appear around 1575 and 1400 cm^{-1} for a complex of oleyl amine and oleic acid in cyclohexane (Klokkenburg et al., 2007). N-H deformation absorbs at wavenumbers very near the absorptions of water, around 1045, 1560, and 1620 cm^{-1} (F. Zhang et al., 2011). There is one important FTIR peak outside the region of overlap between amines and carboxylates from which the presence or absence of free carboxylic acids can be determined. The presence of a peak around 1710 cm^{-1} indicates the presence of uncoordinated COOH (Shafi et al., 2001; Yang et al., 2010).

Some high temperature decomposition schemes have utilized particle precipitation in the presence of di-amines in order to create amine-decorated outer surfaces (Qu, Ma, Riviere, Zhou, & O'Connor, 2012; L. Wang, Bao, Wang, Zhang, & Li, 2006). The creation of such materials proves that amines can form stable bonds to the magnetite surface, although the exact chemistry of such binding is currently unknown. Because amine decorated NPs have so many applications (Qu et al., 2012; L. Wang et al., 2006; F. Zhang et al., 2011), an aqueous functionalization path to such materials may have widespread applications. Carboxylate-magnetite bonds from amino-acid ligands may prove more stable than amine-magnetite bonds (Garrett et al., 2006).

In high temperature decomposition synthesis with di-amines, sodium acetate is typically present during the simultaneous step of particle precipitation and ligand attachment. However, the attachment of carboxylates to particle surfaces during these synthesis is neither proven nor disproven. The FTIR are frequently misinterpreted, with carboxylate peaks ignored entirely (F. Zhang et al., 2011). The attachment of amines to magnetite surfaces during high temperature synthesis in non-polar solvents may indicate that amines bind directly (Qu et al., 2012; L. Wang et al., 2006). Inner shell, direct binding is exclusive to specific binding moieties, along with the ability to coordinate despite unfavorable pH environments. The binding mechanism between the amines and magnetite surface could be the same in aqueous post-precipitation functionalizations.

The simultaneous coordination of amines and carboxylic acids to iron oxides may have effects which are currently unnoticed due to the current common view of amines as non-specific binding moieties. In catalytic applications, unnoticed carboxylate and amine attachments are likely to have effects on catalyst performance. This may affect the researchers' ability to understand the behavior of materials, tune their catalysts for optimal performance, or cause useful synthetic routes and catalytic materials to be overlooked.

For biological researchers, particle surface charge is an important parameter which determines the stability of particles in biologically relevant aqueous conditions. The coordination of amino acids through amine groups is likely to have a substantial effect on particle surface charges, by lowering the number of positively charged amine groups facing outward in solution, and also by increasing the number of carboxylate moieties facing outward. Research groups who are focusing on this issue are currently ignoring the possibility of amine binding (J. Y. Park et al., 2009), as seen in Figure 4.3.

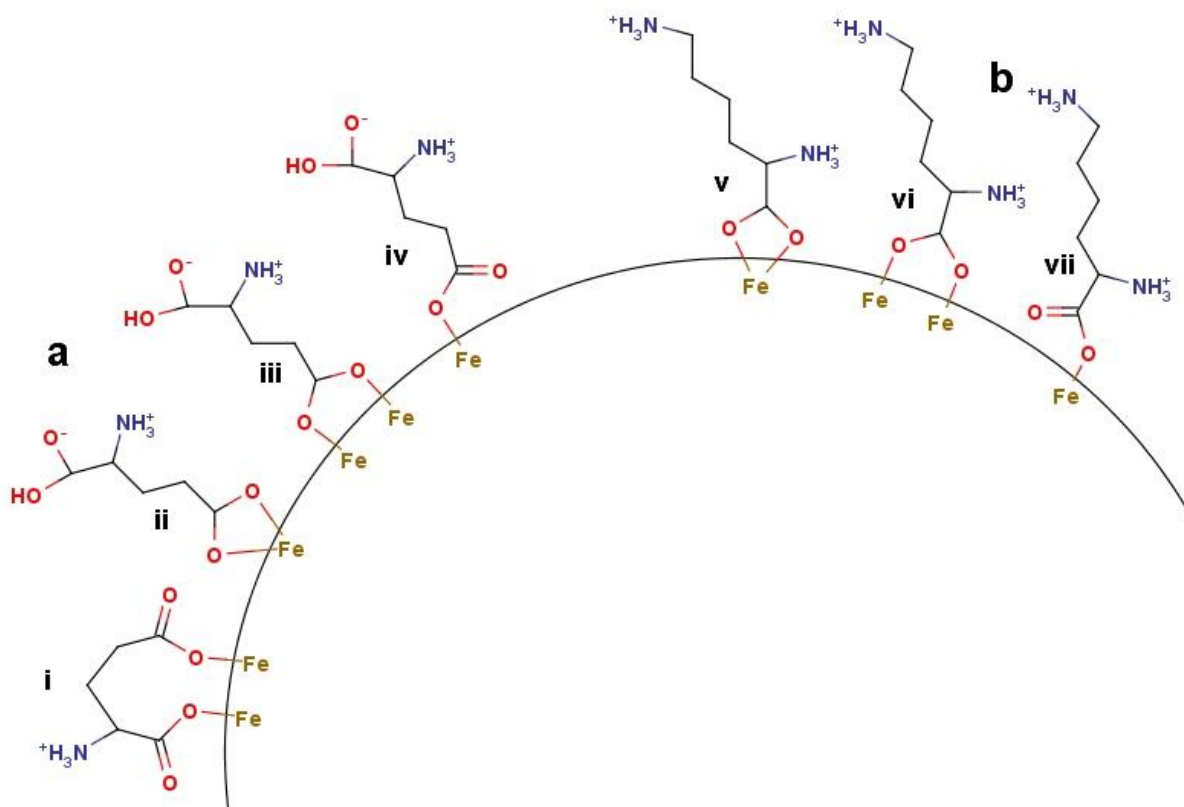


Figure 4.3 Commonly recognized potential binding structures for amino acids do not include the possibility of amine coordination to the particle surface. These possible binding structures come from a study on the surface charge of particles functionalized with the amino acids a) i-iv) Glucine, b) vi-vii) Lysine (adapted from J.Y. Park et al., 2009).

4.3 Syntheses and Characterization

4.3.1 Monolayer Chain Length Analysis

To study the effect that chain length has on functionalized magnetite particles with ligands attached through carboxylic acids, synthesis conditions were set up to attach the amino acids in a low pH environment. As shown in Figure 4.4, the precipitated magnetite particles were functionalized with amino-acids after washing away excess ammonium ions and lowering the pH to 5 with hydrochloric acid. After ligand addition, the particles were heated for 3 hours at 80°C and then cooled to room temperature before being washed three times with excess water to remove unbound ligands and ions.

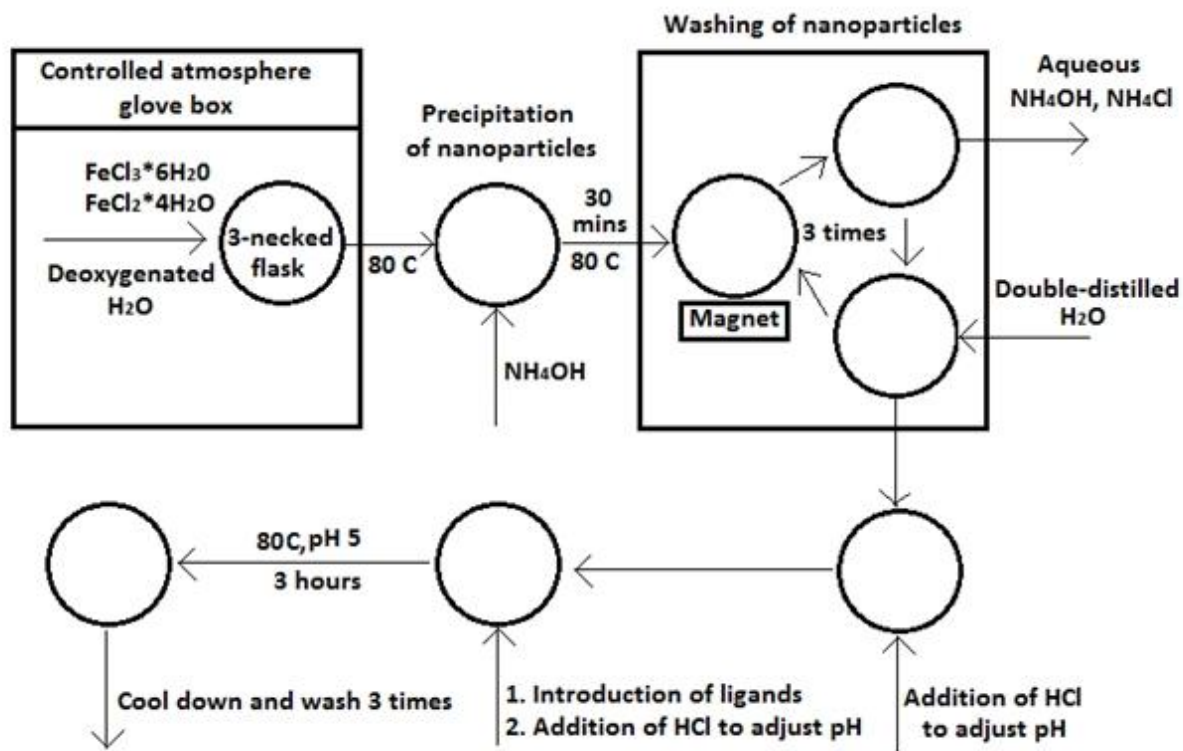


Figure 4.4 Synthesis with 3 washes to remove ammonium ions after particle precipitation, pH adjustment to 5 before and after ligand addition, and 3 hours of ligand functionalization at 80°C.

Surprisingly, titration indicated that the pH of the washed particles was below 7, and that addition of a base was necessary for titration of each amino-acid functionalization. 11-aminoundecanoic acid functionalized and 6-aminohexanoic acid functionalized particles gave acid loadings of 0.12 mmolH⁺/g and 0.1 mmolH⁺/g, respectively. If the ligand attachment had been through the carboxylic acid as expected, the outward facing amines would be expected to create a pH above 7, requiring acid for neutralization. This surprising result led to further study of the binding of amino acids to magnetite.

If amine binding is occurring in aqueous magnetite functionalizations at a wide pH range, and amines form direct bonds to the iron oxide surfaces, then amines fit the definition of specific binding moieties (Cornell & Schwertmann, 2003). In that case amines might coordinate to the nanoparticle surface and compete with carboxylic acids even when the pH of the solution is low

and the nanoparticle amphoteric surfaces have a positive charge. This has important ramifications for a variety of biological and catalytic nanoparticle applications, which often involve syntheses in the presence of both carboxylic acids and amines.

4.3.2 Optimization of pH and Temperature

In addition to chain length effects, we wanted to study the effects of pH and temperature on the formation of carboxylic acid bonds during the ligand attachment phase of the synthesis. Some researchers use temperatures around 80°C for carboxylate-magnetite binding (Roonasi & Holmgren, 2009), although the synthesis procedures we had adopted for functionalization with 11-sulfoundecanoic acid utilized a temperature of 95°C for ligand attachment (Sahoo et al., 2005). To avoid the complications of possible sodium sulfite/sulfate impurities left over from the synthesis of the 11-sulfoundecanoic acid, 11-aminoundecanoic acid was selected as a substitute ligand. We synthesized particles at pH values of 3 and 5 with temperatures at 75°C and 95°C. The procedure for this synthesis is given in Figure 4.5.

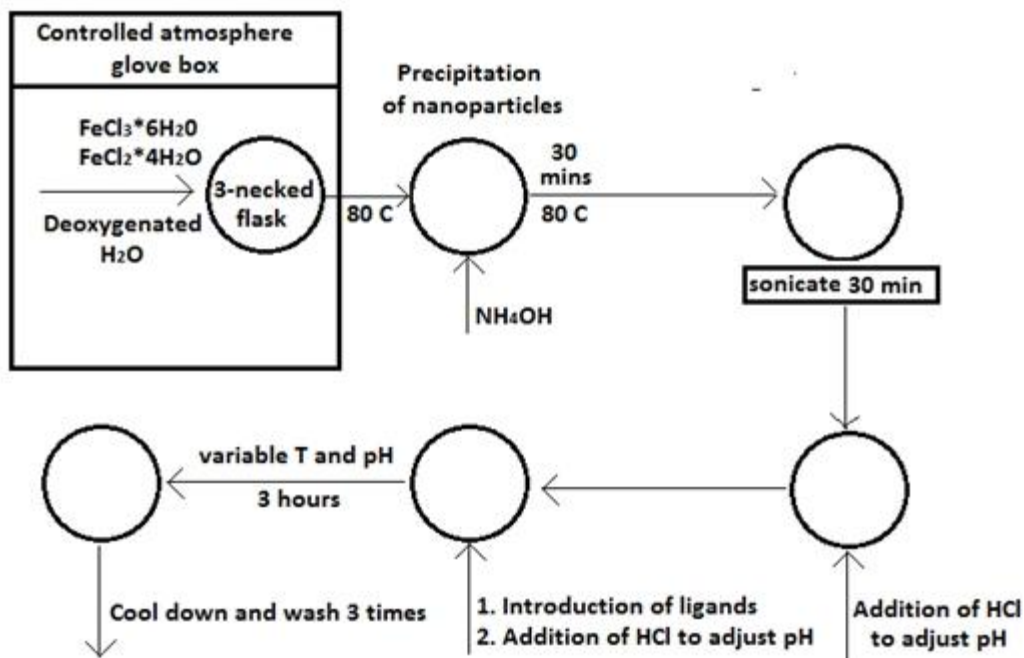


Figure 4.5 Synthesis with sonication prior to pH adjustment, with NH_4^+ ions present during ligand bonding, at varied temperatures and pH environments.

This synthesis differs from the previous 11-aminoundecanoic acid functionalization process in that the ammonium ions were not washed off before adjustment of the pH. After washing to remove excess ligands, the particles were characterized by TGA, titration, and DRIFTS. Figure 4.6 shows the weight loss for the four different batches of particles.

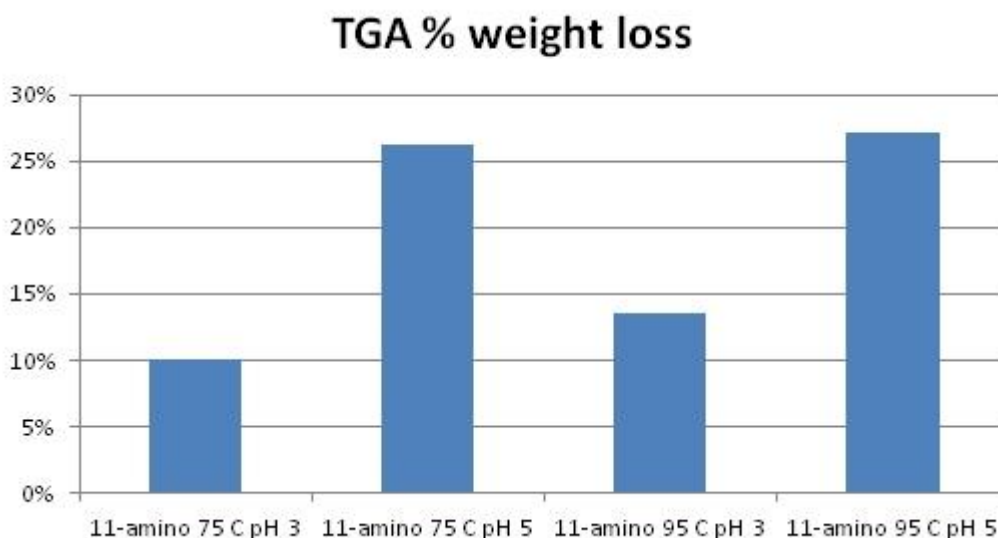


Figure 4.6 Thermogravimetric analysis of iron oxide particles functionalized with 11-aminoundecanoic acid at different temperatures and pH environments.

TGA analysis indicates that the particles functionalized at pH 5 have a higher packing density than particles synthesized at pH 3. Figure 4.7 may provide some explanation for this trend. Because the magnetite surface is essentially saturated with excess protons around pH 5, lowering the pH beyond that value does not increase the available binding sites for carboxylic acids. The lower ligand loading at pH 3 may result from the decreased ionization of the carboxylic acid moiety (Cornell & Schwertmann, 2003). The TGA ligand loading of 25% may indicate higher than monolayer coverage, possibly due to hydrogen bonding of unbound ligands, although the reason for lower hydrogen bonding at pH 3 is unclear.

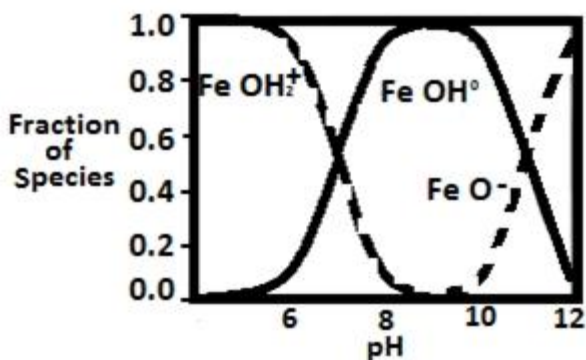


Figure 4.7 Magnetite’s amphoteric variations in surface concentrations of FeOH²⁺, FeOH⁰, and FeO⁻ at different pH chemical environments (modified from Cornell and Schwertmann 2006).

The specific binding acids can dissociate at a lower pH on the iron oxide surface than they do in solution, but there is a trade-off between the desirable increased protonation of the magnetite surface and the undesirable protonation of carboxylic acids (Cornell & Schwertmann, 2003). The optimal pH for carboxylate bonding to magnetite may be around 5 (Cornell & Schwertmann, 2003). The acid loadings measured by titration are given below in Table 9.

Table 9 Acid loadings measured by titration for magnetite particles functionalized with 11-aminoundecanoic acid at varying temperatures and solution pH.

| Synthesis conditions | mmol H ⁺ /gram |
|----------------------|---------------------------|
| 11-amino 75°C pH3 | 0.24 |
| 11-amino 75°C pH5 | 0.12 |
| 11-amino 95°C pH3 | 0.4 |
| 11-amino 95°C pH5 | 0.04 |

Assuming a monolayer ligand footprint of 0.21 nm² (Sahoo et al., 2005), an 11-aminoundecanoic acid loading of 1mmol/g corresponds to a 20% weight loading. The acid loadings from Table 9 indicate that the magnetite is not binding exclusively through the amine. If the sample synthesized at 95°C pH 3 were bonded to magnetite through amine bonds only, the 25% TGA weight loss would indicate an acid loading of 1.25 mmol/g. More information regarding the simultaneous binding of carboxylates and amines can be found in the DRIFTS spectra in Figure 4.8.

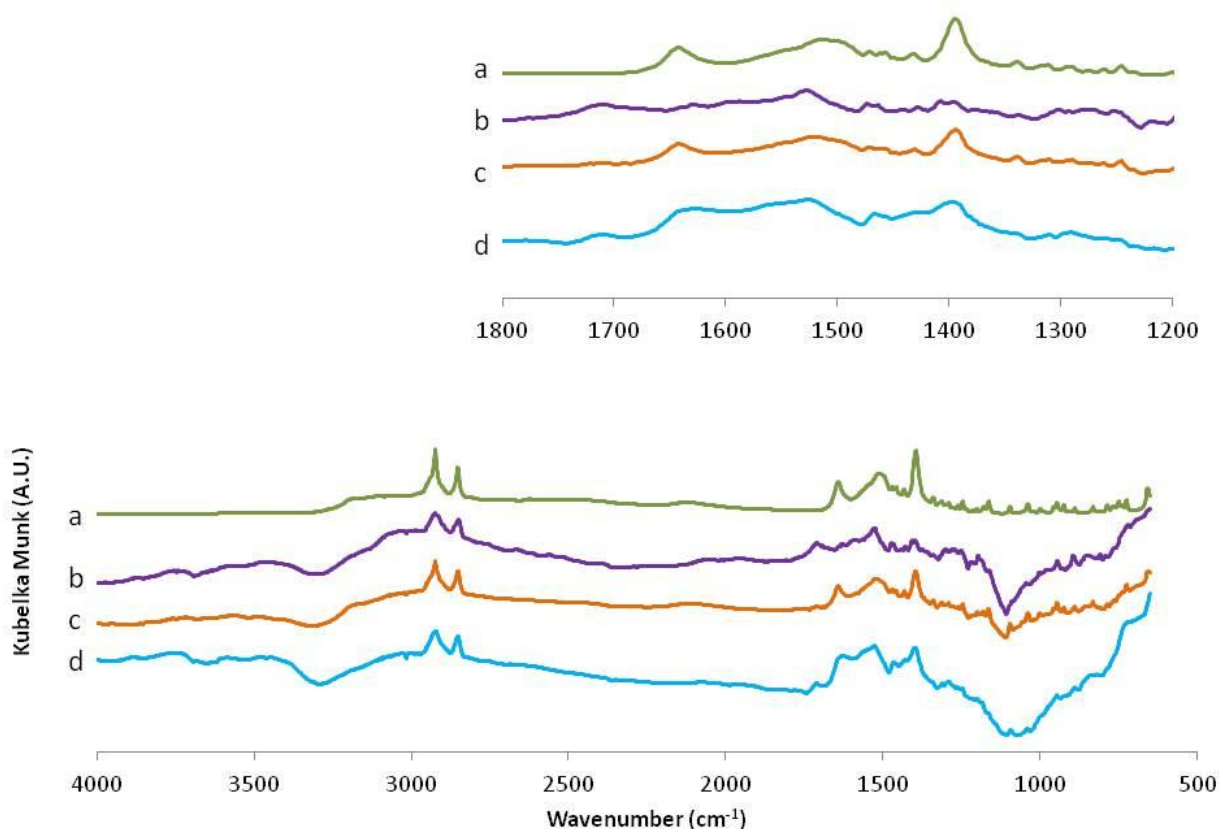


Figure 4.8 DRIFTS spectra of a) 11-aminoundecanoic acid, and particles whose functionalization occurred at b) 95°C, pH3 c) 75°C, pH 5, d) 75°C, pH 3

Peaks common to both the ligand and the functionalized particles include the alkane chain vibrations near 2850 and 2920 cm^{-1} , C-H symmetric bending around 1400 cm^{-1} , and a broad OH/NH shoulder from 3100 to 3300 cm^{-1} . Interpreting the region from 1200 to 1800 cm^{-1} is difficult because of the many possible molecular vibrations that may be responsible for a single peak, but a few definitive conclusions can be drawn. The spectra reveal similar molecular absorption wavenumbers for samples from the different synthesis conditions. Vidal-Vidal et al. suggest that peaks at 1393 and 1514 cm^{-1} are indicative of NH_2 bending modes for N- Fe^{3+} bonds, and some data from other researchers may support that conclusion (Qu et al., 2012). The sample synthesized at 95°C pH 3 has a smaller NH_3 bending peak at 1643 cm^{-1} , and larger peaks near 1393 and 1514 cm^{-1} , compared to the other samples.

The COOH peak around 1710 cm^{-1} is present in all three samples but not in the 11-aminoundecanoic acid, with larger peaks here corresponding to larger measurements of acid groups from titration. This indicates that all three samples contain some carboxylic acids which are not coordinated to the iron oxide surface.

4.3.3 Carboxylate/Amine-Magnetite Binding in the Presence of Ammonium Ions

The first two synthesis schemes indicated that amines were binding to magnetite in aqueous solution at a low pH range, resulting in an outer surface with acid groups available for titration, presumably from excess carboxylic acids. Next, an attempt was made to intensify the amine bonding and decrease the carboxylate bonding by increasing the pH, removing FeOH_2^+ on the magnetite surface that may be preferentially conducive to carboxylate bond formation, and increasing the concentration of FeO^- species which may increase the likelihood of amine bond formation. While varying the pH, we wanted to minimize the influence of different ammonium ion concentrations on the formation of carboxylate-magnetite bonds. Although some researchers dispute the importance of ammonium and amines for carboxylate-binding to magnetite surfaces (Klokkenburg et al., 2007), other research shows that the presence of ammonium ions can have a significant effect (Machunsky, Grimm, Schmid, & Peuker, 2009).

Because the ammonium ions may play a role in the formation of carboxylate bonds, they were added in excess to isolate the effects of varying the pH and the ligand chain length. The ligands 3-aminocaproic acid, 6-aminohexanoic acid, and 11-aminoundecanoic acid were used to functionalize 4 batches per ligand at pH's of 3, 5, 9, and 10.8. Ammonium chloride was added to the higher pH batches to account for the presence of ammonium chloride in low pH solutions as a result of neutralization of ammonium hydroxide with hydrochloric acid. After 12 hours at 80°C , the particles were cooled to room temperature, washed 10 times to remove the excess ligands, and vacuum dried at 50°C . A diagram of the synthesis procedure is shown below in Figure 4.9.

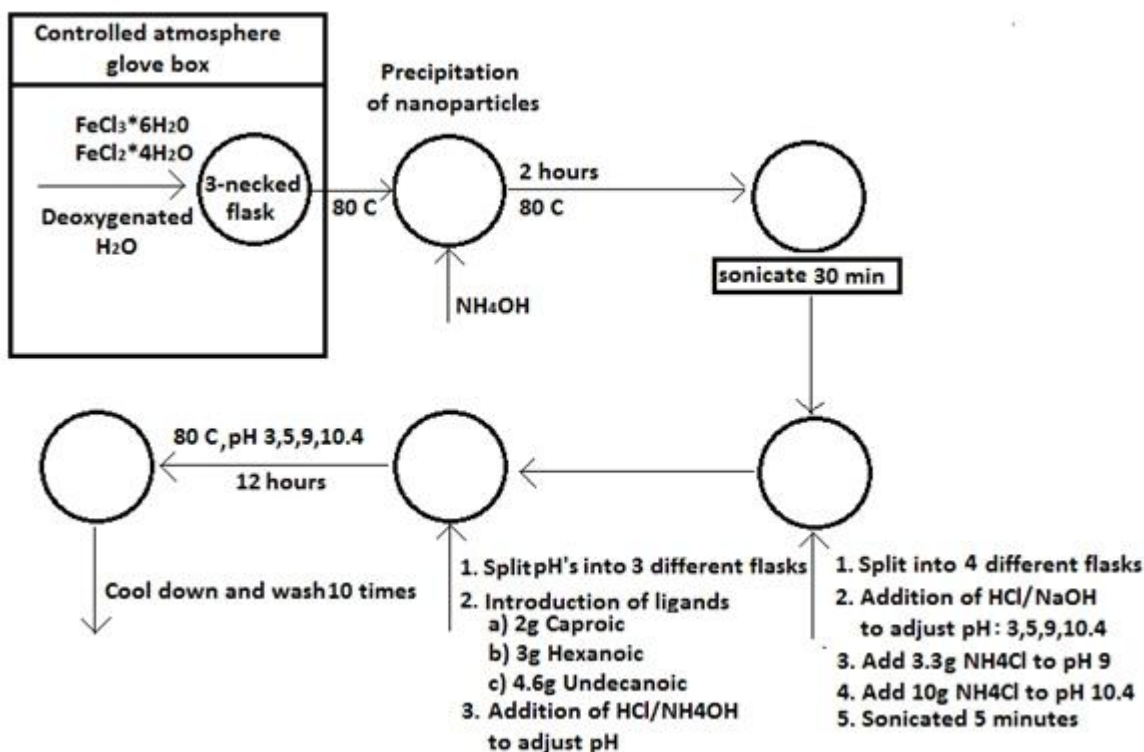


Figure 4.9 Synthesis of amino-acid functionalized particles in the presence of excess ammonium ions, at pH 3, 5, 9, and 10.4.

A specific coordinating moiety will coordinate to the magnetite surface in a variety of pH environments (Cornell & Schwertmann, 2003). Because the amines were previously seen to coordinate at low pH where electrostatic forces are unfavorable, they should also coordinate at high pH, where the electrostatic forces are more favorable between the positively charged amines and the negatively charged magnetite surface (Siddiqui et al., 2009).

XPS surveys, shown for 11-aminoundecanoic acid in Figure 4.10, give atomic concentration information which can be used to compare the loadings of ligands on the particle surfaces. The ratio of nitrogen to iron provides a measure of the ligands bound to the surface, although this measurement does not necessarily reflect the particle's overall composition.

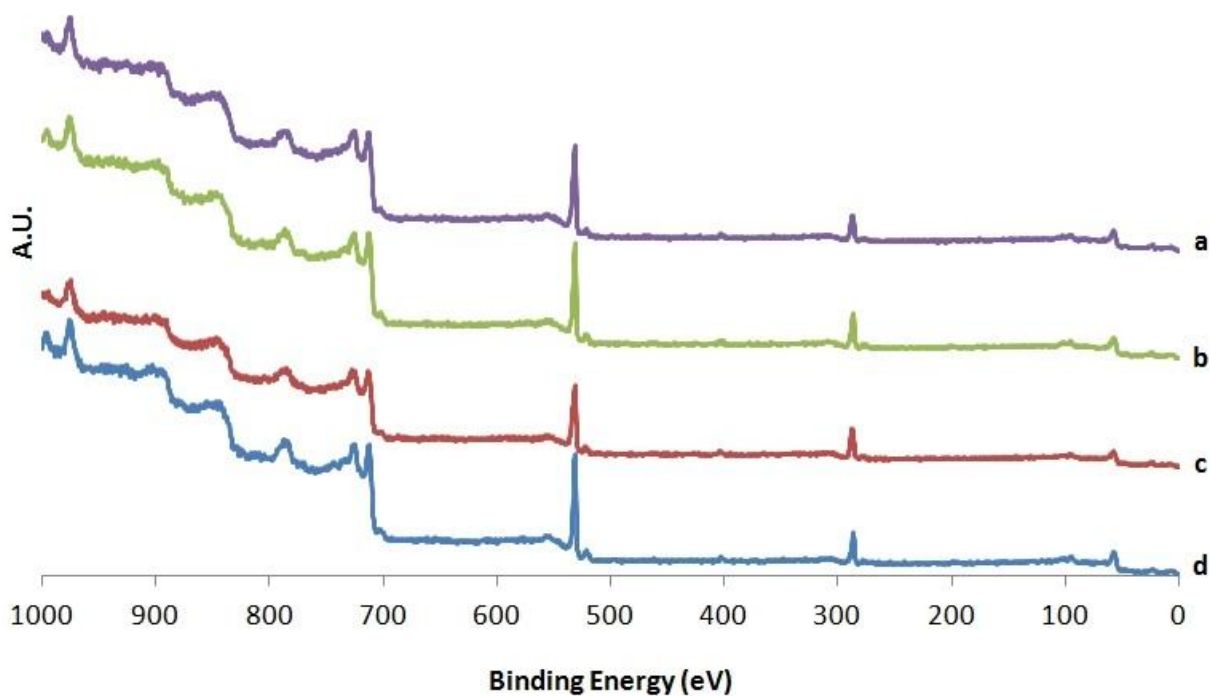


Figure 4.10 XPS survey scans of 11-aminoundecanoic acid functionalized particles in the presence of ammonium ions in a solution at a) pH 10.8 b) pH 9 c) pH 5 d) pH 3

Table 10 gives the XPS survey compositions for the functionalized particles after washing and vacuum drying.

Table 10 Nitrogen atomic compositions from XPS surveys for ligands functionalized at pH 3, 5, 9, and 10.4, with 3-aminocaproic acid, 6-aminohexanoic acid, and 11-aminoundecanoic acid.

| pH | 3-aminocaproic acid | 6-aminohexanoic acid | 11-aminoundecanoic acid | Average |
|---------|---------------------|----------------------|-------------------------|---------|
| 3 | 1.5% | 2.3% | 2.5% | 2.1% |
| 5 | 0.3% | 1.5% | 4.4% | 2.1% |
| 9 | 1.0% | 1.8% | 3.0% | 1.9% |
| 10.4 | 0.6% | 1.3% | 4.6% | 2.2% |
| Average | 0.8% | 1.7% | 3.6% | |

The XPS measurements of nitrogen composition indicate that 11-aminoundecanoic acid gives the densest monolayer on the magnetite surface at all pH values. The smaller ligands give a lower packing density, as evidenced by the lower nitrogen content, with 3-aminocaproic acid

loading lower than 6-aminohexanoic acid. The averaged nitrogen atomic compositions indicate that the pH did not play a definitive role in determining the ligand loading. The NH_4^+ cations may reduce the electrostatic repulsions between RCO_2^- and FeO^- species. FTIR for the particles are given in Figure 4.11.

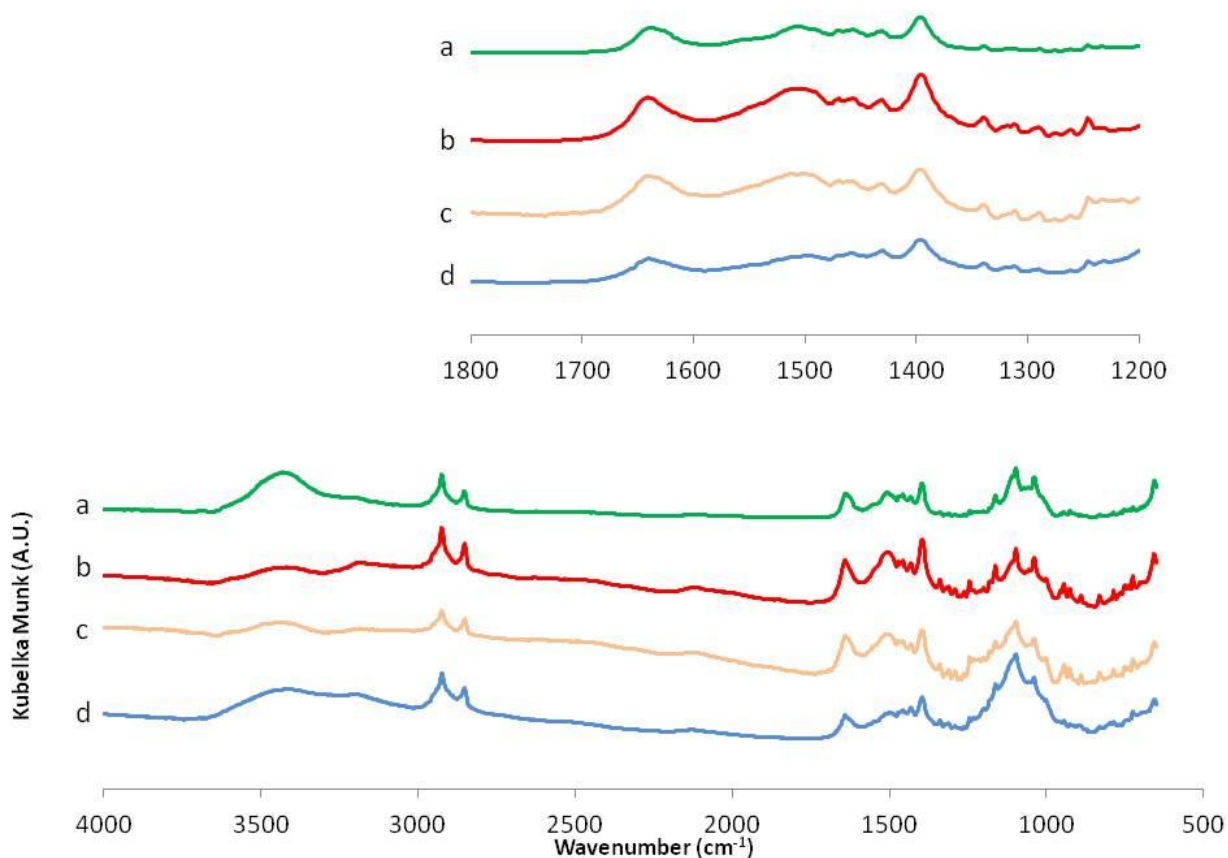


Figure 4.11 DRIFTS spectra for particles functionalized with 11-aminoundecanoic acid at a) pH 3 b) pH 5 c) pH 9 d) pH 10.4

The similarity between binding is indicated by the very similar spectra at all pH conditions. The samples do not show a peak at 1710 cm^{-1} , indicating that there are no free carboxylic acids. This stands in contrast to the binding of samples from Figure 4.8 which were synthesized at comparable pH conditions but in the absence of ammonium ions. The presence of ammonium ions during the functionalization step has lowered the amine-magnetite bonding which causes the carboxylic acids to face outward in solution.

4.3.4 11-Aminoundecanoic Acid Functionalization Without HCl

In the following set of experiments, the functionalization did not involve the use of hydrochloric acid to adjust the pH. Two batches were synthesized according to the Massart co-precipitation method, and the functionalization conditions varied only as to the presence of residual ammonium hydroxide and ammonium chloride. After precipitation, one batch of particles was sonicated for ten minutes and washed by magnetic extraction in between sonication steps. The sonication/washing was repeated twice more. After the third wash, 1g of the particles were sonicated for another 10 minutes, then 0.75g of the 11-aminoundecanoic acid was added and the particles were sonicated for another 10 minutes before being returned to heating. The flasks were kept at 80°C for 12 hours, and then cooled to room temperature while stirring, and washed 10 times by magnetic extraction to remove excess ligand.

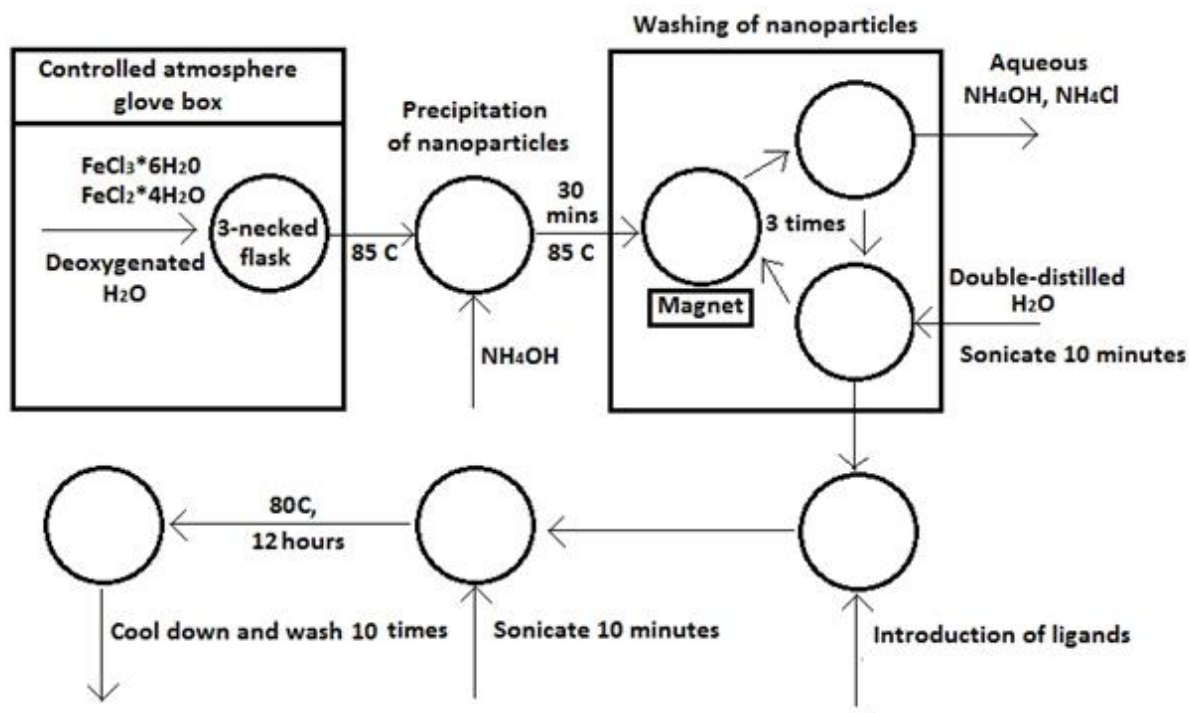


Figure 4.12 Synthesis of two batches without HCl addition. One was washed as shown above. The other batch was functionalized the same way, except that it was not washed.

The synthesized particles were subject to potentiometric titration, XPS, FTIR, and TGA. To compare independent measurements of amine binding on the magnetite surface, it should be possible to use a combination of TGA and titration to obtain the excess carboxylate or amine

groups facing outward into solution. That number should be confirmed by using XPS to measure the N_{1s} orbital and detect the species in various binding arrangements. An uncoordinated amine should have a lower electron density and higher N_{1s} binding energy than an amine bonded to Fe^{3+} .

The washed particles showed a TGA weight loss of 5%, and a titration showed 0.12 mmol OH^- /gram. From TGA, the total ligand loading is 0.25 mmol/g. An excess of 0.12 mmol OH^- indicates that 0.13 mmol of ligands are equally divided between outward facing carboxylates and amines, canceling each other out from the titration. The zeta potential indicated a surface charge of -22 mV, as shown in Figure 4.13.

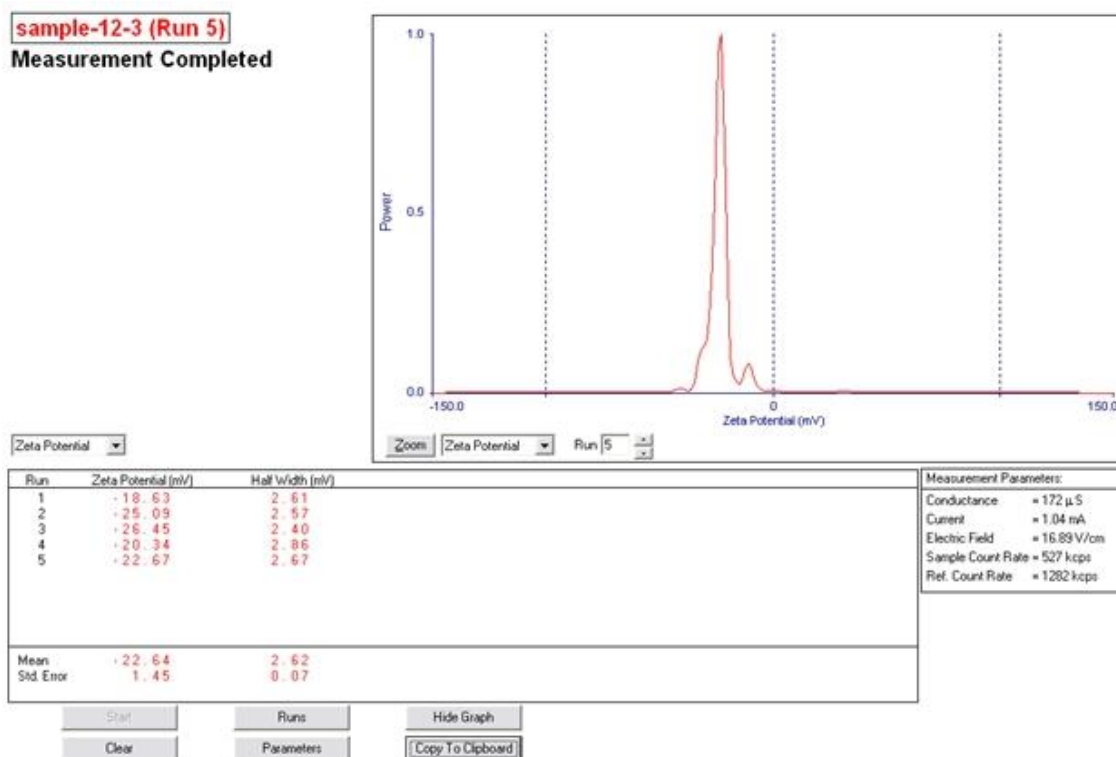


Figure 4.13 Zeta potential measurements for the sample synthesized after removal of ammonium ions.

Particles synthesized in the presence of NH_4OH and NH_4Cl showed a TGA weight loss of 10%, and a titration indicated 0.03 mmol OH^- /gram. From the TGA analysis, the ligand loading is 0.5 mmol/g. An excess of 0.03 mmol outward facing amines indicates that 0.47 mmol of ligand are split equally between outward facing carboxylates and outward facing amines,

cancelling each other out from titration. The zeta potential was measured at -1.1 mV, as shown in Figure 4.14.

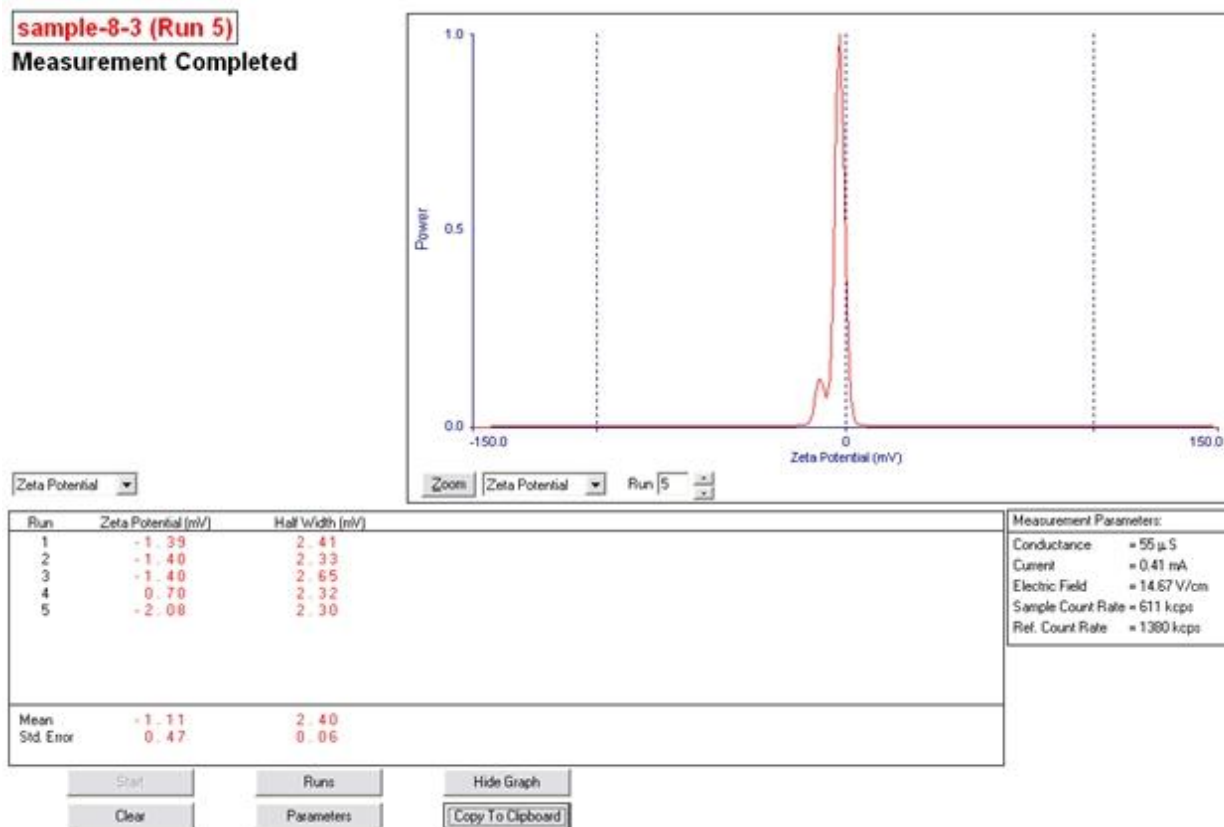


Figure 4.14 Zeta Potential measurements for the sample synthesized without removal of ammonium ions.

If the amines faced only outwards, then the zeta potential would be expected to be positive. The negative zeta potentials measured indicate a surface with an excess of carboxylic acid moieties. This data indicates that the nitrogen binding to the magnetite surface was lower when the magnetite surface had a more negative charge: when $\text{NH}_3/\text{NH}_4\text{OH}/\text{NH}_3\text{Cl}$ ions were present. The ammonium ions may compete with the amines for binding sites on the iron oxide surface (Machunsky et al., 2009). DRIFTS spectra provide additional information about the molecular binding in these samples, as shown in Figure 4.15.

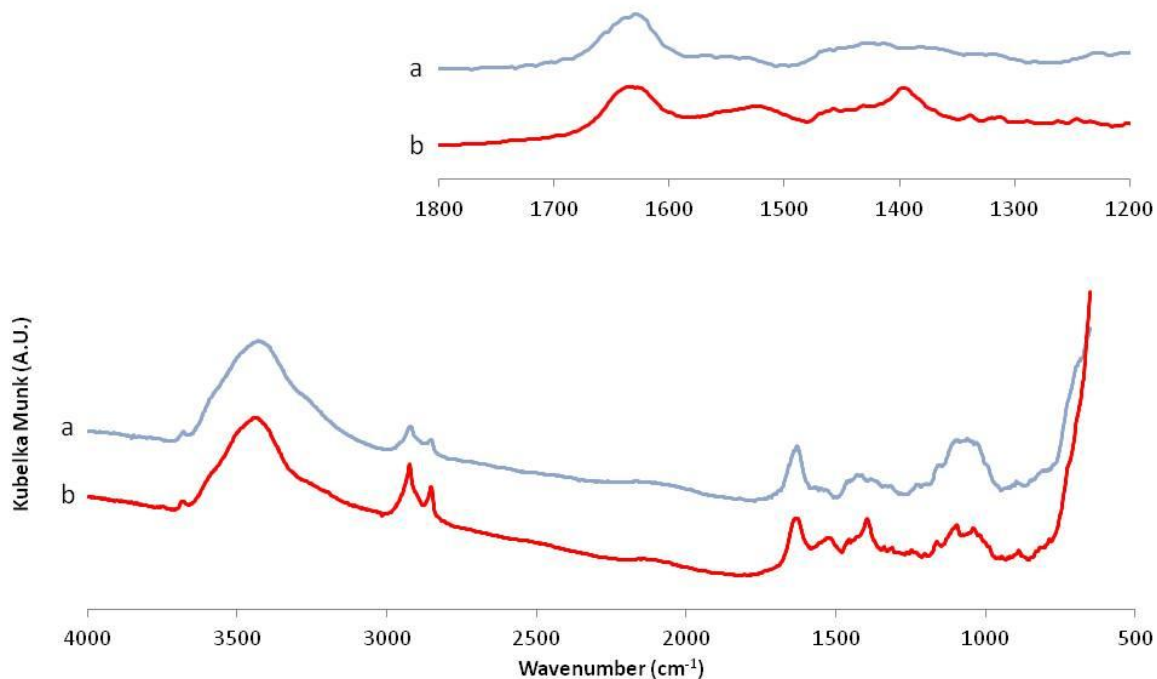


Figure 4.15 DRIFTS spectra for particles synthesized a) in the presence of ammonium left over from precipitation and b) after washing to remove ammonium ions

The peaks at 1515 and 1393 cm^{-1} are more distinct in the sample synthesized in the absence of ammonium ions, possibly indicating the binding of amine groups to Fe^{3+} (Garrett et al., 2006). Neither one has the large peak at 1710 cm^{-1} . The lack of a peak at 1710 cm^{-1} may result from interactions between outward facing carboxylates and amines that shift the absorption wavelengths of the carboxylate symmetric and asymmetric stretching. The peak's presence would therefore correspond to a surface excess of carboxylic acids high enough for some carboxylate stretching to occur in the absence of interaction with nearby amines. Electrostatic considerations prescribe that RNH_3^+ groups would bind to FeO^- sites and not to FeOH_2^+ sites or FeOH^0 sites. However, if the binding mechanism is through the lone electron pair of RNH_2 (Garrett et al., 2006), then the assumed electrostatic effect may be reversed.

4.4 Conclusions

The idea to conduct synthetic experiments using amino acids as a substitute for sulfonic-carboxylic di-acids was based around the notion that amines would not form bonds to magnetite nanoparticles in aqueous conditions. Additionally, particles with carboxylate-magnetite bonds and outward facing amines are a potential base catalyst, as well as a useful material for further biological or catalysis-oriented secondary functionalizations. 11-aminoundecanoic acid gave higher packing densities than 6-aminohexanoic acid or 3-aminocaproic acid. Functionalizations at 95°C gave a higher loading of 11-aminoundecanoic acid than at 80°C.

Titration, FTIR, and Zeta potential analysis indicated that the amino acids were not attaching according to the understanding we had developed in our literature review, or in the manner that would be predicted by simple electrostatic considerations. In our hands, the amino acid ligands were binding to the magnetite surface through amines as well as carboxylates, at higher pH and also at lower pH. A thorough literature review indicated that FTIR was frequently misinterpreted by groups using carboxylates and amines to functionalize magnetite nanoparticles, and that amine bonding had not been disproven.

Titration measurements of hydroxide loading should be proportional to outward facing amine loadings and have an inverse relationship to amine-magnetite bonding. In our functionalizations, conditions of higher pH and higher concentration of ammonium ions result in an increased tendency for ligands to orientate with carboxylate-magnetite attachments and outward-facing amines. The mechanism of amine attachment to the iron oxide surface is uncertain. Ammonium ions may compete with amines for binding sites on the iron oxide surface.

FTIR analysis of bonding structures is complicated by the many overlapping regions between water, amines, and carboxylates. The FTIR analysis may also be affected by the formation of carboxylate-amine hydrogen-bonding structures in solution, as well as the presence of potential impurities such as carbamic acid from air, and residual ammonium ions. The continued study of amino acid binding to magnetite is likely to be beneficial for catalytic and biological research.

Chapter 5 - Toward Monodisperse Nanoparticles with Functional Monolayers

5.1 The Importance of Monodispersity

Aqueous co-precipitation is a facile method for rapid production of iron oxide nanoparticles well suited to screening a large number of ligands, but the particles produced have a polydisperse diameter range from 6 to 20 nm. The variation in chemical, magnetic, and agglomerate properties between particles of 6 nm and 20 nm diameters are likely to be significant (Hill, Millstone, Banholzer, & Mirkin, 2009; J. Park et al., 2004; Siddiqui et al., 2009; D. Wang et al., 2011; L. Zhang et al., 2006). The polydispersity of co-precipitation prevents an analysis of how diameter influences the properties of monolayer functionalized particles. The attainment of monodisperse particles with functional monolayers will allow for definitive measurement of catalytically important properties for individual particle sizes, instead of averaging the properties of particles that may vary significantly.

5.2 Toluene Mixed Solvents

The literature contains a large number of potential routes to monodisperse particles, but only two methods of synthesizing monodisperse particles avoid high cost solvents and reagents. One route involves a low temperature synthesis scheme which was developed to obtain monodisperse particles with a monolayer of oleic acid (Jiang et al., 2011). It involves the precipitation and subsequent reflux of particles in a solvent mixture composed of toluene, water, and ethanol, with excess oleic acid ligand, under argon gas at atmospheric pressure. This method of synthesizing monodisperse particles has the advantages of avoiding high temperatures and expensive solvents. However, the advantage of lower temperature may be somewhat offset by the environmentally unfriendly nature of toluene, and the energy consumed during the reflux process. A full life cycle assessment to compare the toluene reflux method with the high temperature decomposition method would be an important step before industrial scale-up.

5.2.1 Toluene Mixed Solvents With 11-Bromoundecanoic Acid

A solvent mixture of 60 mL water, 80 mL ethanol, and 140 mL toluene was placed in a round bottom flask in an oil bath and purged with nitrogen gas for 30 minutes while being heated

at 74°C. Attached to the flask was a reflux column with cooling water. 2.12g of iron (II) chloride tetrahydrate and 4.31g iron (III) chloride hexahydrate were dissolved in the solvent mixture to give an $\text{Fe}^{3+}:\text{Fe}^{2+}$ ratio of 1.5 and a total iron concentration of 0.095 mmol Fe/L.

24.54g of 11-bromoundecanoic acid were stoichiometrically neutralized with 3.4g of sodium hydroxide, and the ligand salt was added to the mixture so as to give a ligand: Fe^{2+} ratio of 8:1. After 4 hours of reflux at 74°C, the black mixture of solvent and particles was added to excess ethanol and magnetically separated, then re-dispersed in n-hexane. After about two weeks, the particles had turned orange, indicating oxidation of the magnetite. The color change from black to orange after a few weeks, possibly indicating that the ligand bonding stability and magnetite core protection achieved with this technique was inferior.

5.2.2 Toluene Mixed Solvents With 11-Bromoundecanoic Acid

After initial success with the 11-bromoundecanoic acid as the ligand, the system was modified for 11-sulfoundecanoic acid. It was considered that the divalent di-acid would be water soluble enough to avoid the need for toluene. 84.2g of 95% pure ethanol were added to 55.8g of water, and out-gassed with nitrogen flow for 30 minutes at 74°C in the round flask below the reflux column. 1.058g of iron 2 chloride tetrahydrate and 2.157g iron 3 chloride hexahydrate were dissolved in the solvent mixture to give an $\text{Fe}^{3+}:\text{Fe}^{2+}$ ratio of 1.5 and a total iron concentration of 0.095 mmol Fe/L.

12.27g of 11-sulfoundecanoic acid were neutralized with 1.7g of sodium hydroxide in 20 mL of water, stirred for 20 minutes at 60°C, and added to the synthesis flask. Immediately, an orange precipitate formed and stuck to the sides of the vessel. No further attempts were made to modify the system. The neutralization may have been inadequate, affected by impurities of the synthesized 11-sulfoundecanoic acid, or the technique may be simply incompatible with sulfonic acid moieties. Although our investigation and success with this mixed solvent synthesis technique was limited, optimization of the system may have some potential for the generation of large quantities of monodisperse particles with monolayers of functional ligands.

5.3 Aqueous Digestive Ripening

Instead of using the presence of ligands during particle formation as a method of controlling particle growth and synthesizing monodisperse particles in the manner of Jiang et al, we wanted to see if the monodispersity could be achieved after particle formation. Other researchers have had success with the digestive ripening of gold nanoparticles in aqueous solution (Stoeva, Smetana, Sorensen, & Klabunde, 2007). Digestive ripening is a process utilizing the reflux of a solution of nanoparticles, solvent, and an appropriate ligand to drive the particle size distribution toward an equilibrium monodisperse diameter. Digestive ripening can cause smaller particles to get larger and cause larger particles to get smaller, unlike the process of Ostward ripening which only leads to increases in particle diameters.

In the next experiments, 11-aminoundecanoic acid functionalized magnetite particles were digestively ripened in aqueous solution. Iron oxide nanoparticles were precipitated in the usual way, then heated at 95°C for 6 hours with equal parts 11-aminoundecanoic acid and magnetite nanoparticles, then cooled to room temperature and magnetically washed. Refluxing the particles in pH 4 water under nitrogen atmosphere for 72 hours produced TEM images of particles with diameters much smaller than what we were looking for, as shown in Figure 5.1.

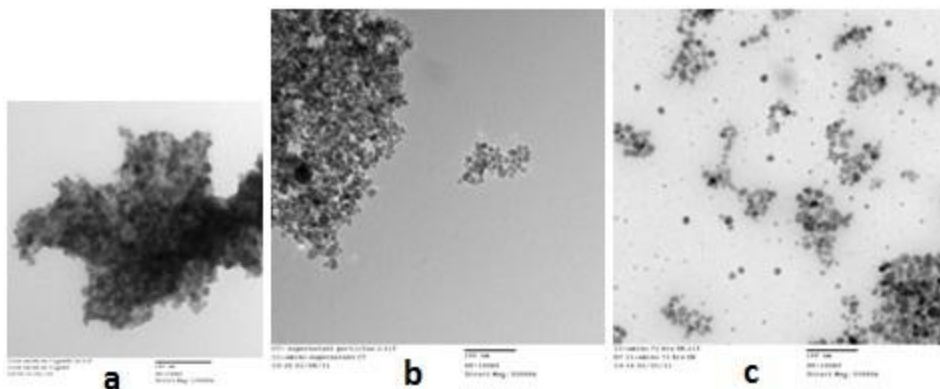


Figure 5.1 Magnetite nanoparticles after a) synthesis by co-precipitation, b) heating with 11-aminoundecanoic acid in pH 5 water at 95°C for 6 hours c) digestively ripened with boiling water reflux for 72 hours in pH 4 solution.

An ideal monodisperse synthesis technique should be tunable for particle diameters between 5-20 nm. The TEM images may indicate that the digestive ripening would have led to an equilibrium size smaller than 5 nm. Although the results appear somewhat promising,

optimization of the system may require a significant amount of further experiments, and larger particle diameters might not be achievable. Additionally, the digestive ripening process probably exposes bare magnetite particle cores to the solvent/ligand solution, where they would likely oxidize in the presence of sulfonic acids. For these reasons, attention was turned to high temperature decomposition methods of particle synthesis.

5.4 High Temperature Decomposition

The second economical monodisperse particle synthesis scheme that we attempted to modify involves a unique high temperature decomposition method which differs from other high temperatures syntheses in its utilization of relatively inexpensive reagents and solvents (J. Park et al., 2004). In this synthesis scheme, a precursor material (composed of an Fe^{3+} atom complexed with three carboxylic ligands) is decomposed at high temperatures in an organic solvent to produce monodisperse magnetite nanoparticles functionalized with the ligand. In addition to economic considerations, this method has excellent potential for facile tailoring of the particle diameters. The choice of the solvent determines the size of the nanoparticles, with higher boiling points producing larger diameters, ranging from 6nm to 22nm (J. Park et al., 2004). This method may provide a robust method for the creation of monodisperse particles with different diameters, but with the same functional ligand attached in a quasi-monolayer on the surface.

5.4.1 High Temperature Decomposition With 11-Bromoundecanoic Acid

Our first modification of this synthesis scheme involved substituting the ligand 11-bromoundecanoic acid for oleic acid. To create a precursor compound, 31.8g of the 11-bromoundecanoic acid was neutralized with 4.8g of sodium hydroxide to form a sodium carboxylate salt in 60 mL of water, and then mixed with 80 mL of ethanol, and 140 mL of hexane. 10.8g of iron (III) chloride hexahydrate were added to give a 3:1 molar ratio of ligands to iron. According to Park et al., heating for four hours at 70°C with magnetic stirring at 600 rpm allows the mixing of the aqueous and nonpolar phases, so that relatively non-polar carboxylate ligands can form bonds with the aqueous iron atoms, as shown in Figure 5.2. Because the Fe^{3+} atom was already fully oxidized, there was no need for a nitrogen atmosphere or other steps to prevent iron oxidation. The sodium and chloride ions have an affinity for the aqueous phase, while the non-polar precursor compound has an affinity for the hexane phase. After the precursor formation reaction was complete, the hexane phase was separated, washed

three times with 30mL of warm de-ionized water, placed into a glass flask, and then evaporated at 80°C to leave behind the orange precursor material.

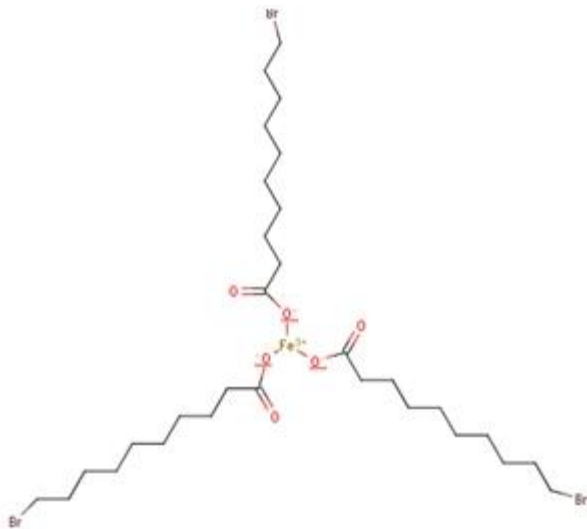


Figure 5.2 Precursor composed of an Fe³⁺ atom coordinated to the carboxylates of three molecules of 11-bromoundecanoate.

19.32g of the precursor complex were placed in a Parr reactor with 113.86g of hexadecene and 3g of 11-bromoundecanoic acid, giving a molar ratio of 2:1 for the complex to bare ligand. The precursor was heated in the solvent, with nitrogen atmosphere and mechanical stirring, at a rate of 3.3°C/min from 20°C to 320°C. It was held at 320°C for 30 minutes, and then cooled under constant stirring. The resulting product solution was black, indicating the formation of magnetite.

The particles we functionalized with 11-bromoundecanoic acid and hexadecene could not be extracted by the force of the supermagnet's external magnetic field. Although no TEM images were taken to confirm the particle diameters, the diameter reported by Park et al. of 6 nm for the hexadecene solvent with oleic acid ligand may have given a similar result for our ligand. To remove excess solvent, a vacuum heating apparatus was used to remove the hexadecene at 60°C, although some liquid remained in the flask. In an attempt to remove excess ligand, a dilute solution of sodium hydroxide was added to the hexadecene to increase ligand solubility in water and potentially separate the hydrophobic functionalized particles in the hexane phase. The

particles did not remain in the hexane phase, and instead distributed in the aqueous phase. This effect was attributed to a bi-layer, as shown in Figure 5.3.

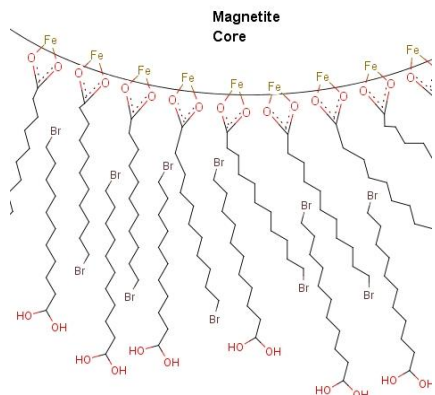


Figure 5.3 A bi-layer of 11-bromoundecanoic acid around a magnetite nanoparticle.

This batch was not adjusted further. The particles remained black for many months afterward. That chemical stability may have been due to the bi-layer preventing diffusion of oxidizing species to the magnetite surface, and not necessarily do to a monolayer superior to that created by the toluene mixed solvent synthetic technique. If the excess ligand were removed, FTIR analysis would be insightful regarding the carboxylate-magnetite binding. Substitution of the bromine group with a sulfite group on the surface of the particles may produce monodisperse particles with functional sulfonic acid monolayers.

5.4.2 High Temperature Decomposition With 11-Aminoundecanoic Acid

For the next set of experiments, 11-aminoundecanoic acid was used as the ligand for precursor formation. Because the 11-aminoundecanoic acid is soluble in water, the hexane phase was unnecessary. 25.7 grams of 11-aminoundecanoic acid were added into 750 mL of de-ionized water and heated to 60°C. 41.0 grams of iron III chloride FeCl_3 was dissolved in 100 mL of water, and added slowly to the aqueous 11-aminoundecanoic acid solution to give a 3:1 molar ratio of ligand to iron. An orange precipitate formed very quickly as drops of iron chloride solution were added. The aqueous solution was stirred for 3 hours at 60°C. Although the precursor tended to settle into the bottom of the container, it was very difficult to thoroughly wash. After a few failed attempts to extract the aqueous phase from above the delicate precursor

layer, a centrifuge was employed to speed the separation. 100 mL volumes of aqueous precursor were centrifuged at 10,000 RPM for 15 minutes. The aqueous layer was poured off, and fresh water was added to the precursor which was stirred and redissolved into the water. After two more centrifugal washings, the precursor was removed from the centrifugation containers, and it was seen to have a gradation in color from orange to darker red. The material was vacuum dried at 60°C overnight. XPS surveys of the orange precursor and the darker red material are shown in Figure 5.4.

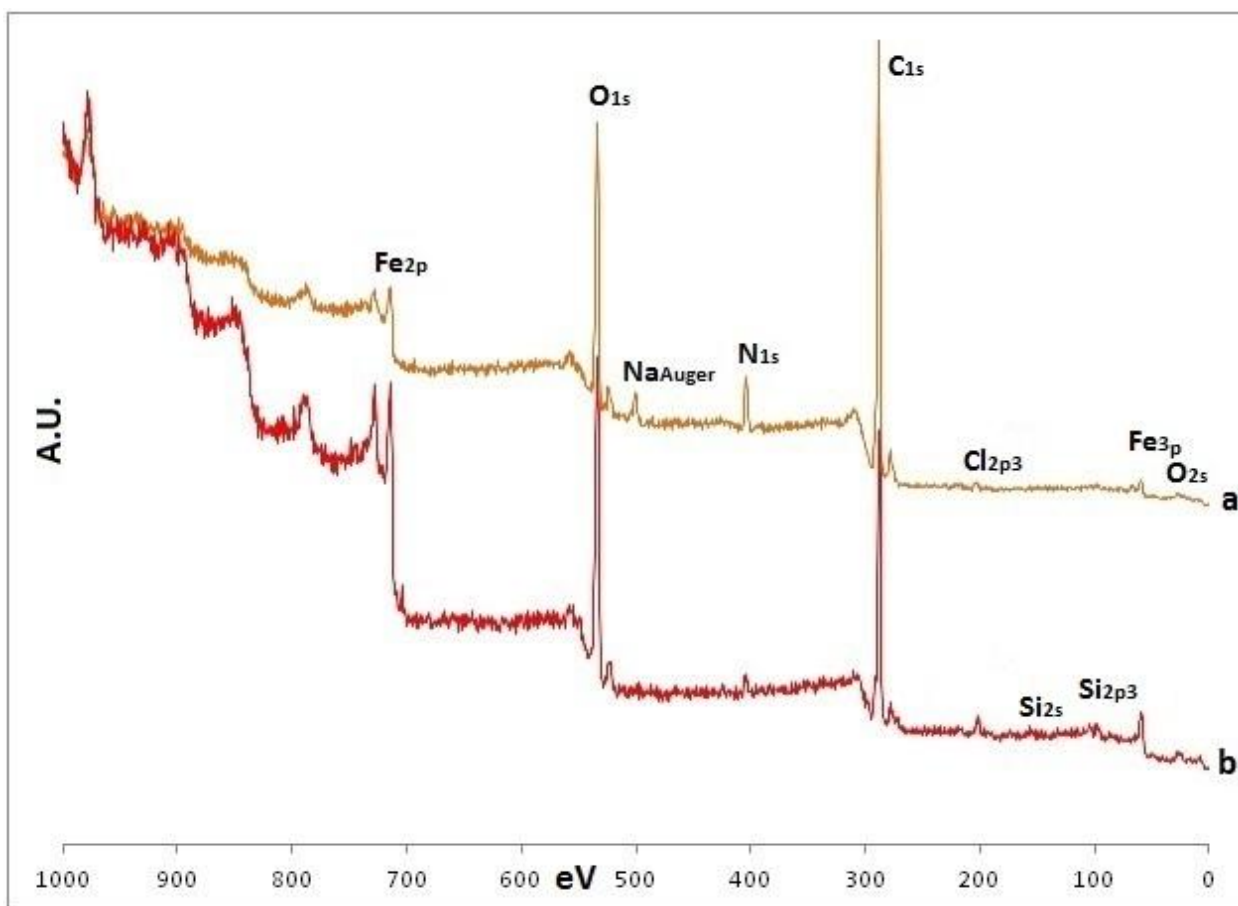


Figure 5.4 XPS surveys of the a) 11-aminoundecanoate Fe³⁺ precursor and b) darker precursor material separated or chemically changed during three centrifugal washes.

Impurities in the precursor result in peaks for Si_{2p₃} at 104 eV, Si_{2s} at 154 eV, Na_{Auger} at 500 eV, and Cl_{2p} at 201 eV. The iron chloride aqueous solution stuck to the glass flask strongly, staining it and possibly dissolving some of the silica. Silica was probably introduced by etching of the glass by the iron chloride or sodium hydroxide pellets. The darker red material shows an

increased atomic concentration of chlorine. A precursor with only two 11-aminoundecanoic ligands and a single chloride anion would have a greater density than a 3-ligand complex, explaining why the stratification took place during centrifugation.

The washed orange precursor was decomposed in a Parr reactor as follows. 17.35 g of precursor were added to 200g trioctylamine along with 2.65g of 11-aminoundecanoic acid. The solution was stirred and heated at 3.3°C/min, but started making a boiling sound around 160°C and vibrated until it was stopped at 230°C. The reactor contents were cooled, and inside there was a black solid deposited on all the surfaces, with white globules on top of it, and a white liquid.

To examine the reaction more closely, the procedure was carried out in a 30mL pressurized glass reaction vessel, using 2g trioctylamine, 0.0265g 11-aminoundecanoic acid, and 0.1735g 11-aminoundecanoic acid precursor. There was no change in appearance until 110°C, when there appeared to be excess precursor around the top of the liquid level, the same color as the liquid but not dissolved. At 120°C, the slightly darker liquid started forming solids around the top of the meniscus. At 125°C, the solution began to clear, while particles formed and eliminated sight of the stir bar. At 128°C, the particles precipitated out of solution, but were resuspended when the stirring rate was increased. After holding at 128°C for ten minutes, the solution was cooled and the liquid had the cloudy appearance of small particles. It is unclear why this reaction occurred, and what the products were that formed. The amines may have interfered with the carboxylate-iron bonding and caused the iron particles to precipitate at a lower temperature. Impurities such as sodium, chlorine, and silica may also have affected the reaction.

In an attempt to alter the synthesis of the precursor, the iron chloride solution and 11-amino acid solution were heated to 60°C before mixing, and then stirred for three hours at 60°C. The result was a black solution, unlike the orange precipitate described in the paper and seen with the 11-bromoundecanoic acid. The black color generally indicates the formation of magnetite. In this case, the addition of sodium hydroxide caused the material to precipitate and

become a darker orange than the precursor prepared by first adding sodium hydroxide to the 11-aminoundecanoic acid.

Alternatively, if the 11-aminoundecanoic acid solution was titrated from 6.04 to 7 using dilute HCl, the result was an initially deep red solution that became slightly darker while heating to 40°C and then much darker above 40°C, similar to the formation of the black material with the addition of exclusively 11-aminoundecanoic acid, but red instead of black.

5.5 Conclusions

Two potential paths to monodisperse particles were selected from the literature and modified for preliminary experiments. Both synthesis routes avoid the use of expensive solvents and reagents, but neither is capable of producing functional monolayers on monodisperse particles without further adjustments. The mixed solvent system of toluene, ethanol, and water was successful in using 11-bromoundecanoic acid in place of oleic acid to synthesize a black solution that was likely magnetite particles. However, those particles oxidized and turned orange within a few weeks. An attempt to substitute 11-sulfoundecanoic acid for oleic acid, and remove toluene from the solvent mixture, produced an oxidized orange material that was insoluble in the ethanol/water solvent system. A preliminary attempt at the digestive ripening of co-precipitated iron oxide nanoparticles utilized 11-aminoundecanoic acid in an aqueous solution of pH 4 water for 72 hours. TEM images confirmed the generation of numerous particles smaller than 5 nm. Achieving larger diameters, if possible, may require significant optimization of reflux conditions.

A high temperature precursor composed of three 11-bromoundecanoic acid ligands and one iron atom was synthesized in a mixed solution of hexane and water. The precursor was decomposed at high temperature in hexadecene and produced a solution of black particles that could not be removed by an external magnetic field. Removing excess ligand and solvent from these particles was much more difficult than the washing away of excess di-anionic ligands from magnetically extractable water soluble particles. 11-aminoundecanoic acid was used to produce precursor compounds, although the aqueous solubility of the precursor increased the difficulty of purification to remove sodium and chloride ions. Centrifugation produced or separated a darker material that had higher chlorine content. The chemistry of amino acid precursors and their high

temperature decomposition can be studied with FTIR and XPS, and may one day prove successful for producing monodisperse particles with functional monolayers.

Chapter 6 - Future Work

6.1 Sulfonic Acid Monolayers on Iron Oxide Nanoparticles

Aqueous precipitation was a useful method to produce particles quickly and easily for the purpose of screening molecules as candidates for the creation of stable, functional monolayers. The polydisperse particles produced allowed us to determine that di-acids with alkane chains are good candidates for creating acid-catalytic monolayers on the particle surfaces. However, the acid loading (L. Zhang et al., 2006), catalytic activity (Mbaraka & Shanks, 2006; D. Wang et al., 2011), ligand chain disorder (Gubin & Kataeva, 2006), and other important properties may vary substantially depending on the particle size and resulting surface curvature. In order to advance the understanding of acid monolayer functionalized iron oxide nanoparticles and develop these materials toward the goal of industrial scale catalytic cellulose hydrolysis, the next step is to create monodisperse batches of nanoparticles which are functionalized with monolayers of 11-sulfoundecanoic acid, 11-aminoundecanoic acid, and 10-phosphono,1-decanesulfonic acid. The combination of measurements for determination of ligand loading should include titration, ICP, TGA, TEM, XRD, and zeta potential analysis. Titration, TGA, and ICP can give measurements of the ligand weight percent loading, while TEM and XRD can measure the particle diameters for calculation of specific surface areas.

Careful TEM sample preparation may allow precise measurements of particle diameters for rigorous quantification of the specific surface area. Agglomerates may distort the particle size histograms and resulting calculations of specific surface area, if agglomeration rates vary by particle size (Siddiqui et al., 2009), and if agglomeration reduces the likelihood of producing a measurement of the particle diameter. Manipulation of pH, temperature, and other environmental conditions should be used in combination with sonication to reduce agglomeration and allow for accurate measurements of individual particles. TEM grids should have a small quantity of solution completely evaporated on the surface, instead of using a dipping or contact time preparation method which may preferentially deposit particles of particular diameters.

Future particle syntheses should utilize more difficult synthetic methods such as high temperature decomposition and digestive ripening in mixed solvents. Experimentation with the precursor approach developed by Park et al. is likely to be fruitful (J. Park et al., 2004). Alternatively, post-precipitation functionalization methods involving substitution of carboxylates and phosphonates for more weakly bound moieties such as cyclohexamine (Garrett et al., 2006) may be the most facile route toward monodisperse particles with functional monolayers. If monodisperse particles are synthesized with ligands that are easily displaced, that will avoid the need for strongly acidic ligands to be present during particle nucleation and growth. Sonication during solvent reflux may assist the breakdown of agglomerates and assist the growth of tightly packed monolayers on all particle surfaces. Instead of working immediately towards economical synthesis strategies, it would be expedient to ignore economic evaluations of synthetic methods during the research stage of evaluating material properties.

Future syntheses of 11-sulfoundecanoic acid should utilize the oxidation of thiols, or some other pathway that eliminates sodium sulfite and any other di-anions from the synthesis procedures. Purification of sodium sulfite salts from carboxy-sulfonic di-acids is difficult, and the highest purification we achieved showed some residual sodium which could have been sodium sulfite impurity or sodium carboxylate/sulfonate. The effects of the variability in sulfate and other impurities may be significant in determining the stability and activity of the particles produced. Since atomic concentrations of sulfur are used to identify ligand loss, the elimination of sulfur impurities is also important for accurate measurements of ligand dissociation. If the use of sodium sulfite as a reagent is necessary, careful removal of impurities should be verified by ICP, XPS, and/or other atomic concentration measurements.

The measurement of catalytic activity and stability for the acid functionalized nanoparticle system is inherently more complicated than for non-particulate solid acid catalysts, due to the variability in agglomeration and incomplete separation of the particles from solution. Determination of ligand dissociation by analyzing the sulfur content of the supernatant is further limited by an inability to differentiate between functionalized particles and dissociated ligands. ICP analysis should be conducted at each step of the reaction cycles, analyzing virgin catalyst solutions and all recycle reaction solutions, as well as supernatants after catalyst extraction.

The activity seen for bare particles in sucrose hydrolysis is surprising and points to an interesting line of future work. To our knowledge, iron oxide nanoparticles have not been previously shown to be catalytically active for hydrolysis of carbohydrates. Because the iron oxide is amphoteric, there could be some bi-functional acid-base type molecular interactions. Future work should examine the roles that particle size, agglomeration, and ligand packing density (possibly by using a catalytically inactive ligand instead of the sulfonic acid) play in the activity of magnetite particles for sucrose hydrolysis. Additionally, there are methods for synthesizing iron oxide nanoparticles which involve only the mechanical grinding of reagents (Ngo et al., 2010). These methods are more cost-efficient and energy efficient than co-precipitation or high temperature decomposition. The particles produced from mechanical grinding have higher polydispersity, but the energy savings and scale-up potential could be advantageous if bare iron oxide nanoparticles were found to be active for important conversions of biomass into industrial chemicals.

6.2 Amine-Magnetite Bonding

The development of amine-magnetite surface science should continue until the questions regarding amine-magnetite bonding characterization and quantification are resolved. Such resolution will have important ramifications for a variety of biomedical and catalytic iron oxide research projects. Amine binding studies should eliminate ammonium as a precipitation agent during synthesis, so as to eliminate the possibility of ammonium distorting the data taken by XPS, FTIR, ICP, and other measurement techniques. If the effects of ammonium are to be studied, ammonium chloride should be added methodically, rather than using ammonium hydroxide left over from precipitation.

All steps including the drying of samples for analysis should be conducted in a nitrogen glovebox or other sealed containers to prevent contamination with carbon dioxide from the air. CO₂ may interact with amines or the iron oxide surface and affect measurements of carboxylates and amines. The effects of carbon dioxide presence should be analyzed using pressurized gas introduced in a methodical way.

In the same way that in-situ FTIR can give interesting information about gas phase catalysis, in-situ liquid FTIR could give interesting information about the behavior of acid monolayer nanoparticle catalysts. Liquid phase FTIR may help analyze the attachment and dissociation of ligands, and that data may be useful in optimizing synthesis conditions. Far IR in the range of 100-500 cm^{-1} may also provide useful information for understanding the iron oxide surface and ligand bonding (Garrett et al., 2006).

6.3 Bi-Functional Catalysts

The creation of an ordered, dual-functional catalytic outer surface on iron oxide nanoparticles may result in the production of a new class of recyclable catalysts whose acid and base groups work independently or in a concerted mechanism (Apesteguía, Hattori, & Setoyama, 2006). When working independently, the bi-functional catalysts enable reactions which would otherwise require separate catalytic steps (Gianotti, Diaz, Velty, & Corma, 2013). Flexible synthetic strategies allow comparisons between the effectiveness of the concerted mechanisms for various combinations of functional groups (Brunelli, Venkatasubbaiah, & Jones, 2012).

Binary mixtures of ligands can form patches or stripes on nanoparticles (BRAUN, 2004; X. Liu, Yu, Kim, Marnett, & Stellacci, 2012), with differences in ligand chain lengths directly affecting spontaneous ligand arrangement patterns. By synthesizing a dual-ligand mixture of 11-aminoundecanoic acid and 11-carboxyundecanol in the presence of ammonium chloride at alkaline pH, it should be possible to create bi-functional acid-base catalysts with the synthetic techniques demonstrated in this work. Additionally, if one of the ligands is adjusted for a shorter or longer chain length, it may increase the patterns that place different moieties next to each other. Increasing the length of the secondary ligand, to 16-aminohexadecanoic acid for example, may result in a more stable monolayer than what would be created by using a shorter molecule. The choice of which ligand should be longer could be determined by a cost analysis of available ligands, or perhaps the two alternatives could both be synthesized and compared.

The creation of multi-functional catalysts of various monodisperse diameters may open a floodgate of new environmentally superior catalysts. The thermal decomposition synthetic techniques may allow for the binding of multiple moieties in arrangements which differ from

those arrangements obtained through aqueous functionalization, by either increasing or decreasing the relative importance of kinetic factors vs. thermodynamic driving forces.

For iron oxide nanoparticles, the bonding mechanisms of carboxylic and phosphonic acids are understood much better than the bonding of amines. If amine-magnetite bonding can be understood and controlled, it may open up another path to the creation of ordered bifunctional monolayers. Because the carboxylate and phosphonate ions are negatively charged, and the amines are positively charged, the simultaneous attachment of these moieties on iron oxide surfaces may result in spontaneous ordering. This is another reason why a resolution of uncertainties regarding the binding of amines to iron oxides may be of importance to the development of advanced catalytic materials.

6.4 Atom Transfer Radical Polymerization (ATRP)

Monolayer optimization on monodisperse particles may contribute significantly to the development of polymer sulfonic acid catalysts using ATRP. Past research on sulfonic polymer magnetite particles involved either the direct attachment of initiators on the magnetite surface (G. Li, Fan, Jiang, & Gao, 2004), attachment of a silica shell which served as the substrate to which initiator molecules are attached (Long & Jones, 2011), or the use of a monolayer with no polymerization initiator, which remains unattached to the surrounding polymer layer (Feyen et al., 2010; Y. Wang et al., 2003). Each technique has problems requiring further resolution. Magnetite-silica-polymer composites have shown some deactivation due to polymer loss and desulfonation (Long & Jones, 2011). Improving the stability of magnetic cores and polymer attachment has been achieved with a heavily crosslinked polymer matrix, although extensive crosslinking may reduce the accessibility of acid sites and the activity for catalysis of cellulose and other biomaterials.

Direct attachment of initiators has utilized a ligand substitution process to create acid polymeric materials whose structural stability is provided by cross-linking of the polymer chains (G. Li et al., 2004). Feyen et al. have avoided attaching any initiators in their preparation of polymeric nanoparticle acid catalysts, instead using a layer of 16-heptadecanoic acid as a ligand (Feyen et al., 2010). A high degree of cross-linking (achieved by using 100% divinylbenzene

monomer) was shown to be necessary to maintain the stability of the iron oxide cores through multiple reactions.

Instead of using an exchange substitution method to displace oleic acid with an initiator ligand (G. Li et al., 2004), it may be possible to attach an initiator ligand directly on the particle surface in a monolayer immediately after or during the precipitation of the particles. Or, it may be possible to attach initiator molecules to the tails of a ligand monolayer on the surface of particles. 11-aminoundecanoic acid, 2-bromo-2-methylpropanoyl bromide, and the amide product of their reaction are good candidates for these approaches, as shown in Figure 6.1. One-step attachment of initiator ligands to particle surfaces, as opposed to substitution after the particle precipitation step, may lead to a higher ligand loading on the particle surface. An optimized, more tightly packed monolayer may offer a higher degree of protection for the iron oxide cores. By attaching inexpensive initiator ligands in a packed monolayer on the particle surfaces, and thus avoiding the use of silica and ligand substitution while reducing the need for cross-linking, it may be possible to lower the cost of catalyst production and simultaneously achieve a greater stability and activity in the resulting sulfonic acid polymer material. It may also reduce the costs of catalyst production by eliminating the need for the step with excess initiator present to displace the original ligand.

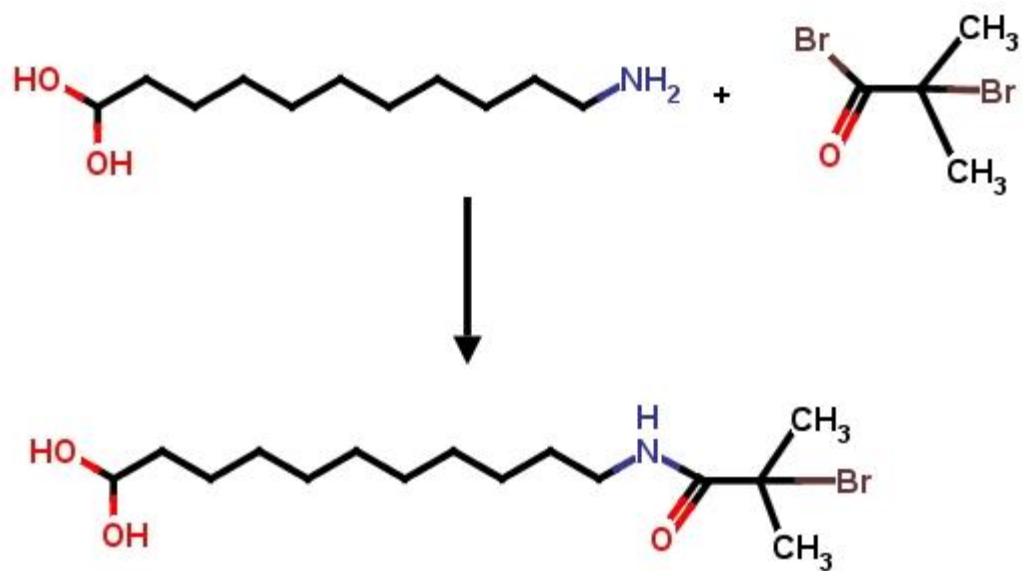


Figure 6.1 11-aminoundecanoic acid can form an amide bond to 2-bromo-2-methylpropanoyl bromide

References

- Adachi, Y., Cohen Stuart, M., Ohshima, H., Hajdú, A., Illés, E., Tombácz, E., & Borbáth, I. (2009). Surface charging, polyanionic coating and colloid stability of magnetite nanoparticles. *Colloids and Surfaces A: Physicochemical and Engineering Aspects*, 347(1), 104–108. Retrieved from <http://www.sciencedirect.com/science/article/pii/S0927775709000065>
- Aden, A., Ruth, M., Ibsen, K., Jechura, J., Neeves, K., Sheehan, J., ... Lukas, J. (2002). Lignocellulosic Biomass to Ethanol Process Design and Economics Utilizing Co-Current Dilute Acid Prehydrolysis and Enzymatic Hydrolysis for Corn Stover Lignocellulosic Biomass to Ethanol Process Design and Economics Utilizing Co-Current Dilute Acid Prehyd, (June).
- Apesteuguía, C., Hattori, H., & Setoyama, T. (2006). Acid–base bifunctional catalysis: An industrial viewpoint. *Catalysis Today*, 116(2), 250–262. Retrieved from <http://www.sciencedirect.com/science/article/pii/S092058610600215X>
- Avdeev, M. V., Bica, D., Vékás, L., Marinica, O., Balasoiu, M., Aksenov, V. L., ... Schreyer, A. (2007). On the possibility of using short chain length mono-carboxylic acids for stabilization of magnetic fluids. *Journal of Magnetism and Magnetic Materials*, 311(1), 6–9. doi:10.1016/j.jmmm.2006.11.155
- Bartczak, D., & Kanaras, A. G. (2010). Diacetylene-containing ligand as a new capping agent for the preparation of water-soluble colloidal nanoparticles of remarkable stability. *Langmuir : the ACS journal of surfaces and colloids*, 26(10), 7072–7. doi:10.1021/la9044013
- Binder, W. H., & Weinstabl, H. C. (2007). Surface-Modified Superparamagnetic Iron-Oxide Nanoparticles. *Monatshefte für Chemie - Chemical Monthly*, 138(4), 315–320. doi:10.1007/s00706-007-0617-2
- Binder, W. H., Weinstabl, H., & Sachsenhofer, R. (2008). Superparamagnetic Ironoxide Nanoparticles via Ligand Exchange Reactions: Organic 1,2-Diols as Versatile Building Blocks for Surface Engineering. *Journal of Nanomaterials*, 2008, 1–10. doi:10.1155/2008/383020

- Bootsma, J. A., Entorf, M., Eder, J., & Shanks, B. H. (2008). Hydrolysis of oligosaccharides from distillers grains using organic-inorganic hybrid mesoporous silica catalysts. *Bioresource technology*, *99*(12), 5226–31. doi:10.1016/j.biortech.2007.09.033
- Bouchard, J., & Overend, R. (1992). Mechanism of dilute acid hydrolysis of cellulose accounting for its degradation in the solid state. *Journal of Wood Chemistry and Technology*, *12*(3), 335–354. Retrieved from <http://www.tandfonline.com/doi/abs/10.1080/02773819208545239>
- BRAUN, P. (2004). Spontaneous ligand organization. *Nature materials*, *3*, 281–282. Retrieved from <http://braingroup.beckman.illinois.edu/privdocs/reprints-copy/028pvb.pdf>
- Brunelli, N. A., Venkatasubbaiah, K., & Jones, C. W. (2012). Cooperative Catalysis with Acid–Base Bifunctional Mesoporous Silica: Impact of Grafting and Co-condensation Synthesis Methods on Material Structure and Catalytic Properties. *Chemistry of Materials*, *24*(13), 2433–2442. doi:10.1021/cm300753z
- Carroll, A., & Somerville, C. (2009). Cellulosic biofuels. *Annual review of plant biology*, *60*, 165–82. doi:10.1146/annurev.arplant.043008.092125
- Carvalho, F., Duarte, L. C., & Gírio, F. M. (2008). Hemicellulose biorefineries : a review on biomass pretreatments. *Journal of Scientific & Industrial Research*, *67*(November), 849–864.
- Charmot, A., & Katz, A. (2010). Unexpected phosphate salt-catalyzed hydrolysis of glycosidic bonds in model disaccharides: Cellobiose and maltose. *Journal of Catalysis*, *276*(1), 1–5. doi:10.1016/j.jcat.2010.08.006
- Chiu, C., Moore, P. B., Shinoda, W., & Nielsen, S. O. (2009). Size-dependent hydrophobic to hydrophilic transition for nanoparticles: a molecular dynamics study. *The Journal of chemical physics*, *131*(24), 244706. doi:10.1063/1.3276915
- Corma, A., Iborra, S., & Velty, A. (2007). Chemical routes for the transformation of biomass into chemicals. *Chemical reviews*, *107*(6), 2411–502. doi:10.1021/cr050989d
- Cornell, R., & Schwertmann, U. (2003). *The iron oxides: Structure, properties, reactions, occurrences, and uses* (2nd ed., p. 703). Wiley-VCH.
- Cui, J., Cao, D., & Xu, C. (2006). Synthesis of Undecanoic Acid-11-sulfonic Acid Sodium (disodium). *Chinese Journal of Synthetic Chemistry*, *14*(5), 529–531.

- Daou, T. J., Grenèche, J. M., Pourroy, G., Buathong, S., Derory, a., Ulhaq-Bouillet, C., ...
Begin-Colin, S. (2008). Coupling Agent Effect on Magnetic Properties of Functionalized Magnetite-Based Nanoparticles. *Chemistry of Materials*, 20(18), 5869–5875.
doi:10.1021/cm801405n
- De, S., Aswal, V. K., & Ramakrishnan, S. (2010). Phenyl-ring-bearing cationic surfactants: effect of ring location on the micellar structure. *Langmuir : the ACS journal of surfaces and colloids*, 26(23), 17882–9. doi:10.1021/la1036053
- Deng, Y.-H., Wang, C.-C., Hu, J.-H., Yang, W.-L., & Fu, S.-K. (2005). Investigation of formation of silica-coated magnetite nanoparticles via sol–gel approach. *Colloids and Surfaces A: Physicochemical and Engineering Aspects*, 262(1), 87–93. Retrieved from <http://www.sciencedirect.com/science/article/pii/S0927775705002438>
- Dhepe, P. L., Ohashi, M., Inagaki, S., Ichikawa, M., & Fukuoka, A. (2005). Hydrolysis of sugars catalyzed by water-tolerant sulfonated mesoporous silicas. *Catalysis Letters*, 102(3-4), 163–169. doi:10.1007/s10562-005-5850-x
- Do Kim, K., Kim, S., Choa, Y., & Kim, H. (2007). Formation and surface modification of Fe₃O₄ nanoparticles by co-precipitation and sol-gel method. *Journal of Industrial and Engineering Chemistry*, 13(7), 1137–41.
- Duan, H., Kuang, M., Wang, X., Wang, Y. A., Mao, H., & Nie, S. (2008). Reexamining the Effects of Particle Size and Surface Chemistry on the Magnetic Properties of Iron Oxide Nanocrystals: New Insights into Spin Disorder and Proton Relaxivity. *Journal of Physical Chemistry C*, 112(22), 8127–8131. doi:10.1021/jp8029083
- Durdureanu-Angheluta, A., Dascalu, A., Fifere, A., Coroaba, A., Pricop, L., Chiriac, H., ... Simionescu, B. C. (2012). Progress in the synthesis and characterization of magnetite nanoparticles with amino groups on the surface. *Journal of Magnetism and Magnetic Materials*, 324(9), 1679–1689. doi:10.1016/j.jmmm.2011.11.062
- Fan, L., Gharpuray, M. M., & Lee, Y.-H. (1987). *Cellulose Hydrolysis* (Vol. 3, p. 198). Berlin, Heidelberg: Springer Berlin Heidelberg. doi:10.1007/978-3-642-72575-3
- Feyen, M., Weidenthaler, C., Schüth, F., & Lu, A.-H. (2010). Synthesis of Structurally Stable Colloidal Composites as Magnetically Recyclable Acid Catalysts. *Chemistry of Materials*, 22(9), 2955–2961. doi:10.1021/cm100277k

- Gallezot, P. (2008). Catalytic conversion of biomass: challenges and issues. *ChemSusChem*, 1(8-9), 734–7. doi:10.1002/cssc.200800091
- Gan, Q., Allen, S. ., & Taylor, G. (2003). Kinetic dynamics in heterogeneous enzymatic hydrolysis of cellulose: an overview, an experimental study and mathematical modelling. *Process Biochemistry*, 38(7), 1003–1018. doi:10.1016/S0032-9592(02)00220-0
- Garrett, P. R., Tiddy, G. J. T., Treiner, C., Vidal-Vidal, J., Rivas, J., & López-Quintela, M. A. (2006). Synthesis of monodisperse maghemite nanoparticles by the microemulsion method. *Colloids and Surfaces A: Physicochemical and Engineering Aspects*, 288(1), 44–51. Retrieved from <http://www.sciencedirect.com/science/article/pii/S0927775706003128>
- Geboers, J. a., Van de Vyver, S., Ooms, R., Op de Beeck, B., Jacobs, P. a., & Sels, B. F. (2011). Chemocatalytic conversion of cellulose: opportunities, advances and pitfalls. *Catalysis Science & Technology*, 1(5), 714. doi:10.1039/c1cy00093d
- Gehlen, M. H. (2009). Kinetics of autocatalytic acid hydrolysis of cellulose with crystalline and amorphous fractions. *Cellulose*, 17(2), 245–252. doi:10.1007/s10570-009-9385-y
- Ghosh, A., Smits, M., Sovago, M., Bredenbeck, J., Müller, M., & Bonn, M. (2008). Ultrafast vibrational dynamics of interfacial water. *Chemical Physics*, 350(1-3), 23–30. doi:10.1016/j.chemphys.2007.12.022
- Gianotti, E., Diaz, U., Veltz, A., & Corma, A. (2013). Designing bifunctional acid–base mesoporous hybrid catalysts for cascade reactions. *Catalysis Science & Technology*, 3(10), 2677–2688. doi:10.1039/c3cy00269a
- Gill, C., Price, B., & Jones, C. (2007). Sulfonic acid-functionalized silica-coated magnetic nanoparticle catalysts. *Journal of Catalysis*, 251(1), 145–152. doi:10.1016/j.jcat.2007.07.007
- Gobin, O. C., & Schüth, F. (2008). On the suitability of different representations of solid catalysts for combinatorial library design by genetic algorithms. *Journal of combinatorial chemistry*, 10(6), 835–46. doi:10.1021/cc800046u
- Guardia, P., Batlle-Brugal, B., & Roca, A. (2007). Surfactant effects in magnetite nanoparticles of controlled size. *Journal of Magnetism ...*, 316(2), 756–759. doi:10.1016/j.jmmm.2007.03.085
- Gubin, S. P., & Kataeva, N. a. (2006). Coordination chemistry of nanoparticles. *Russian Journal of Coordination Chemistry*, 32(12), 849–857. doi:10.1134/S1070328406120013

- Häfeli, U., Zborowski, M., Woo, K., Hong, J., & Ahn, J.-P. (2005). Synthesis and surface modification of hydrophobic magnetite to processible magnetite@silica-propylamine. *Journal of Magnetism and Magnetic Materials*, 293(1), 177–181. Retrieved from <http://www.sciencedirect.com/science/article/pii/S0304885305001538>
- Hara, M., Yoshida, T., Takagaki, A., Takata, T., Kondo, J. N., Hayashi, S., & Domen, K. (2004). A carbon material as a strong protonic acid. *Angewandte Chemie (International ed. in English)*, 43(22), 2955–8. doi:10.1002/anie.200453947
- Harris, V. G., Geiler, A., Chen, Y., Dae, S., Wu, M., Yang, A., ... Vittoria, C. (2009). Recent advances in processing and applications of microwave ferrites. *Journal of Magnetism and Magnetic Materials*, 321, 2035–2047. doi:10.1016/j.jmmm.2009.01.004
- Herbert, R., Wang, D., Schomäcker, R., Schlögl, R., & Hess, C. (2009). Stabilization of mesoporous silica SBA-15 by surface functionalization. *Chemphyschem : a European journal of chemical physics and physical chemistry*, 10(13), 2230–3. doi:10.1002/cphc.200900311
- Hill, H. D., Millstone, J. E., Banholzer, M. J., & Mirkin, C. A. (2009). The Role Radius of Curvature Plays in Thiolated Oligonucleotide Loading on. *ACS Nano*, 3(2), 418–424.
- Hofer, R. (2009). *Sustainable Solutions for Modern Economies* (p. 497). Royal Society of Chemistry. Retrieved from <http://books.google.com/books?id=5AG42e0qkHMC&pgis=1>
- Huang, P. M., & Wang, M. K. (1997). Formation chemistry and selected surface properties of iron oxides. *Advances in GeoEcology*, 30, 241–270.
- Ino, P., Nanodelcev, M., & Drmota, A. (2008). A MECHANISM FOR THE ADSORPTION OF CARBOXYLIC ACIDS ONTO THE SURFACE OF MAGNETIC NANOPARTICLES. *Materials and Technology*, 42(2), 79–83.
- Jérôme, F., Pouilloux, Y., & Barrault, J. (2008). Rational design of solid catalysts for the selective use of glycerol as a natural organic building block. *ChemSusChem*, 1(7), 586–613. doi:10.1002/cssc.200800069
- Jiang, W., Lai, K.-L., Hu, H., Zeng, X.-B., Lan, F., Liu, K.-X., ... Gu, Z.-W. (2011). The effect of [Fe³⁺]/[Fe²⁺] molar ratio and iron salts concentration on the properties of superparamagnetic iron oxide nanoparticles in the water/ethanol/toluene system. *Journal of Nanoparticle Research*, 13(10), 5135–5145. doi:10.1007/s11051-011-0495-8

- Kahani, S. A., & Jafari, M. (2009). A new method for preparation of magnetite from iron oxyhydroxide or iron oxide and ferrous salt in aqueous solution. *Journal of Magnetism and Magnetic Materials*, 321(13), 1951–1954. doi:10.1016/j.jmmm.2008.12.026
- Kalescky, R. J. B., Shinoda, W., Moore, P. B., & Nielsen, S. O. (2009). Area per ligand as a function of nanoparticle radius: a theoretical and computer simulation approach. *Langmuir : the ACS journal of surfaces and colloids*, 25(3), 1352–9. doi:10.1021/la8032918
- Kanth, J. M. P., Vemparala, S., & Anishetty, R. (2010). Long-distance correlations in molecular orientations of liquid water and shape-dependent hydrophobic force. *Physical review. E, Statistical, nonlinear, and soft matter physics*, 81(2 Pt 1), 021201. Retrieved from <http://www.ncbi.nlm.nih.gov/pubmed/20365555>
- Khanh, B. T. H. L., Hoang, V. V., & Zung, H. (2008). P HYSICAL J OURN A L D Structural properties of amorphous Fe₂O₃ nanoparticles. *The European Physical Journal*, 332(49), 325–332. doi:10.1140/epjd/e2008-00168-1
- Kikura, H., Matsushita, J., Matsuzaki, M., Kobayashi, Y., & Aritomi, M. (2004). Thermal behaviour and particle size evaluation of primary clusters in a water-based magnetic fluid. *Science and Technology of Advanced Materials*, 5(5-6), 703–707. doi:10.1016/j.stam.2004.04.001
- Kilpeläinen, I., Xie, H., King, A., Granstrom, M., Heikkinen, S., & Argyropoulos, D. S. (2007). Dissolution of wood in ionic liquids. *Journal of agricultural and food chemistry*, 55(22), 9142–8. doi:10.1021/jf071692e
- Kitano, M., Yamaguchi, D., Suganuma, S., Nakajima, K., Kato, H., Hayashi, S., & Hara, M. (2009). Adsorption-enhanced hydrolysis of beta-1,4-glucan on graphene-based amorphous carbon bearing SO₃H, COOH, and OH groups. *Langmuir : the ACS journal of surfaces and colloids*, 25(9), 5068–75. doi:10.1021/la8040506
- Klokkenburg, M., Hilhorst, J., & Ern , B. H. (2007). Surface analysis of magnetite nanoparticles in cyclohexane solutions of oleic acid and oleylamine. *Vibrational Spectroscopy*, 43(1), 243–248. doi:10.1016/j.vibspec.2006.09.008
- Kralj, S., Makovec, D.,  ampelj, S., & Drogenik, M. (2010). Producing ultra-thin silica coatings on iron-oxide nanoparticles to improve their surface reactivity. *Journal of Magnetism and Magnetic Materials*, 322(13), 1847–1853. doi:10.1016/j.jmmm.2009.12.038

- Kusaka, I., Wang, Z.-G., & Seinfeld, J. H. (1998). Binary nucleation of sulfuric acid-water: Monte Carlo simulation. *The Journal of Chemical Physics*, *108*(16), 6829. doi:10.1063/1.476097
- Lai, D., Deng, L., Guo, Q., & Fu, Y. (2011). Hydrolysis of biomass by magnetic solid acid. *Energy & Environmental Science*, *4*(9), 3552. doi:10.1039/c1ee01526e
- Lai, D., Deng, L., Li, J., Liao, B., Guo, Q., & Fu, Y. (2011). Hydrolysis of cellulose into glucose by magnetic solid acid. *ChemSusChem*, *4*(1), 55–8. doi:10.1002/cssc.201000300
- Lattuada, M., & Hatton, T. A. (2007). Functionalization of monodisperse magnetic nanoparticles. *Langmuir : the ACS journal of surfaces and colloids*, *23*(4), 2158–68. doi:10.1021/la062092x
- Laurent, S., Forge, D., Port, M., Roch, A., Robic, C., Vander Elst, L., & Muller, R. N. (2008). Magnetic iron oxide nanoparticles: synthesis, stabilization, vectorization, physicochemical characterizations, and biological applications. *Chemical reviews*, *108*(6), 2064–110. doi:10.1021/cr068445e
- Lee, J., Lee, Y., Youn, J. K., Na, H. Bin, Yu, T., Kim, H., ... Hyeon, T. (2008). Simple synthesis of functionalized superparamagnetic magnetite/silica core/shell nanoparticles and their application as magnetically separable high-performance biocatalysts. *Small (Weinheim an der Bergstrasse, Germany)*, *4*(1), 143–52. doi:10.1002/smll.200700456
- Li, C., Wang, Q., & Zhao, Z. K. (2008). Acid in ionic liquid: An efficient system for hydrolysis of lignocellulose. *Green Chemistry*, *10*(2), 177. doi:10.1039/b711512a
- Li, G., Fan, J., Jiang, R., & Gao, Y. (2004). Cross-linking the Linear Polymeric Chains in the ATRP Synthesis of Iron Oxide / Polystyrene Core / Shell Nanoparticles. *Chemistry of Materials*, *16*(10), 1835–1837.
- Lin, Y.-S., & Haynes, C. L. (2009). Synthesis and Characterization of Biocompatible and Size-Tunable Multifunctional Porous Silica Nanoparticles. *Chemistry of Materials*, *21*(17), 3979–3986. doi:10.1021/cm901259n
- Liu, J., Sun, Z., Deng, Y., Zou, Y., Li, C., Guo, X., ... Zhao, D. (2009). Highly Water-Dispersible Biocompatible Magnetite Particles with Low Cytotoxicity Stabilized by Citrate Groups. *Angewandte Chemie*, *121*(32), 5989–5993. doi:10.1002/ange.200901566

- Liu, X., Yu, M., Kim, H., Mameli, M., & Stellacci, F. (2012). Determination of monolayer-protected gold nanoparticle ligand-shell morphology using NMR. *Nature communications*, 3, 1182. doi:10.1038/ncomms2155
- Long, W., & Jones, C. W. (2011). Hybrid Sulfonic Acid Catalysts Based on Silica-Supported Poly(Styrene Sulfonic Acid) Brush Materials and Their Application in Ester Hydrolysis. *ACS Catalysis*, 1(7), 674–681. doi:10.1021/cs2001175
- Lu, A., Salabas, E. L., & Schüth, F. (2007). Magnetic Nanoparticles: Synthesis, Protection, Functionalization, and Application. *Angewandte Chemie (International ed. in English)*, 46, 1222–1244. doi:10.1002/anie.200602866
- Luo, H., Ma, L., Zhang, Y., & Carr, P. W. (2008). Synthesis and characterization of silica-based hyper-crosslinked sulfonate-modified reversed stationary phases. *Journal of chromatography. A*, 1182(1), 41–55. doi:10.1016/j.chroma.2007.11.104
- Machunsky, S., Grimm, P., Schmid, H.-J., & Peuker, U. a. (2009). Liquid–liquid phase transfer of magnetite nanoparticles. *Colloids and Surfaces A: Physicochemical and Engineering Aspects*, 348(1-3), 186–190. doi:10.1016/j.colsurfa.2009.07.014
- Mahadeva, S. K., & Kim, J. (2009). Electromechanical Behavior of Room Temperature Ionic Liquid Dispersed Cellulose. *The Journal of Physical Chemistry C*, 113(28), 12523–12529. doi:10.1021/jp9024238
- Massart, R. (1981). Preparation of Aqueous Magnetic Liquids in Alkaline and Acidic Media. *IEEE Transactions on Magnetics*, 17(2), 1247–1248.
- Mbaraka, I., & Shanks, B. (2006). Acid strength variation due to spatial location of organosulfonic acid groups on mesoporous silica. *Journal of Catalysis*, 244(1), 78–85. doi:10.1016/j.jcat.2006.09.001
- Mohapatra, S., Mallick, S. K., Maiti, T. K., Ghosh, S. K., & Pramanik, P. (2007). Synthesis of highly stable folic acid conjugated magnetite nanoparticles for targeting cancer cells. *Nanotechnology*, 18(38), 385102. doi:10.1088/0957-4484/18/38/385102
- Mohapatra, Sasmita, & Pramanik, P. (2009). Synthesis and stability of functionalized iron oxide nanoparticles using organophosphorus coupling agents. *Colloids and Surfaces A: Physicochemical and Engineering Aspects*, 339(1-3), 35–42. doi:10.1016/j.colsurfa.2009.01.009

- Morel, A.-L., Nikitenko, S. I., Gionnet, K., Wattiaux, A., Lai-Kee-Him, J., Labrugere, C., ... Simonoff, M. (2008). Sonochemical approach to the synthesis of Fe(3)O(4)@SiO(2) core-shell nanoparticles with tunable properties. *ACS nano*, 2(5), 847–56. doi:10.1021/nn800091q
- Mosier, N. S., Ladisch, C. M., & Ladisch, M. R. (2002). Characterization of acid catalytic domains for cellulose hydrolysis and glucose degradation. *Biotechnology and bioengineering*, 79(6), 610–8. doi:10.1002/bit.10316
- Mundy, C. J., Kuo, I.-F. W., Tuckerman, M. E., Lee, H.-S., & Tobias, D. J. (2009). Hydroxide anion at the air–water interface. *Chemical Physics Letters*, 481(1-3), 2–8. doi:10.1016/j.cplett.2009.09.003
- Nagle, N., Ibsen, K., & Jennings, E. (1999). A process economic approach to develop a dilute-acid cellulose hydrolysis process to produce ethanol from biomass. *Applied biochemistry and biotechnology*, 77-79, 595–607. Retrieved from <http://www.ncbi.nlm.nih.gov/pubmed/15304681>
- Naik, S. N., Goud, V. V., Rout, P. K., & Dalai, A. K. (2010). Production of first and second generation biofuels: A comprehensive review. *Renewable and Sustainable Energy Reviews*, 14(2), 578–597. doi:10.1016/j.rser.2009.10.003
- Nakajima, K., Hara, M., & Hayashi, S. (2007). Environmentally Benign Production of Chemicals and Energy Using a Carbon-Based Strong Solid Acid. *Journal of the American Ceramic Society*, 071019062949001–??? doi:10.1111/j.1551-2916.2007.02082.x
- Nakajima, K., Okamura, M., Kondo, J. N., Tatsumi, T., Hayashi, S., Hara, M., & Domen, K. (2009). Amorphous Carbon Bearing Sulfonic Acid Groups in Mesoporous Silica as a Selective Catalyst. *Chemistry of Materials*, 21(1), 186–193. doi:10.1021/cm801441c
- Nakamoto, K. (1997). *Infrared and Raman Spectra of Inorganic and Coordination Compounds* (p. 232). New York: John Wiley & Sons.
- Neouze, M.-A., & Schubert, U. (2008). Surface Modification and Functionalization of Metal and Metal Oxide Nanoparticles by Organic Ligands. *Monatshefte für Chemie - Chemical Monthly*, 139(3), 183–195. doi:10.1007/s00706-007-0775-2
- Ngo, T. H., Tran, D. L., Do, H. M., Tran, V. H., Le, V. H., & Nguyen, X. P. (2010). Facile and solvent-free routes for the synthesis of size-controllable Fe₃O₄ nanoparticles. *Advances in*

Natural Sciences: Nanoscience and Nanotechnology, 1(3). doi:10.1088/2043-6254/1/3/035001

- Notestein, J. M., & Katz, A. (2006). Enhancing heterogeneous catalysis through cooperative hybrid organic-inorganic interfaces. *Chemistry (Weinheim an der Bergstrasse, Germany)*, 12(15), 3954–65. doi:10.1002/chem.200501152
- Okuhara, T. (2002). Water-tolerant solid acid catalysts. *Chemical reviews*, 102(10), 3641–65. Retrieved from <http://www.ncbi.nlm.nih.gov/pubmed/12371897>
- Onda, A., Ochi, T., & Yanagisawa, K. (2008). Selective hydrolysis of cellulose into glucose over solid acid catalysts. *Green Chemistry*, 10(10), 1033. doi:10.1039/b808471h
- Orozcoa, A., Ahmada, M., Rooney, D., & Walker, G. (2007). Dilute Acid Hydrolysis of Cellulose and Cellulosic Bio-Waste Using a Microwave Reactor System.pdf. *Process Safety and Environmental Protection*, 85(5), 446–449.
- Pang, J., Wang, A., Zheng, M., & Zhang, T. (2010). Hydrolysis of cellulose into glucose over carbons sulfonated at elevated temperatures. *Chemical communications (Cambridge, England)*, 46(37), 6935–7. doi:10.1039/c0cc02014a
- Park, J., An, K., Hwang, Y., Park, J.-G., Noh, H.-J., Kim, J.-Y., ... Hyeon, T. (2004). Ultra-large-scale syntheses of monodisperse nanocrystals. *Nature materials*, 3(12), 891–5. doi:10.1038/nmat1251
- Park, J., Lee, E., Hwang, N.-M., Kang, M., Kim, S. C., Hwang, Y., ... Hyeon, T. (2005). One-nanometer-scale size-controlled synthesis of monodisperse magnetic iron oxide nanoparticles. *Angewandte Chemie (International ed. in English)*, 44(19), 2873–7. doi:10.1002/anie.200461665
- Park, J. Y., Choi, E. S., Baek, M. J., & Lee, G. H. (2009). Colloidal stability of amino acid coated magnetite nanoparticles in physiological fluid. *Materials Letters*, 63(3-4), 379–381. doi:10.1016/j.matlet.2008.10.057
- Park, J.-N., Zhang, P., Hu, Y.-S., & McFarland, E. W. (2010). Synthesis and characterization of sintering-resistant silica-encapsulated Fe₃O₄ magnetic nanoparticles active for oxidation and chemical looping combustion. *Nanotechnology*, 21(22), 225708. doi:10.1088/0957-4484/21/22/225708

- Peña, L., Ikenberry, M., Ware, B., Hohn, K. L., Boyle, D., Sun, X. S., & Wang, D. (2011). Cellobiose hydrolysis using acid-functionalized nanoparticles. *Biotechnology and Bioprocess Engineering*, 16(6), 1214–1222. doi:10.1007/s12257-011-0166-8
- Perlack, R. D., & Stokes, B. J. (2011). *U.S. BILLION-TON UPDATE: Biomass Supply for a Bioenergy and Bioproduct Industry. Renewable Energy* (pp. 1–227). doi:10.2172/1023318
- Phan, N. T. S., & Jones, C. W. (2006). Highly accessible catalytic sites on recyclable organosilane-functionalized magnetic nanoparticles: An alternative to functionalized porous silica catalysts. *Journal of Molecular Catalysis A: Chemical*, 253(1-2), 123–131. doi:10.1016/j.molcata.2006.03.019
- Portet, D., Denizot, B., Rump, E., Lejeune, J.-J., & Jallet, P. (2001). Nonpolymeric Coatings of Iron Oxide Colloids for Biological Use as Magnetic Resonance Imaging Contrast Agents. *Journal of Colloid and Interface Science*, 238, 37–42.
- Qu, H., Ma, H., Riviere, A., Zhou, W., & O'Connor, C. J. (2012). One-pot synthesis in polyamines for preparation of water-soluble magnetite nanoparticles with amine surface reactivity. *Journal of Materials Chemistry*, 22(8), 3311. doi:10.1039/c2jm15932e
- Rajh, T., Chen, L. X., Lukas, K., Liu, T., Thurnauer, M. C., & Tiede, D. M. (2002). Surface Restructuring of Nanoparticles : An Efficient Route for Ligand - Metal Oxide Crosstalk. *Journal of Physical Chemistry B*, 106, 10543–10552.
- Rinaldi, R., & Schüth, F. (2009). Acid hydrolysis of cellulose as the entry point into biorefinery schemes. *ChemSusChem*, 2(12), 1096–107. doi:10.1002/cssc.200900188
- Rondinone, A. J., Samia, A. C. S., & Zhang, Z. J. (1999). Superparamagnetic Relaxation and Magnetic Anisotropy Energy Distribution in CoFe₂O₄ Spinel Ferrite Nanocrystallites. *Journal of Physical Chemistry B*, 103(1), 6876–6880.
- Roonasi, P., & Holmgren, A. (2009). A Fourier transform infrared (FTIR) and thermogravimetric analysis (TGA) study of oleate adsorbed on magnetite nano-particle surface. *Applied Surface Science*, 255(11), 5891–5895. doi:10.1016/j.apsusc.2009.01.031
- Rostrup-Nielsen, J. R. (2005). Chemistry. Making fuels from biomass. *Science (New York, N.Y.)*, 308(5727), 1421–2. doi:10.1126/science.1113354
- Sahoo, Y., Goodarzi, A., Swihart, M. T., Ohulchanskyy, T. Y., Kaur, N., Furlani, E. P., & Prasad, P. N. (2005). Aqueous ferrofluid of magnetite nanoparticles: Fluorescence labeling

- and magnetophoretic control. *The journal of physical chemistry. B*, 109(9), 3879–85.
doi:10.1021/jp045402y
- Sahoo, Y., Pizem, H., Fried, T., Golodnitsky, D., Burstein, L., Sukenik, C. N., & Markovich, G. (2001). Alkyl Phosphonate / Phosphate Coating on Magnetite Nanoparticles : A Comparison with Fatty Acids Alkyl Phosphonate / Phosphate Coating on Magnetite Nanoparticles : A Comparison with Fatty Acids. *Langmuir : the ACS journal of surfaces and colloids*, 17(25), 7907–7911. doi:10.1021/la010703
- Santoyo-Salazar, J., Castellanos-Roman, M. a., & Beatriz Gómez, L. (2007). Structural and magnetic domains characterization of magnetite nanoparticles. *Materials Science and Engineering: C*, 27(5-8), 1317–1320. doi:10.1016/j.msec.2006.07.027
- Santra, S., Tapeç, R., Theodoropoulou, N., Dobson, J., Hebard, A., & Tan, W. (2001). Synthesis and Characterization of Silica-Coated Iron Oxide Nanoparticles in Microemulsion: The Effect of Nonionic Surfactants. *Langmuir*, 17(10), 2900–2906. doi:10.1021/la0008636
- Schuster, M., Kreuer, K.-D., Andersen, H. T., & Maier, J. (2007). Sulfonated Poly(phenylene sulfone) Polymers as Hydrolytically and Thermo-oxidatively Stable Proton Conducting Ionomers. *Macromolecules*, 40(3), 598–607. doi:10.1021/ma062324z
- Sen, T., Magdassi, S., Nizri, G., & Bruce, I. (2006). Dispersion of magnetic nanoparticles in suspension. *Micro & Nano Letters*, 1(1), 39–42. doi:10.1049/mnl
- Shafi, K. V. P. M., Ulman, A., Yan, X., Yang, N., & Estourne, C. (2001). Sonochemical Synthesis of Functionalized Amorphous Iron Oxide Nanoparticles. *Langmuir : the ACS journal of surfaces and colloids*, 17(13), 5093–5097.
- Shen, L., Laibinis, P. E., & Hatton, T. A. (1999). Bilayer Surfactant Stabilized Magnetic Fluids: Synthesis and Interactions at Interfaces. *Langmuir*, 15(2), 447–453. doi:10.1021/la9807661
- Shen, X.-C., Fang, X.-Z., Zhou, Y.-H., & Liang, H. (2004). Synthesis and Characterization of 3-Aminopropyltriethoxysilane-Modified Superparamagnetic Magnetite Nanoparticles. *Chemistry Letters*, 33(11), 1468–1469. doi:10.1246/cl.2004.1468
- Shi, G., Xue, G., Li, C., & Jin, S. (1994). Layered poly(naphthalene) films prepared by electrochemical polymerization. *Polymer Bulletin*, 33(3), 325–329.
doi:10.1007/BF00314270
- Shu, Q., Nawaz, Z., Gao, J., Liao, Y., Zhang, Q., Wang, D., & Wang, J. (2010). Synthesis of biodiesel from a model waste oil feedstock using a carbon-based solid acid catalyst:

- reaction and separation. *Bioresource technology*, 101(14), 5374–84.
doi:10.1016/j.biortech.2010.02.050
- Siddiqui, S. W., Unwin, P. J., Xu, Z., & Kresta, S. M. (2009). The effect of stabilizer addition and sonication on nanoparticle agglomeration in a confined impinging jet reactor. *Colloids and Surfaces A: Physicochemical and Engineering Aspects*, 350(1-3), 38–50.
doi:10.1016/j.colsurfa.2009.08.031
- Stavrinides, A. J., Phipps, D. A., & Shamma, A. A.-. (n.d.). REVIEW ; CURRENT AND DEVELOPING LIGNO- CELLULOSIC PRETREATMENT METHODS FOR BIOETHANOL PRODUCTION, 233–242.
- Stephens, C. H., Whitmore, P. M., Morris, H. R., & Bier, M. E. (2008). Hydrolysis of the amorphous cellulose in cotton-based paper. *Biomacromolecules*, 9(4), 1093–9.
doi:10.1021/bm800049w
- Stoeva, S. I., Smetana, A. B., Sorensen, C. M., & Klabunde, K. J. (2007). Gram-scale synthesis of aqueous gold colloids stabilized by various ligands. *Journal of colloid and interface science*, 309(1), 94–98. doi:10.1016/j.jcis.2006.12.064
- Suganuma, S., Nakajima, K., Kitano, M., Yamaguchi, D., Kato, H., Hayashi, S., & Hara, M. (2010). Synthesis and acid catalysis of cellulose-derived carbon-based solid acid. *Solid State Sciences*, 12(6), 1029–1034. doi:10.1016/j.solidstatesciences.2010.02.038
- Summers, M., & Eastoe, J. (2003). Applications of polymerizable surfactants. *Advances in Colloid and Interface Science*, 100, 137–152. Retrieved from <http://www.sciencedirect.com/science/article/pii/S0001868602000581>
- Sun, S., & Zeng, H. (2002). Size-Controlled Synthesis of Magnetite Nanoparticles. *Journal of the American Chemical Society*, 124(28), 8204–8205. doi:10.1021/ja026501x
- Sun, X., Yoo, S., Xantheas, S. S., & Dang, L. X. (2009). The reorientation mechanism of hydroxide ions in water: A molecular dynamics study. *Chemical Physics Letters*, 481(1), 9–16. Retrieved from <http://www.sciencedirect.com/science/article/pii/S0009261409010963>
- Sun, Ye, & Cheng, J. (2002). Hydrolysis of lignocellulosic materials for ethanol production: a review. *Bioresource Technology*, 83(1), 1–11. doi:10.1016/S0960-8524(01)00212-7
- Sun, Yong, Zhuang, J., Lin, L., & Ouyang, P. (2009). Clean conversion of cellulose into fermentable glucose. *Biotechnology advances*, 27(5), 625–32.
doi:10.1016/j.biotechadv.2009.04.023

- Sun, Yongkang, Duan, L., Guo, Z., DuanMu, Y., Ma, M., Xu, L., ... Gu, N. (2005). An improved way to prepare superparamagnetic magnetite-silica core-shell nanoparticles for possible biological application. *Journal of Magnetism and Magnetic Materials*, 285(1), 65–70. Retrieved from <http://www.sciencedirect.com/science/article/pii/S030488530400767X>
- Sun, Z., Su, F., Forsling, W., & Samskog, P. (1998). Surface Characteristics of Magnetite in Aqueous Suspension. *Journal of colloid and interface science*, 197(1), 151–9. Retrieved from <http://www.ncbi.nlm.nih.gov/pubmed/19304376>
- Taffa, D., Kathiresan, M., & Walder, L. (2009). Tuning the hydrophilic, hydrophobic, and ion exchange properties of mesoporous TiO₂. *Langmuir : the ACS journal of surfaces and colloids*, 25(9), 5371–9. doi:10.1021/la8038126
- Theppaleak, T., Tumcharern, G., Wichai, U., & Rutnakornpituk, M. (2009). Synthesis of water dispersible magnetite nanoparticles in the presence of hydrophilic polymers. *Polymer Bulletin*, 63(1), 79–90. doi:10.1007/s00289-009-0075-6
- Thøgersen, J., Jensen, S. K., Petersen, C., & Keiding, S. R. (2008). Reorientation of hydroxide ions in water. *Chemical Physics Letters*, 466(1-3), 1–5. doi:10.1016/j.cplett.2008.10.023
- Thomas, J. M. (1997). The Ineluctable Need for in Situ Methods of Characterising Solid Catalysts as a Prerequisite to Engineering Active Sites. *Chemistry - A European Journal*, 3(10), 1557–1562. doi:10.1002/chem.19970031004
- Van de Vyver, S., Peng, L., Geboers, J., Schepers, H., de Clippel, F., Gommès, C. J., ... Sels, B. F. (2010). Sulfonated silica/carbon nanocomposites as novel catalysts for hydrolysis of cellulose to glucose. *Green Chemistry*, 12(9), 1560. doi:10.1039/c0gc00235f
- Van de Vyver, S., Geboers, J., Jacobs, P. a., & Sels, B. F. (2011). Recent Advances in the Catalytic Conversion of Cellulose. *ChemCatChem*, 3(1), 82–94. doi:10.1002/cctc.201000302
- Vayssieres, L. (2005). On the thermodynamic stability of metal oxide nanoparticles in aqueous solutions. *International journal of nanotechnology*, 2(4), 411–439. Retrieved from <http://inderscience.metapress.com/index/2m6vn2cjxu2ehapa.pdf>
- Vekasa, L., Bica, D., & Avdeev, M. (2007). Magnetic nanoparticles and concentrated magnetic nanofluids- Synthesis, properties and some applications.pdf. *China Particuology*, 5(1-2), 43–49.

- Vereda, F., Vicente, J. De, & Hidalgo-Alvarez, R. (2007). Influence of a magnetic field on the formation of magnetite particles via two precipitation methods. *Langmuir : the ACS journal of surfaces and colloids*, 23(7), 3581–9. doi:10.1021/la0633583
- Vinod, T. P., Chang, J. H., Kim, J., & Rhee, S. W. (2008). Self-Assembly and Photopolymerization of Diacetylene Molecules on Surface of Magnetite Nanoparticles, 29(4), 799–804.
- Wang, D., Nap, R. J., Lagzi, I., Kowalczyk, B., Han, S., Grzybowski, B. a, & Szleifer, I. (2011). How and why nanoparticle's curvature regulates the apparent pKa of the coating ligands. *Journal of the American Chemical Society*, 133(7), 2192–7. doi:10.1021/ja108154a
- Wang, F., Izvekov, S., & Voth, G. a. (2008). Unusual “amphiphilic” association of hydrated protons in strong acid solution. *Journal of the American Chemical Society*, 130(10), 3120–6. doi:10.1021/ja078106i
- Wang, L., Bao, J., Wang, L., Zhang, F., & Li, Y. (2006). One-pot synthesis and bioapplication of amine-functionalized magnetite nanoparticles and hollow nanospheres. *Chemistry (Weinheim an der Bergstrasse, Germany)*, 12(24), 6341–7. doi:10.1002/chem.200501334
- Wang, X., & Lieberman, M. (2003). Zirconium - Phosphonate Monolayers with Embedded Disulfide Bonds. *Langmuir : the ACS journal of surfaces and colloids*, 19(11), 7346–7353.
- Wang, Y., Teng, X., Wang, J., & Yang, H. (2003). Solvent-free atom transfer radical polymerization in the synthesis of Fe₂O₃@ polystyrene core-shell nanoparticles. *Nano letters*, 3(6), 2–6. Retrieved from <http://pubs.acs.org/doi/abs/10.1021/nl034211o>
- Wei, X., Zhang, D., & Liu, C. (2008). A DFT study on the hydrolysis stabilities of silica molecular chains and rings based on the two-membered rings. *Journal of Molecular Structure: THEOCHEM*, 859(1), 1–6. Retrieved from <http://www.sciencedirect.com/science/article/pii/S0166128008001115>
- WPettersson, P. O., Torget, R. W., Eklund, R., Xiang, Q., Lee, Y. Y., & Zacchi, G. (2003). Simplistic modeling approach to heterogeneous dilute-acid hydrolysis of cellulose microcrystallites. *Applied biochemistry and biotechnology*, 105 -108(1), 451–6. Retrieved from <http://www.ncbi.nlm.nih.gov/pubmed/12721467>
- Xiang, Q., Kim, J. S., & Lee, Y. (2003). A comprehensive Kinetic Model for Dilute-Acid Hydrolysis of Cellulose. *Applied biochemistry and biotechnology*, 105(1), 337–352.

- Yamaguchi, D., Kitano, M., Suganuma, S., Nakajima, K., Kato, H., & Hara, M. (2009). Hydrolysis of Cellulose by a Solid Acid Catalyst under Optimal Reaction Conditions. *The Journal of Physical Chemistry C*, 113(8), 3181–3188. doi:10.1021/jp808676d
- Yang, K., Peng, H., Wen, Y., & Li, N. (2010). Re-examination of characteristic FTIR spectrum of secondary layer in bilayer oleic acid-coated Fe₃O₄ nanoparticles. *Applied Surface Science*, 256(10), 3093–3097. doi:10.1016/j.apsusc.2009.11.079
- Yee, C., Kataby, G., Ulman, A., Prozorov, T., White, H., King, A., ... Gedanken, A. (1999). Self-Assembled Monolayers of Alkanesulfonic and -phosphonic Acids on Amorphous Iron Oxide Nanoparticles. *Langmuir : the ACS journal of surfaces and colloids*, 15(8), 7111–7115.
- Yoo, M. K., Kim, I. Y., Kim, E. M., Jeong, H., Lee, C., Jeong, Y. Y., ... Cho, C. S. (2007). Superparamagnetic Iron Oxide Nanoparticles Coated with Galactose-Carrying Polymer for Hepatocyte Targeting. *Journal of Biomedicine and Biotechnology*, 2007, 1–9. doi:10.1155/2007/94740
- Yoshioka, Y., Nakahara, H., & Fukuda, K. (1985). Photopolymerizations in Langmuir-Blodgett films of monoacids containing phenyl and diacetylene groups simultaneously. *Thin Solid Films*, 133(1), 11–19. Retrieved from <http://www.sciencedirect.com/science/article/pii/0040609085904201>
- Yu, S., & Chow, G. M. (2004). Carboxyl group (?CO₂H) functionalized ferrimagnetic iron oxide nanoparticles for potential bio-applications. *Journal of Materials Chemistry*, 14(18), 2781. doi:10.1039/b404964k
- Zhang, C., Wängler, B., Morgenstern, B., Zentgraf, H., Eisenhut, M., Untenecker, H., ... Kiessling, F. (2007). Silica- and alkoxy silane-coated ultrasmall superparamagnetic iron oxide particles: a promising tool to label cells for magnetic resonance imaging. *Langmuir : the ACS journal of surfaces and colloids*, 23(3), 1427–34. doi:10.1021/la061879k
- Zhang, F., Jin, J., Zhong, X., Li, S., Niu, J., Li, R., & Ma, J. (2011). Pd immobilized on amine-functionalized magnetite nanoparticles: a novel and highly active catalyst for hydrogenation and Heck reactions. *Green Chemistry*, 13(5), 1238. doi:10.1039/c0gc00854k
- Zhang, L., He, R., & Gu, H.-C. (2006). Oleic acid coating on the monodisperse magnetite nanoparticles. *Applied Surface Science*, 253(5), 2611–2617. doi:10.1016/j.apsusc.2006.05.023

- Zhang, W. (2003). Nanoscale iron particles for environmental remediation : An overview. *Journal of Nanoparticle Research*, 5, 323–332.
- Zhang, Y.-H. P., Ding, S.-Y., Mielenz, J. R., Cui, J.-B., Elander, R. T., Laser, M., ... Lynd, L. R. (2007). Fractionating recalcitrant lignocellulose at modest reaction conditions. *Biotechnology and bioengineering*, 97(2), 214–23. doi:10.1002/bit.21386
- Zhang, Z., & Zhao, Z. K. (2009). Solid acid and microwave-assisted hydrolysis of cellulose in ionic liquid. *Carbohydrate Research*. Retrieved from <http://www.sciencedirect.com/science/article/pii/S0008621509003450>
- Zheng, R., Gu, H., Xu, B., Fung, K., & Zhang, X. (2005). Self-assembly and self-orientation of truncated nano-octahedra of magnetite. Retrieved from <http://arxiv.org/abs/cond-mat/0512433>

